

Structure-property relationships in a porous
ceramic solid where porosity is variable by
composition and sintering

Anthony Flynn

May 2009

*

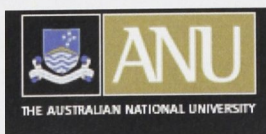
A thesis submitted for the degree

of

Doctor of Philosophy

of

The Australian National University



Structure-property relationships in a porous
ceramic solid where porosity is variable by
composition and sintering

Anthony Flynn



A thesis submitted for the degree

Doctor of Philosophy

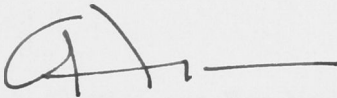
The Australian National University



Certificate

Declaration

I certify that this thesis does not incorporate, without acknowledgement, any material previously submitted for a degree or diploma in any university and that, to the best of my knowledge, it does not contain any material previously published or written by another person except where due reference is made in the text. The work in this thesis is originally my own, except for the contributions made by others as described in the Acknowledgements.

A handwritten signature in black ink, consisting of a stylized initial 'A' followed by a horizontal line.

Dated the twenty-second day of May 2009

I gratefully acknowledge the love, generosity and patience of my wife, Jude, and our children, Pip, Hughie and Anna, whose support and sometimes baffled forbearance over the years of this strange and often inexplicable process made it not only possible, but especially worthwhile.

And to Dr Zbigniew H. Stachurski, though no doubt aware of the special pitfalls of an older student whose background was the art world rather than engineering, who nevertheless agreed to be my Supervisor, continuing the role he began in 1996, I am profoundly grateful for his friendship and participation.

This thesis purports to be the work of one individual, but it summarises the result of the input of many people and their facilities, in fact too many to detail, both within this University and elsewhere, their advice and assistance often sought and always freely given, all were participants and all are inseparable from its outcomes.

Rob Gresham and Ben Nash, colleagues in the Department of Engineering, are admirable for their wonderful and lateral capacity to solve problems and devise odd pieces of equipment whenever the need arose.

I remain indebted to Dr Frank Brink and Dr Roger Heady, both of the Electron Microscopy Unit, RSBS, ANU, who have for eight years been constantly available in their assistance with my imaging and analysis of the structures that are the subject of this work.

Abstract

This research sees the invention, further development and characterisation of a strong, porous, sintered-ceramic solid in which porosity is both articulated and variable by composition and sintering. This is achieved by the addition of ceramic powders to cenospheres, a system of hollow alumino-silicate single spheres and elliptical aggregations of smaller spheres. When intimately mixed with water a joining neck structure is formed at multiple cenosphere contact points, thereby creating a void fraction that is articulated or continuously connected one to another in three dimensions. The void fraction remains intact and patent when sintered across the range 1100°C to 1500°C. The final sintered form of the material is that of a solid in the form of an alumino-silicate scaffold, the geometry of which is defined by its sintered, solid fraction and a coexistent articulated-void fraction. The primary sintered-cenosphere structure's void fraction is infiltrated under vacuum with polymeric and additional compounds including polymers and minerals. Samples are examined using scanning electron microscopy and X-ray tomography of the sintered solid and its articulated void fraction. Sintered infiltrated samples are prepared and measured in the determination of signal-attenuation properties at the Tsukuba Photon Factory Beamline Facility, Tsukuba, Japan.

Table of Contents

Chapter 1	Introduction	1
1.01	Aim of the study	1
1.02	Scope of the study	1
Chapter 2	Literature review	8
2.1	Preamble	8
2.2	Cenospheres	9
2.3	Sintering	21
2.4	Granular systems	22
Chapter 3	Theoretical model	28
3.1	Microstructure	28
3.2	Determination of porosity	31
3.3	Permeability	33
3.4	Elastic modulus	34
3.5	Strength and fracture of porous ceramic sintered from spherical particles	36
3.6	Strength as a function of porosity	37
Chapter 4	Experimental methods and techniques	38
4.01	Factors considered in the choice of raw materials	38
4.02	Sintering of samples	39
4.03	Purchase of materials	40
4.04	Description of materials used in precursor experiments	41
4.05	Precursor experiments in evaluation of materials	41

Table of contents

4.06	Materials used in the formation of the primary structure	42
4.06.1	Cenospheres	42
4.06.2	Cenospheres, available grades	44
4.06.3	Description of cenosphere materials	44
4.06.4	Materials used in the formation of secondary structures	45
4.07	Choice of maximum sintering temperature range, °C	45
4.08	Constituent materials ratios by Group	46
4.08.1	Group A	46
4.08.2	Group B	47
4.08.3	Group C	50
4.08.4	Group D	51
4.09	Determination of sample form	52
4.09.1	Choice of the dimensions of the cylindrical form	52
4.09.2	Choice of material for cylindrical container form	52
4.09.3	Fabrication of cylindrical paper container form	54
4.10	Identification of samples	54
4.11	Mixing of dry materials for sintering	55
4.11.1	Compaction of samples in paper cylindrical former	55
4.11.2	Identification of samples after removal from the firing chamber	55
4.12	Choice of maximum sintering temperatures	56
4.13	Design of firing cycle	56
4.14	Sintering of samples	57
4.15	Recording of data	59
4.16	Measurement of permeability rates post firing	59
4.17	Measurement of sample compressive strength	60

Table of contents

4.18	Imaging and analysis of samples using SEM	61
4.18.1	Preparation of sample thin sections for SEM	61
4.18.2	SEM imaging of sample thin sections and fracture faces	62
4.19	Preparation of core samples for tomographic imaging	63
4.20	Vacuum infiltration of samples by polymerics	63
4.20.1	Vacuum infiltration	63
4.20.2	Summary of mixing sequence and infiltration under vacuum of polymerics	66
4.20.3	Summary of mixing sequence and infiltration of polymer/minerals and other compounds under vacuum	68
4.20.4	Choice of polymer for infiltration	69
4.20.5	Curing of samples infiltrated with a polymer	70
4.20.6	Preparation of cured, infiltrated samples for compression testing	71
4.20.7	Measurement of cured, infiltrated sample compressive strength	71
4.20.8	Preparation of samples for X-ray analysis	71
4.20.9	X-ray analysis of samples	72
4.20.10	Measurement of attenuation of signal	72
4.20.11	Tomographic imaging of sintered sample	72
Chapter 5	Results	73
5.1	Estimation of errors	73
5.1.1	Measurement of dimensions	74
5.1.2	Measurement of weight	74
5.1.3	Measurement of mechanical properties	74
5.1.4	Measurement of particle size	74
5.1.5	Sintering temperature	75
5.1.6	Calculation of density	75

Table of contents

5.2	Results	75
5.2.1	Density	75
5.2.2	Permeability	78
5.2.3	Strength	79
5.2.4	Modulus	82
5.2.5	Mechanical behaviour under compression	83
5.2.6	Signal attenuation	86
5.3	Sample morphology	87
Chapter 6	Discussion	94
6.1	Structure formation	94
6.2	Sample density	102
6.3	Permeability	106
6.4	Compression testing of uninfiltreated samples	107
6.5	Infiltration of the sintered structure with a polymer	113
6.5.1	Infiltration of Group A samples with polymer/mineral composites	115
Chapter 7	Conclusions	118
	References	120
	Bibliography	122
	Appendix	124

List of Figures

2.1	Dependence of cenosphere formation on iron oxide in ash	13
2.2	Plot of inverse of radius change of radius against radius	14
2.3	Pressure inside ash cenospheres	15
2.4	Network of normal contact branches in sample	23
2.5	Restoration of normal forces in sample	24
2.6	3-D and 2-D cross sections of random packing and concentration suspension with solid fraction	25
2.7	Particles in random packing and in suspension	26
2.8	Solid area fractions	26
3.1	Geometrical and morphological model of the sintered cenosphere structure	28
3.2	Photographic image of an expanded aluminium foam structure	29
4.1	Electronmicrograph of SL500 grade cenosphere particles	42
4.2	Electron micrograph of polished 30 μ m thin section of SL500 cenospheres,	43
4.3	Electronmicrograph of silica fume particles	48
4.4	Electronmicrograph of 30 μ m polished thin section of silica fume	49
4.5	Unsintered, dried samples showing numbering sequence	54
4.6	Group A, pre-firing in ANSTO Laser dilatometer furnace, 1300°C, showing silicon carbide shelving and high alumina sheeting	58
4.7	Desiccator chamber containing sample for de-airing, with vacuum pump attached	65
4.8	Sintered sample in container prior to vacuum infiltration	65
4.9	Cylinders of hardened polymer/mineral composite, each containing an infiltrated sintered sample	69
4.10	Small furnace used to cure infiltrated samples, Materials Laboratory, Department of Engineering, ANU	70
4.11	Autoclave used to cure infiltrated samples, Materials Laboratory, Department of Engineering, ANU	71
5.1	Group A, variation to average sample density	75
5.2	Group B, variation to average sample density	76
5.3	Group C, variation to average sample density	76
5.4	Groups A, C5, variation to average sample density	77
5.5	Group A, variation to average sample density before and after infiltration	77

List of figures

5.6	Group A, B, C variation to average sample permeability	78
5.7	Group A, variation to average density compared with average permeability	78
5.8	Group A, variation to average stress	79
5.9	Group A, variation to average stress compared with average permeability	79
5.10	Group B, variation to average stress	80
5.11	Group C, variation to average stress	80
5.12	Group A, C5, variation to average stress	81
5.13	Group A, variation to load at maximum load, uninfiltated and infiltated	81
5.14	Group A, C5, uninfiltated, Group A infiltated, variation to average modulus of elasticity	82
5.15	Group A, variation to average modulus of elasticity compared with average permeability	82
5.16	Sample 511, 1100°C, load at maximum load	83
5.17	Sample 765, 1200°C, load at maximum load	84
5.18	Sample 774, 1300°C, load at maximum load	84
5.19	Sample 785, 1400°C, load at maximum load	85
5.20	Sample 1285, 1500°C, load at maximum load	85
5.21	Results of Tsukuba beamline testing, sample #1768	86
5.22	Results of Tsukuba beamline testing, sample #1803	86
5.23	Electron micrograph of unsintered SL500 cenosphere particles	88
5.24	Group A, enlarged photographic image of a Group A sample	89
5.25	Group A, unsintered, cenospheres + kaolin + Frit, before sintering, electron micrograph of a polished thin section	89
5.26	Group A, sintered to 1100°C, electron micrograph of polished thin section	90
5.27	Group A, sintered to 1200°C, electron micrograph of polished thin section	90
5.28	Group A, sintered to 1300°C, electron micrograph of polished thin section	90
5.29	Group A, sintered to 1400°C, electron micrograph of polished thin section	91
5.30	Group A, sintered to 1500°C, electron micrograph of polished thin section	91
5.31	Group A, 1100C, electron micrograph of a polished thin section	91
5.32	Group A, 1100C, electron micrograph showing two cenosphere particles	92
5.33	X-ray tomography image of Group A material sintered to 1100°C	92
5.34	X-ray tomographic image of Group A material sintered to 1100°C, selection from data set	93

List of figures

5.35	Image of a single 100 μ m slice taken from a tomographic X-ray MPEG movie of a 5mm core cut from a Group A sample after sintering to 1100°C	93
6.1	Electron micrograph of a polished thin section of cenosphere-kaolin compound	94
6.2	Electron micrograph of aggregated kaolin particles	95
6.3	Electron micrograph of a Group A, 5mm core sample	97
6.41	3-D tomographic images of the same Group A sintered structure, 1100°C.	98
6.42	3-D tomographic images of the same Group A sintered structure, 1100°C.	98
6.43	3-D tomographic images of the same Group A sintered structure, 1100°C.	98
6.44	3-D tomographic images of the same Group A sintered structure, 1100°C.	98
6.5	Distribution of particles and voids at 25 frame intervals	101
6.61	Electron micrographs of a sintered stoneware clay body, sintered at four temperatures in the range 960°C, polished 30 μ m thin sections	104
6.62	Electron micrographs of a sintered stoneware clay body, sintered at four temperatures in the range 1050°C, polished 30 μ m thin sections	104
6.63	Electron micrographs of a sintered stoneware clay body, sintered at four temperatures in the range 1215°C, polished 30 μ m thin sections	104
6.64	Electron micrographs of a sintered stoneware clay body, sintered at four temperatures in the range 1294°C, polished 30 μ m thin sections	104
6.7	Failure modes of porous brittle cylinders under axial compression, Sammis and Ashby (1985)	108
6.8	Comparison of fracture-face images and differences in Instron recordings of failure in compression of two ceramic samples	110
6.9	Electron micrograph, void fraction and neck structure, Group A, 1500°C, showing crystal growth in association with neck materials in fused particles	112
6.10	Void fraction and neck structure, Group A, fracture face, 1400°C, showing intact internal skeletal structures in fused particles	113
6.11	Group A sample, 1100°C, showing transverse and longitudinal access points prior to vacuum infiltration	115
6.12	Group A sample, 1100°C, showing hardened surface after vacuum infiltration with Derakane 411-3350 Epoxy Vinyl Ester Resin and yellow lead	116
6.13	Group A sample, 1100°C, showing hardened surface after vacuum infiltration with Derakane 411-3350 Epoxy Vinyl Ester Resin and yellow lead, 1:2.5	116

List of Tables

1.0	Summary of materials groups and the temperatures	1
2.1	Densities and thickness of ash cenospheres	12
2.2	Gas composition and pressure in ash cenospheres	12
4.1	Cenospheres, marketed as econospheres, available grades, size ranges and diameter means	44
4.2	E-Spheres, SL500 grade, supplier's technical specifications and physical properties	44
4.3	The range of sintering temperatures, °C, to which each of the specified materials Groups was fired.	45
4.4	Identification of materials groups by sintering temperature, °C, and by constituent materials	46
4.5	Group A, weight of constituent materials	46
4.6	Group B, weight of constituent materials	47
4.7	Group C, weight of constituent materials	50
4.8	Group D, weight of constituent materials	51
4.9	Materials used in the compounding of materials for vacuum infiltration	64
4.10	Properties of Derakane 411-3350 Epoxy Vinyl Ester Resin [®]	69
6.1	Comparison of specific compressive strength of materials	117

Chapter 1

Introduction

Aim of the study

The ultimate aim of the study was to develop a structure that used only widely available, conventional ceramic materials in its formation and that could be combined and sintered using existing technology.

The sintered ceramic structure should display the following properties:

- (a) It should include a void fraction that is articulated in three dimensions
- (b) the topology of the structure should remain unchanged up to the melting points of individual and compounded ceramic components
- (c) the structure's void fraction should be able to be infiltrated by materials of specific properties

1.02 Scope of the study

- (a) The development of the sintered ceramic structure of compositions shown in Table 1.0
- (b) Morphological studies that include optical microscopy, SEM and X-ray tomography
- (c) Characterisation of the sintered structure's physical and mechanical properties.

Table 1.0: Summary of materials groups and the temperatures, °C, to which each was sintered

Materials Group and Additions		Sintering temperature, C				
Group	Additions	1100	1200	1300	1400	1500
A	*Base	•	•	•	•	•
B	*Base + silica fume +tin oxide	•	•	•	•	•
C	*Base + silica fume + tin oxide + cobalt carbonate	•	•	•	•	•

*Where the Base includes the same ratios of cenospheres, kaolin, frit, and water.

This thesis presents data, images-in-support and conclusions based upon research that saw the development of a ceramic structure which, by the nature of its constituent materials when sintered between 1100-1500°C, forms two coexisting scaffold structures,

- (a) the primary structure, an alumino-silicate scaffold that itself creates and exists simultaneously with the second structure,
- (b) a void-fraction articulated in three dimensions.

The primary raw materials used in the sintered structure are cenospheres, a hollow, spherical and elliptical alumino-silicate fraction of fly ash.

Sintered structures that are the subject of this thesis are in current experimental evaluation as high-temperature insulation in solar-generation applications where temperatures $>1500^{\circ}\text{C}$ are encountered and where simultaneous protection of static metal componentry and removal by absorption and diffusion of sustained high levels of absorbed energy are required. These insulation units have now been in use for two years.

This porous solid also presents properties and applications appropriate to the aerospace industry, offering potential for absorption of blast and impact energy and particularly in the creation of a series of structures, which when infiltrated with a polymer-particulate composite produces wavelength-specific signal attenuation.

The properties of the sintered structure are summarised as indicating potential in the following applications:

- Signal attenuation
- Absorption and diffusion-dispersal of heat
- Static high-temperature insulation
- Acoustic insulation

While cenospheres are in widespread use within the building and construction industries as additives to plaster sheeting, and as an important component of concrete used in general construction, there are no reports or papers to indicate concurrent research and development by others in the sintering of cenospheres in the production of a strong, sintered, porous-ceramic structure in which its void fraction is continuously articulated in three dimensions.

This work documents the development of a strong ceramic in which porosity is not eliminated, one in which it is predictably variable by composition and sintering, using combinations of materials that are cheap, readily available and in widespread use by industry. It sees the use of these materials in novel combinations and ratios, with sintering to five maximum temperatures between 1100°C-1500°C.

“Ceramic” is defined by Kingery, Bowen and Uhlmann [1] as, “...*the art and science of making and using solid articles which have as their essential component, and are composed in large part of, inorganic non-metal materials. This definition includes not only materials such as pottery, porcelain, refractories, structural clay products, abrasives, porcelain enamels, cements and glass, but also non-metal magnetic materials, ferroelectrics, manufactured single crystals, glass ceramics and a variety*

of other products which were not in existence until a few years ago and many which do not exist today.”

Barsoum [2] defines ceramics as, “...*solid compounds that are formed by the application of heat, and sometimes heat and pressure, comprising at least two elements provided one of them is a non-metal or a non-metal elemental solid. The other element(s) may be metal(s) or another non-metallic elemental solid(s)...In other words, what is neither a metal, a semi conductor or a polymer is a ceramic.*”

The Shorter Oxford Dictionary [3] sees “ceramics” in a form more accessible to the lay reader as being “...*of or pertaining to pottery, esp. as an art.*”

As applied to a ceramic material, the word “strong” can only be understood in terms of its measured strength, that is, the stress required to separate it into two parts, where it is a given that a defect or flaw in the form of voids is deleterious to that material’s strength. This understanding is predicated upon another given, that it is the intention of the fabricator to devise a ceramic structure that achieves a density and strength that is as close as achievable to theoretical possibility, with minimal or zero residual voids within its structure. But here it is the intention of this study to achieve high levels of strength in a sintered ceramic structure while simultaneously preserving its pore fraction across a wide firing-temperature range, a proposition diametrically opposed to the traditional theory and processes explicit in the sintering of ceramic materials.

“Porosity” is a concept that includes void structures and dimensions that range from vacancies between atoms, to the void microstructures of grain boundaries, to those

void macrostructures that are residual to the completion of a particular sintering cycle. While the literature explains the theory underlying the reduction or elimination of voids from a ceramic as it might be applied to conventional sintered ceramics, in this study this can only be applicable to that fraction of the total structure that is necessary for the fusion of the primary macro-particle ceramic material in the formation of a solid. In this work the general concept of “porosity” is effectively divided into two mutually exclusive categories:

- (a) the first, in which there is one class of voids that is the result of the choice of a specific material in the formation of a primary structure and in which, by the geometry of its constituent particles, sees the creation of a complex macro-void fraction that is articulated in three dimensions within that primary structure.
- (b) the second, in which a secondary micro-void structure is formed within the primary ceramic structure. It is the consequence of the combination of ceramic materials that are finer than the primary material, and the particles of which are irregular in their geometry, dissimilar in size and distribution and many orders of magnitude smaller than the equivalent spherical diameters of individual primary-material particles. This class of voids is only found in the neck structure that fuses the macro particles into a porous solid.

This second category of voids, (b) above, is contained within the much larger primary ceramic fraction and has been designed to behave conventionally on sintering. It will parallel conventional sintered-ceramic behaviour; its constituent

materials will progressively form micro-eutectics that in their formation will themselves facilitate the removal of micro voids and the achievement of a strong non-porous ceramic fraction. It is the sole function of this secondary ceramic fraction to bond together the larger particles of the primary-structure scaffold at their contact points.

The primary ceramic material used in the production of the sintered scaffold is a waste by-product of coal combustion in power stations, where the ash produced is divided into top and bottom fractions, with further division into additional fractions, one of which has become known by various proprietary trade names, the most common of which is cenospheres. This light, hollow, spherical and elliptical, free-flowing alumino-silicate material is constituted by

- (a) single, hollow spheres, in which wall thickness is approximately 10% of diameter, and
- (b) aggregations of small, hollow spheres which in their formation sintering combine to produce larger aggregated ovoid forms with irregular surfaces that reflect their internal structures.

Industry estimates place annual total world fly-ash production at approximately 400m tonnes [4], with the cenosphere fraction potentially representing perhaps 20m tonnes.

Various of the fly ash fractions are used by the cement and plastics industries, some are incorporated in a range of experimental agricultural programs, others in civil engineering, highway construction and maintenance, but, regardless of the type of application in which they are currently employed, fly ash is an almost insoluble problem for the world-wide electricity-generation industry that depends upon coal

combustion. Recent legislation in India forbids traditional brick making within a five-mile radius of a coal-fired power station unless all manufactured bricks include 30% by weight fly ash. That and similar attempts to increase use of part of the worldwide fly ash stockpile still manages to see only "37 million tons of coal combustion products beneficially used annually [5] in the United States each year", with "more than 81 million tons still being disposed in landfills." Figures to show what percentage of total coal combustion products (CCPs) cenospheres represent are variable, but on the basis of American Coal Council & American Coal Ash Association (ACC&ACAA) estimates and industry breakdown of CCP fractions it may be assumed that cenosphere reclamation within the US alone represents the potential for approximately 5.9 million tons annually (See Appendix 1).

Chapter 2

Literature Review

2.1 Preamble

By the end of the first half of the 19th Century the interest in the physical world that for the previous two centuries had often been the preserve of gifted, wealthy and well educated amateurs was being increasingly formalised. Competition between the nations of Western Europe for trade and empires drove State policy and saw the emergence of institutions both within and outside of existing universities and whose sole function was the systematic investigation of materials, particularly as these results might eventually be applied to industry and trade and the benefit of the State. Likewise, the growth and consolidation of industry in the decades after the first industrial revolution saw the burgeoning development of new sections within manufacturing enterprises whose sole function was the research and development of new materials, new chemicals and new products. Indivisible from the results, and as a consequence of these State and privately funded researches, was an explosive increase in both knowledge and the technology necessary for its production.

In the century after 1850 the period between 1900 and 1950 is regarded by many as the most intensive and productive for the investigation of clay-based ceramic microstructures and the processes inherent in their formation. But by the mid 1930s there was a decrease in the number of papers published with new results of research into clay-based ceramic's properties and structures, this decrease perhaps implying a consensus within the research community that most of the work that could be done had been done. The ceramic-research community began to swing to the emerging field of what quickly became known as "new ceramics". The Second World War

disrupted the accelerating interest in new-ceramics research and into nearly every other aspect of ceramics as well, other than those areas that could be directly applied to the war effort.

Post-war interest in ceramics-based research saw a continuing change in emphasis and location. Emphasis was now clearly moving away from the European-centric dominance of traditional clay-based ceramics, with the locations of that research moving from Europe, principally pre-war Germany and to a lesser extent Great Britain, to the United States of America. Research into the “new ceramics”, non-clay-based ceramics, now occurred in a period without precedent in the history of materials science for its vigour, focus and the scale of the great wealth available from governments and industry to fund their researchers.

Where trade and curiosity to discover and define the unknown had been the driving force in the mid-19th Century, mid-20th Century materials science was defined by an increasing focus on the emerging space race, and the then ten-year-old struggle for nuclear dominance at the heart of Cold War rivalry between the USA and the USSR. Research had become precisely focussed and perhaps less generalist than previously in its application and had moved away decisively from clay-based to non-clay based ceramics.

2.2 Cenospheres.

The physical properties of cenospheres are seen as varying from one coal deposit to another but, regardless of their source, they are agreed to be largely spherical, sometimes elliptical, always hollow to various extents, and enclosed by an alumino-

silicate shell of variable wall thickness, density and structure. Larger elliptical particles will be seen to enclose an alumino-silicate skeleton, which reflects the aggregation of smaller, multiple single spheres within the larger form. Some larger particles will include spheres which will themselves contain smaller single unit spheres.

Cenospheres are described by manufacturers as ceramic balloons and as having diameters between 10-600um, by others as being completely spherical and by others as both spherical and ovoid. Suppliers describe cenospheres as a white free-flowing powder; others see their material as grey. The temperature at which cenospheres melt is stated as greater than 1700°C, for other suppliers it is a material that will melt at 1300°C.

Cenospheres are in commercial use as extenders in plastics, as an integral part of syntactic foams, as additives in insulating paints for industrial applications, as additions in alteration to soil properties for agriculture and even for medical purposes in bandages that absorb wound exudate. The concrete industry makes use of cenospheres in composite sheeting as well as in bridge and road construction, the brick-making industry in India includes fly ash in bricks by legislative interdict. In its industrial applications it is a material that embodies a paradox, in that notwithstanding its widespread use in a range of applications that do not require sintering, its use is characterised not as a material that stands alone, but as a material that by its use alters the properties of an existing materials composite to which it is added. This work presents the results of the sintering fusion of cenospheres and the characterisation of that resultant structure.

There are no data or references that can be relied upon as conclusive in establishing either the total annual world production of pulverised-fuel fly ash or the annual total tonnage of cenospheres recovered from that production.

Cenospheres in pulverised-fuel ash were characterised and their properties defined by *Raask, E 1968* [6]. This seminal paper, the work for which was carried out at the Central Electricity Research Laboratories, Leatherhead, UK, reports that different amounts of lightweight cenospheres are produced by the boilers at different power stations; in some cases the quantity of ash cenospheres is negligible whereas some boilers discharge sufficient to form a thick layer of floating material on lagoons. Table 2.1 shows the percentage of ash cenospheres in pulverised-fuel ash for those power stations listed as ranging from 0.1-4.8%, with chemistry of samples showing similar variation. He observed cenospheres as colourless glass spheres of sizes ranging from 20-200 μm , with a noticeable absence of small particles less than 10 μm . Separation of dried cenospheres into nine different size fractions was performed by sieving, a function found easier in the absence of submicron particles. Variation to the sizes of cenospheres showed that of the floating cenospheres only 5% by weight of particles were less than 50 μm in diameter, whereas dense fly ash has more than 80% below that size and that while density of cenospheres is only a quarter of that of solid ash particles, by volume the cenospheres can amount to as much as 20% of total fly ash from stations sourced. Non-porous walls or shells of cenospheres are reported as 2.0 to 10.0 μm thick, with bulk density of samples varying between 0.25 and 0.35 g/cm^3 and the apparent density of individual particles in the range 0.4 to 0.8 g/cm^3 .

Table 2.1: Densities and thickness of ash cenospheres, after Raask, E [6]

Sample	Upgraded	Particle diameter of graded sample (μ)							
		> 152	120 to 152	105 to 120	89 to 105	75 to 89	63 to 75	53 to 63	< 45
<i>Carrington:</i>									
Real density, g cm ⁻³	2.26	—	—	—	—	—	—	—	—
Apparent density, g cm ⁻³	0.54	0.55	0.53	0.56	0.53	0.54	0.54	—	0.53
Bulk density, g cm ⁻³	0.34	0.32	0.34	0.33	0.33	0.33	0.31	—	0.29
Wall thickness, μ	—	—	5.8	5.0	4.25	3.6	3.0	—	—
<i>Ferrybridge:</i>									
Real density, g cm ⁻³	2.30	—	—	—	—	—	—	—	—
Apparent density, g cm ⁻³	0.58	0.62	—	0.56	0.55	0.57	0.56	0.56	0.61
Bulk density, g cm ⁻³	0.34	0.31	0.29	0.34	0.34	0.33	0.34	0.28	0.35
Wall thickness, μ	—	—	—	5.0	4.3	3.7	3.1	2.6	—
<i>High Marnham:</i>									
Real density, g cm ⁻³	2.02	—	—	—	—	—	—	—	—
Apparent density, g cm ⁻³	0.42	0.44	0.47	0.41	0.43	0.40	0.55	—	—
Bulk density, g cm ⁻³	0.27	0.28	0.28	0.27	0.26	0.25	0.24	—	—
Wall thickness, μ	—	—	5.6	4.1	3.9	2.9	3.5	—	—
<i>Skelton Grange:</i>									
Real density, g cm ⁻³	2.40	—	—	—	—	—	—	—	—
Apparent density, g cm ⁻³	0.62	0.53	0.46	0.61	0.55	0.6	0.63	—	—
Bulk density, g cm ⁻³	0.43	0.32	—	0.35	0.36	0.37	0.36	—	—
Wall thickness, μ	—	—	—	4.5	4.0	3.8	3.4	—	—

Note: In some size fractions there was an insufficient amount of materials for density measurements.

Analysis of gases contained within cenospheres indicates evolution of carbon dioxide and nitrogen within fused silicate glass during their period within the boiler chamber results in their expansion to cenospheres, with gas evolution catalysed by iron oxide.

The composition of gas within cenospheres was analysed by gas chromatography and showed CO₂ and N₂ were the main constituents of gas locked in cenospheres.

Table 2.2: Gas composition and pressure in ash cenospheres, after Raask, E [6]

Sample	Vol. of gas at NTP, cm ³ g ⁻¹				Pressure atm at 20°C
	CO ₂	N ₂	CO	O ₂	
High Marnham	0.27	0.075	< 0.01	< 0.005	0.2
Carrington	0.13	0.13	< 0.03	< 0.01	0.2
Skelton Grange	0.16	0.04	< 0.01	< 0.005	0.18
Ferrybridge	0.19	0.06	< 0.01	< 0.005	0.18

Raask's explanation of the formation of contained gases and their pressures proposes two possible sources of CO₂, dissociation of carbonates and combustion of carbonaceous matter. Calcium carbonate was ruled out as the cenospheres contain

only small amounts of calcium oxide. In addition to calcium carbonate, coal may contain iron carbonate, but the decomposition of iron carbonate is below 600°C, thus the evolution of CO₂ would have been completed well before the siliceous material started to soften. Raask reports that experiments made to observe the gas evolution showed that oxidation of carbon or carbides within the molten silica glass is the most likely source of gas. Raask's experiments proved that an intimate contact of carbonaceous and siliceous matter is required and that the presence of iron is essential.

Raask shows the dependence of cenosphere formation on iron oxide in ash in Fig 2.1:

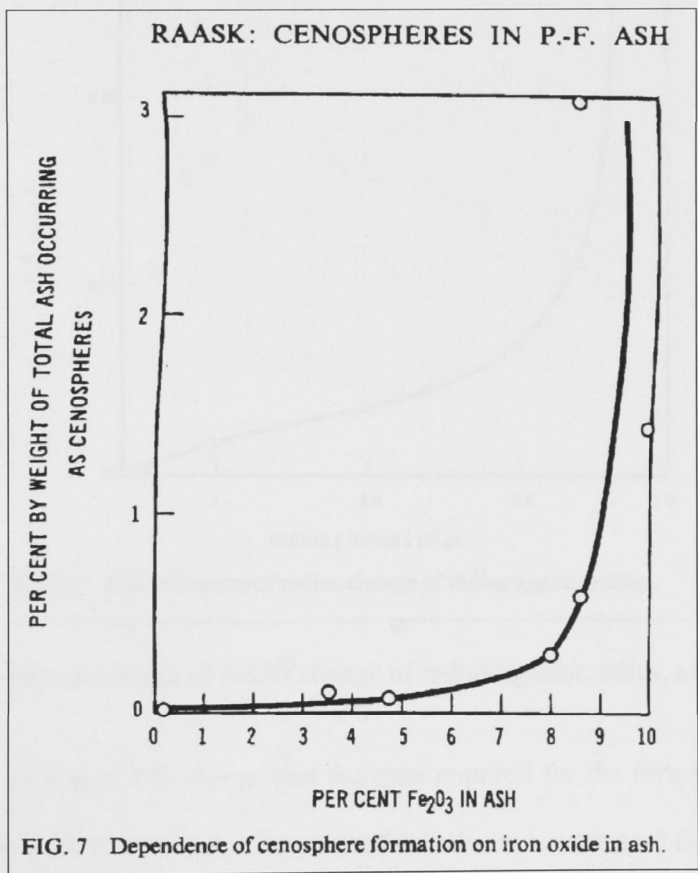
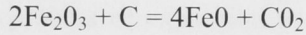


Figure 2.1: Dependence of cenosphere formation on iron oxide in ash, [6]
(Reproduction from a copy of the paper received from inter-library loan)

where the amount of cenospheres in different ashes is plotted against iron oxide content. It is reported that ferric oxide could be the sole source of oxygen to provide CO_2 for the expansion of the molten silica particles by reaction with dispersed carbon:



If this were so it may be calculated that 5-8% of Fe_2O_3 would be required to expand a given particle to cenosphere dimensions.

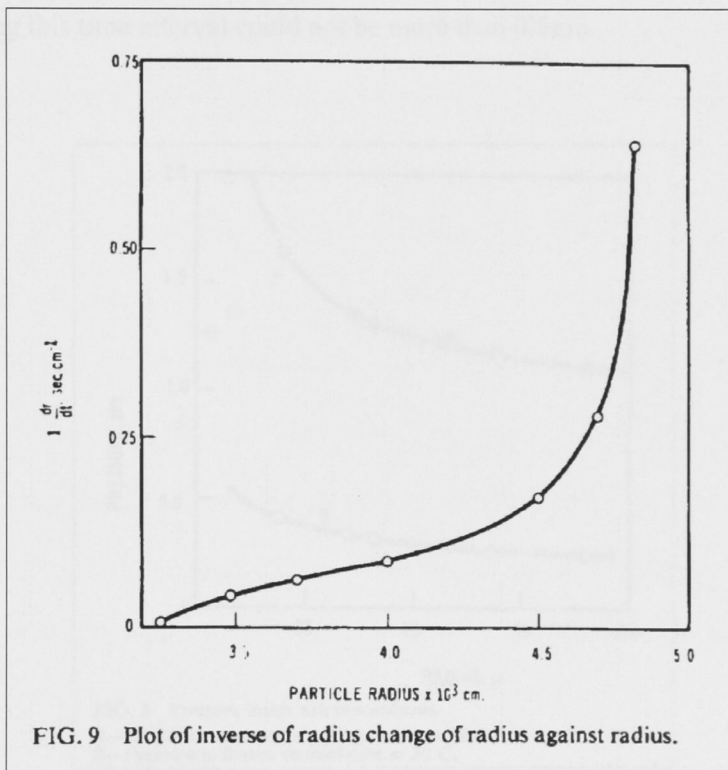


Figure 2.2: Plot of inverse of radius change of radius against radius, after Raask, E [6]

Raask shows in Figure 2.2, above, that the time required for the formation of $50\mu\text{m}$ cenospheres at 1400°C , where the viscosity of the silicate is estimated from the data of *Hoy Roberts and Wilkins* [7] to be 1000 poises and the surface tension of the silicate is $320 \text{ dynes/cm}^{-1}$. The time required for the expansion of the particle to 95% of the

final size is 0.3 milliseconds. Raask further reports that as the pressure inside the sphere approaches equilibrium the rate of expansion slows down, thus the final stage may take several seconds. If too much gas is generated inside the ash particle it will burst leaving a blob and the process of expansion is repeated. Alternatively, if the viscosity is low the particle will explode into small dense particles, the phenomenon similar to that of a bursting soap bubble. On rapid cooling no significant contraction of the cenospheres should take place. A cenosphere having a radius of $50\mu\text{m}$ would take about 50 milliseconds to cool to about 1000°C , thus the decrease in the particle radius during this time interval could not be more than $0.5\mu\text{m}$.

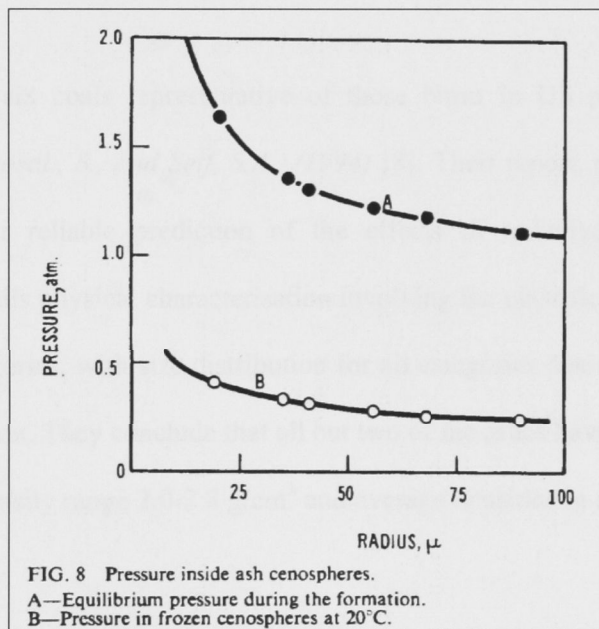


Figure 2.3: Pressure inside ash cenospheres [6]

After freezing, the pressure inside the sphere decreases in accord with Charles' Law and the curve B, Figure 2.3, represents the pressure inside the frozen cenospheres at 20°C , assuming a freezing temperature of 1000°C . The pressure thus calculated is higher than the value, 0.2atm , obtained from gas analysis, Table 4, above. Raask suggests that the viscous contraction of the cenosphere had ceased above 1000°C , but

the results of gas analysis are not sufficiently accurate to evaluate a definite freezing temperature.

In his conclusion Raask writes, inter alia, that the thickness of the shell is about 10% of the radius; the silica content is higher but the calcium oxide is lower in the cenospheres than in the dense material; the ash cenospheres decrepitate on heating to 300°C, a phenomenon probably associated with the release of water dissolved in the glassy material. He further concludes that the formation and size of cenospheres are governed by the viscosity and surface tension of fused silicate glass, by the rate of change in particle temperature, and by the rate of diffusion of gases in the silicate.

The fly ash of six coals representative of those burnt in US power plants were examined by *Ghosal, S., and Self, S.A., (1994)* [8], Their report, part of an effort to provide data for reliable prediction of the effects of radiative heat transfer in combustors, details physical characterisation involving the classification of ashes into six density categories, with size distribution for all categories determined as being in the range 1-200µm. They conclude that all but two of the ashes have mass fractions of $\geq 80\%$, in the density range 2.0-2.8 g/cm³ and average densities in the range 2.1-2.4 g cm³.

A Canadian microscopic study of combustion residues of sub-bituminous and bituminous coals from Alberta, *Gentzis, T., and Chambers, A., (1922)* [9] classified three coals morphologically using reflected light microscopy, concluding that, inter alia, high-volatile bituminous coal produced large isotropic cenospheres having thin and thick walls as well as exploded cenospheres. A study of Greek lignites in the

Ptolemais field, *Georgakopoulos, A., et al, (1994)* [10] shows ash consisting of irregularly shaped, oval and spherical particles, with plerospheres, cenospheres and $<5\mu\text{m}$ spherical particles also present.

The physical, chemical, mineralogical and thermal properties of cenospheres from an ash lagoon in India are reported by *Kolay, P.K., and Singh, D.N (2000)* [11] where a small percentage of the particles present in the pulverised coal ash consist of thin-walled hollow spheres or cenospheres. It is interesting to note that the authors state that the amount of cenospheres or plerospheres contained in an ash normally depends upon its carbon and iron contents and where in general the diameter of cenospheres ranges from 20-200 μm , shell wall thickness varies from 2-10 μm , with density varying from 0.3-0.6 g/cm^3 . The authors concluded that alumina and quartz are the most predominant minerals present in the cenosphere samples, that the particles are seen to be almost uniform in size, with specific surface area quite low. The cenosphere samples were seen to be thermally stable up to 280°C, with the formation of an endothermic peak at around 330°C.

Zheng, Y., and Wang, Z., (1996) [12] examined thermal behaviour of lignite and semi-anthracite coals, in the production of cenospheres, finding highly vesiculated cenospheres rarely developed due to the respective coal's poor thermoplasticity, with corphumanite and textinite having thermal behaviour similar to textinite during pyrolysis. *Gay, A.J, Littlejohn, R.F., and van Duin, P.J., (1983)* [13] discovered cenospheres in fly ash from fluidised-bed combustors, reporting differences between the fluidised bed and more conventional combustors that are likely to affect cenosphere production are indicated. They further reported, that fly ash from

fluidised-bed combustion of bituminous coals contains carbonaceous cenospheres of several forms, thick-walled, opaque and transparent with a skeletal structure as well as balloons without skeletons.

Ozdemir, O., and Celik, M.S., (2002) [14] characterised fly ash as unburned carbon, iron compounds, typically of magnetite, pozzolanic material and cenospheres, conducting a systematic study to optimum conditions for the separation of these materials from fly ash.

The use of cenospheres in the production of a new light weight inorganic polymer was proposed by *Wu, H-C., and Sun, P., (2005)* [15], using Class F fly ash, metakaolinite and light weight aggregate, and small amounts of sodium hydroxide and sodium silicate solution in the fabrication of a geopolymer, first proposed as a new class of three dimensional alumino-silicates by Professor Joseph Davidovits in the 1970s. They reported cenospheres as hollow, alumino-silicate, micro-ceramic balloons, with low density, low shrinkage and high strength from their outer shell and superior thermal stability. Low specific gravity (0.64) and small diameter made them ideal replacement for sand in the production of light-weight concrete.

A potential use of cenospheres is noted by *Ayers, S.R., and Van Erp, G.M., (2003)* [16] who report a new class of structural core material applicable to composite materials in civil and structural engineering where vinyl ester resins and cenospheres are combined. *Cardoso, R.J., Shukla, A., and Bose, A., (2002)* [17] presented findings of the effect of particle size and surface treatment on constitutive properties of polyester-cenosphere composites, using hollow alumino-silicate spheres ranging from

10-400 μm diameters as a filler in an homogenous polyester composite, reporting that amongst other findings, fracture toughness increased with particle size reduction.

Additional study of hygrothermal properties of syntactic foams, commonly used as core materials in composite sandwich structures for weight sensitive applications, was carried out by *Gupta, N., and Woldesenbet, E., (2003)* [18]. Epoxy resin was used as the matrix material where the distribution of outer diameter cenospheres added to two resins was the same. Results of compression tests were compared with those of dry syntactic foam samples.

Freeform fabrication of aluminium metal-matrix composites were examined by *Souvignier, C.W., Sercombe, T.B., et al, (2001)* [19] who reported that a series of metal-matrix composites were formed by extrusion freeform fabrication of a sinterable aluminium alloy in combination with silicon carbide and whiskers, alumina particles and hollow fly ash cenospheres. They further found that this fabrication method also allows composites to be formed with hollow spheres that cannot be formed by other powder or melt methods. A metal matrix syntactic foam was created by *Rohatgi, P.K., Kim, J.K., et al, (2006)* [20] who reported loose beds of cenospheres being pressure infiltrated with A356 alloy melt using applied pressure up to 275 kPa, where the volume fraction of cenospheres were in the range of 20-65% and processing variables included melt temperature, gas pressure and the particle size of the fly ash.

Working on the fabrication and characterisation of ceramic foams based on a silicon carbide matrix and hollow alumino-silicate spheres, *Ozcivici, E., and Singh, R.P.,*

(2005) [21] also report incorporation of two different grades of cenospheres into a silicon carbide matrix, where the matrix was formed through the pyrolysis of a pre-ceramic polymer, with multiple polymer infiltration and pyrolysis cycles employed in the minimisation of voids. Thermal conductivity and thermal expansion properties for both 5-100 and 5-500 μm cenosphere-based materials were measured as a function of the number of re-infiltration cycles with laser flash technology employed to measure thermal conductivity.

Cenospheres as a component of emulsion explosives are reported by *Anshits, A.G., Anshits, N.N., and Deribas, A.A., et al, (2005)* [22] where cenospheres 50-250 μm diameter were added to an emulsion explosive as a sensitiser and variation to detonation velocity was measured as a function of variation to particle diameter.

The role of cenospheres in cracking in fly-ash-bearing cement pastes was reported by *Montgomery, D., and Diamond, S., (1984)* [23], where compact-tension specimens were prepared from a cement paste with an especially high content of cenospheres. It was found that an advancing crack, even after extensive ageing, typically went around the cenosphere-paste interface rather cleaving through the cenosphere itself, thus appearing to act as energy dissipating inclusions in fracture and not necessarily weakening the system. *Tiwari, V., et al, (2004)* [24] reported investigation of the effect of the addition of cenospheres to a cement matrix, with experimental results showing that a 40% volume fraction addition increased the noise reduction coefficient by 100%, where in a cenosphere-rich cement the sound absorption coefficient of asphalt concrete decreased with an increase to the cenosphere volume fraction.

The immobilisation of cesium and strontium radio nuclides in framework aluminosilicates using cenospheres, where calcination and solid-phase crystalline stages are utilised was reported by *Vasil'eva, N.G, et al, (2005)* [25]

Electroless copper coating of cenospheres using a silver nitrate activator was investigated by *Shukla., S., et al, (2001)* [26] where AgNO_3 was used to successfully achieve a uniform and continuous Cu coating of cenosphere surfaces.

2.3 Sintering

Sintering is a topic area that is now long understood and reported upon. Since ancient times potters have understood the role of the application of increased heat as essential to the achievement of the changes that we know as sintering. Archaeologists cautiously propose that the first sintered objects were probably made in Mesopotamia some 10,000-12,000 years BP and saw the first consideration of the transforming link between heat and clay.

This entirely empirically based process brought slow change over thousands of years to the process of making pottery with an equally slow accretion of the knowledge of cause and effect. Temperature could only be assessed optically, certain colours in the chambers of potters' kilns were known to produce particular desirable qualities and equally others were not associated with success. The change necessary to produce what we understand as a reduction firing in a kiln was accompanied by smoke and flame from its chimney and stoking ports and reduced clarity in the kiln's chambers, an oxidising firing was the opposite, clarity in the chamber and no sustained smoke and flame from chimney and stoking ports. It was not until the mid 19th Century that

the connection between heat applied to ceramic objects and the creation of different structures within its constituent particles would be formally examined and described.

Hermann Salmang, in *Ceramics: Physical and Chemical Fundamentals*, [27], gathers, organises, elucidates and cites 612 papers that published the results of research into all aspects of the chemistry and physics of clay between 1821 and 1955. It is beyond the scope of this thesis to attempt to summarise Salmang's monumental compilation and explanation of the reported findings of one hundred and thirty four years. More recently *Kingery, Bowen and Uhlmann*, [1], and *Barsoum*, [2], have added their significant contributions to the greater understanding of the field. I acknowledge my dependence upon the work of these five writers in achieving an understanding of the processes and mechanisms inherent in the sintering of ceramic materials generally and particularly insofar as they touch upon and inform my investigations reported here.

2.4 Granular systems

Tsoungui, O., Vallet, D., and Chamet, J-C, 1998 [28] report the results of experimental studies into the distribution of contact forces within two-dimensional granular packings with binary size distribution, composed of water softener salt discs of uniform thickness, under an oedometric compression. In the mechanics of soils and rocks the analysed media are frequently considered as discontinuous or granular. It is then possible to use physical models made of spheres, or of discs loaded in their plane, to better understand the distribution of forces between grains. Using photo-elastic visualisations, these models provided striking evidence of the heterogeneous distribution of inter-particle forces in a granular system on a scale definitely larger

than the typical particle size. Tsoungui, O., et al, [28], report that these heterogeneities are generally responsible for many unusual properties of granular media.

Computer simulations enable the capture of some of the aspects of the packing of grains under compression and the authors propose an experimental method leading to the determination of particle-particle contact forces that involves the direct measurement of contact area traces left on particles in contact. Using water-softener discs of uniform thickness it is possible to measure the irreversible trace left on the discs after contact.

Figure 2.4, below, shows a network of normal contact branches in a sample after computer analysis, where each disc is identified by a number. Contact branches are drawn from the centre of one particle to that of the adjoining particle through its contact point at the circumference of each.

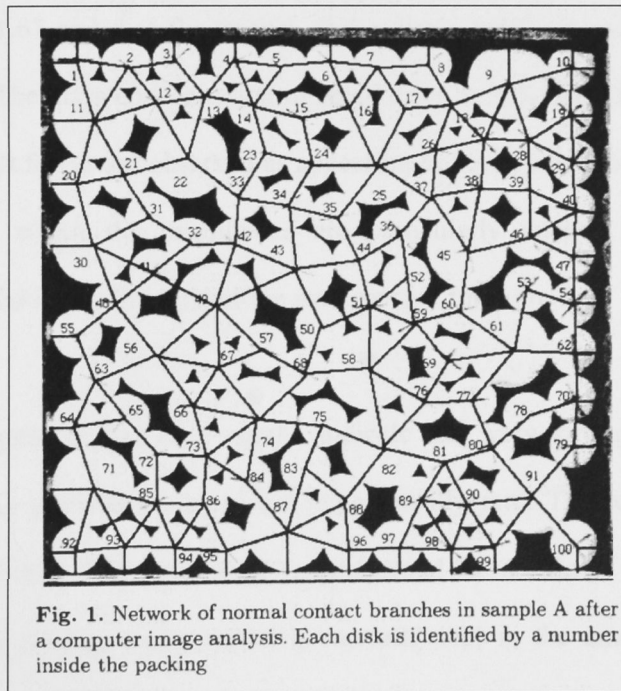


Figure 2.4: Network of normal contact branches in sample [28]

Figure 2.5 shows restoration of the network of normal forces in a sample after computer image analysis, where forces are encoded as the width of inter-centre segments.

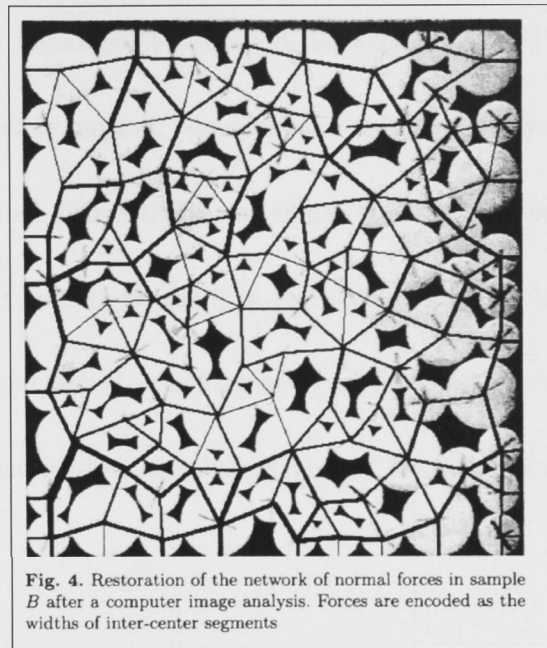


Figure 2.5: Restoration of normal forces in sample [28]

Experimental results show that the size ratio of the largest and smallest discs is approximately 1.67 and that fluctuation of the disc's radii is less than 5% of their average value. The mass concentration of small discs is 50% and 65% in Figures 2.4 and 2.5. Contact forces are observed as appearing to be very heterogeneous, forming “chains” along which the magnitudes are particularly intense, with the chains generally oriented in the direction of the macroscopic force applied.

The authors conclude that their results indicate that very strong particle-particle contact forces in granular packings are exponentially rare. The relative agreement between simulation data and their experimental tests shows that the direct measurement of contact areas can be a powerful tool in the analysis of granular assemblies.

He, D., and Ekere, N.N., (2001) [29] reported the application of a Monte Carlo technique to simulate the structure of concentrated suspensions of hard spherical particles that obey lognormal distribution. Structures reported in their study were shown to be completely random, homogeneous and isotropic by statistical tests. With particles of lognormal distribution both the gap sizes and the neighbouring numbers are distributed over broader ranges than that with equal particles. Their results also show that with equal particles and particles of lognormal distribution, there is no significant difference between the distributions of the solid-area distributions on the cross sections.

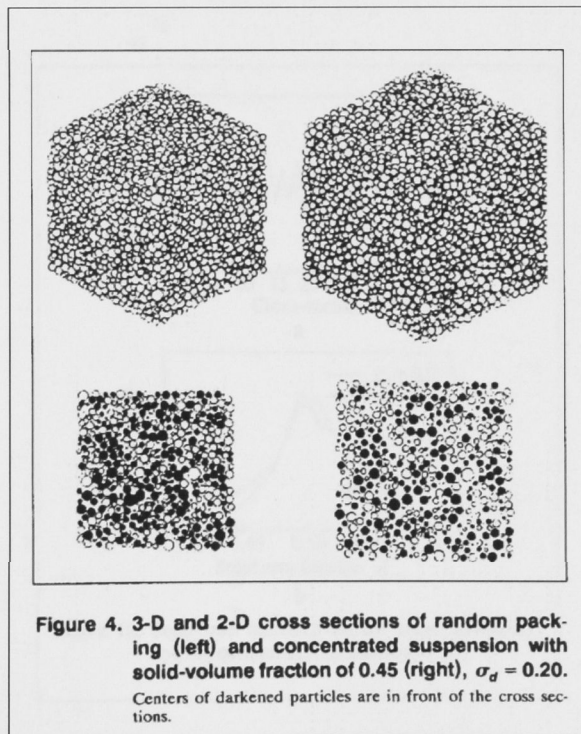


Figure 2.6: 3-D and 2-D cross sections of random packing and concentration suspension with solid fraction [29]

In random packing of particles there exist both close contacts and near contacts. Theoretical analysis does not take the near contacts, such as particle i and particle j , below, Figure 2.7, into account. However, because the hydrodynamic interaction between these two particles may be stronger than between particle i and a smaller particle, such as particle k , it should be taken into account.

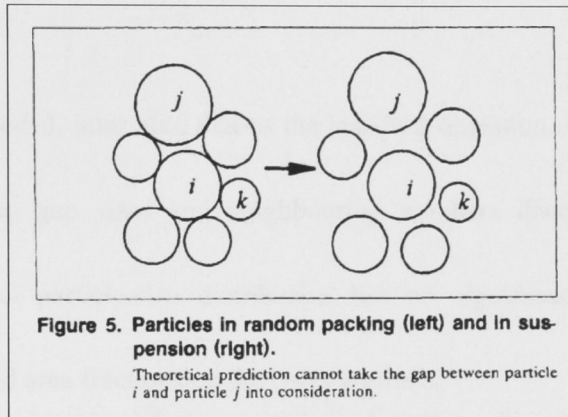


Figure 2.7: Particles in random packing and in suspension [29]

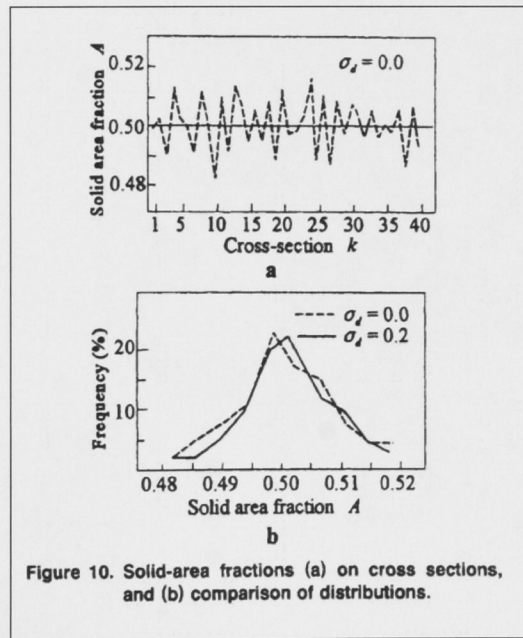


Figure 2.8: Solid-area fractions [29]

Figure 2.8 shows solid-area fractions (a) on cross sections and (b) comparison of distributions. To evaluate the structure on a macro scale, each simulation was cut by forty equally separated cross sections, see Figure 2.6 above, and the distribution of the solid area fractions was examined.

The authors concluded, inter alia, that as the standard deviation of particle diameters increases, both the gap sizes and neighbouring numbers distribute over broader ranges. In contrast particle-size distribution has no significant influence on the distribution of solid area fractions on the cross sections.

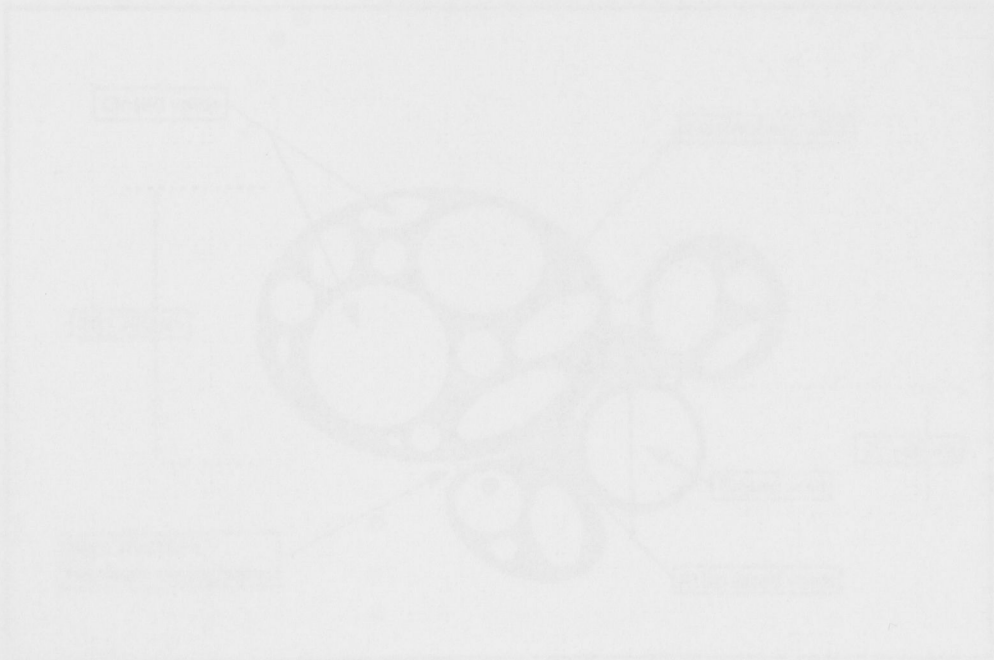


Figure 2.8: Schematic of an experimental model of the ordered mesoporous structure. The labels indicate the position of the pore, particle, neighbouring number, gap size, and particle size.

Chapter 3 Theoretical model

3.1 Microstructure

Figure 3.1 below shows a diagrammatic representation of the ceramic material's sintered structure and cross-section details, showing:

- a) variation to geometry, sizes and internal structures, where single or multiple closed voids are contained within cenospheres
- b) neck structures joining the cenospheres that are formed during sintering from alumino-silicate materials
- d) articulated interstitial spaces between fused cenosphere-plus-neck combinations, with open porosity (estimated as within the range 35-40%)

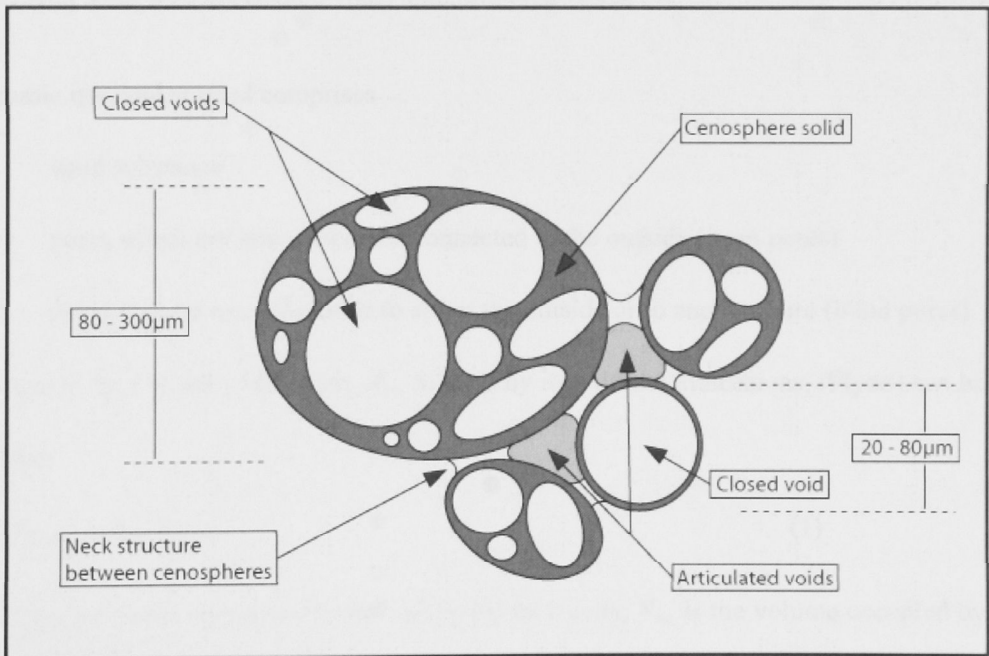


Figure 3.1: Geometrical and morphological model of the sintered cenosphere structure. Dimensions shown are indicative of possible size ranges.

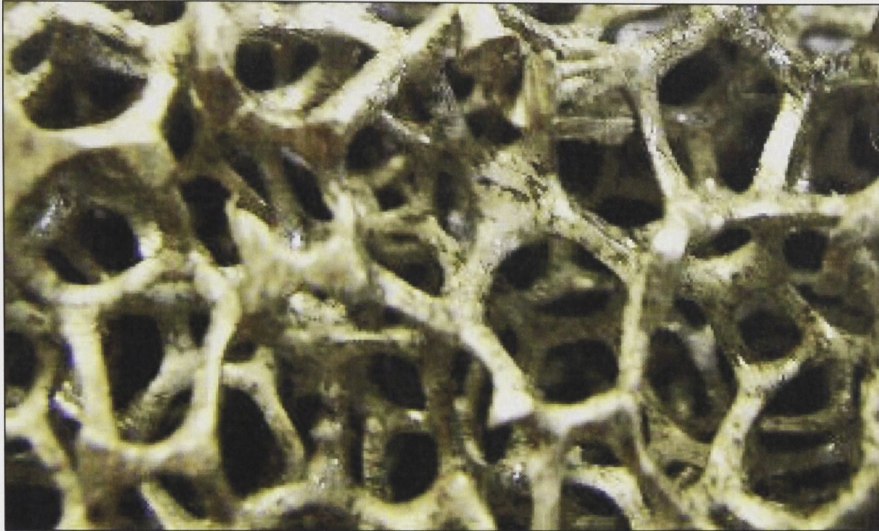


Figure 3.2: Photographic image of an expanded aluminium foam structure, x10

Figure 3.2 shows for comparison with Figure 3.1 the less-complex microstructure of a foamed metal solid with articulated voids and no closed voids.

The ceramic material studied comprises

- (i) solid substance
- (ii) pores which are articulated and connected to the outside (open pores)
- (iii) pores that are not articulated to either the outside or to another pore (blind pores).

In such a case the volume of the body, V_b , defined by its external dimensions, (Flynn) can be divided into:

$$V_b = V_s + V_{op} + V_{sp} \quad (1)$$

Where V_s is the volume occupied by the solid substance only, V_{op} is the volume occupied by the open pores, and V_{sp} is the volume occupied by the sealed pores.

A single-void cenosphere particle (diameter range 45-150 μm), is generalized as having a wall thickness that is approximately 10% of its external diameter, where direct observation of single-void particles shows wall thickness can vary from >3% to <15% of overall diameter. When single-void particles of the same diameter are isolated and compared, it is seen that wall thicknesses are not identical.

As average particle-size diameter increases beyond 150 μm , the proportion of single-void particles decreases, with single-void particles appearing to be less than approximately 5% of particles within the range 180-300 μm . The geometry of particles also varies as a function of increase to particle size, so that single-void spherical particles are increasingly replaced by particles that are ovoid or elliptical, with surface irregularities reflecting their structures as aggregations of small-diameter spheres. The thickness of the walls that define and separate the smaller internal spheres themselves vary unpredictably, with thickened wall sections seen as including very small completely contained spherical voids.

Where in a traditional clay-based structure it can be shown conclusively that the articulated void fraction can be both measured and predicted as a function of particle size and sintering temperature, this appears not possible in the use of cenospheres. The combination of particles of differing equivalent spherical diameters, geometries, densities and surface profiles produces an articulated void fraction which, because of these factors, will necessarily vary in its sectional volumes and cross-sectional geometry and measurements, while also being predictable within a narrow range of values for its total volume in large-number sample measurements.

In addition to variation to articulated void-fraction volumes described above, a further variable is seen where the surface of individual cenosphere particles has been fractured, thus opening access to inner voids that are otherwise contained within an intact cenosphere's outer shell. When such access occurs the inner-void volume then becomes an integral part of the structure's larger, articulated-void fraction and thus must also be considered part of the structure's tortuosity. The random distribution of cenospheres of differing sizes, volumes and densities that differ in their packing one to another, as well as in the distances between close but not-touching particles, suggests that while total void volumes can be calculated, volumes will vary unpredictably from one section of a given sample to that of another.

3.2 Determination of porosity

The determination of total articulated porosity volume presents an additional problem. In clay-based ceramics *apparent porosity (AP)* is defined by *Singer & Singer (1971)* as,

$$AP\% = \frac{\text{Wet wt of sample} - \text{Dry wt of sample}}{\text{Dry wt of sample}} * 100 \quad (2)$$

Where *Dry weight* is the weight of the sample without any water (moisture) and dry weight of the sample determines the mass of the solid substance and *Wet weight* is the weight of the sample with pores completely filled with water.

If the solid substance is made up of a number of different constituents, then the mass of the solid, defined by its weight, is the sum of the masses of the individual constituents. Given the volume fraction of each constituent solid and assuming the simple law of mixtures, we have the relationship for the density of the solid:

$$\rho_s = \rho_1 v_1 + \rho_2 v_2 + \rho_3 v_3 \dots \rho_n v_n = \sum_{i=1}^n \rho_i v_i \quad (3)$$

where v_1, v_2, v_3 , etc, represent the volume fractions of the individual constituents and ρ_1, ρ_2, ρ_3 , etc, are their corresponding densities (Flynn).

The increase in the weight of the wet sample is assumed to be due to water ingress through open pores. Assuming that water fills all of the open pore spaces, then $V_{water} = V_{op}$ and therefore the volume fraction of open pores can be calculated from,

$$v_{op} = \frac{V_{water}}{V_{body}} = \frac{m_{water} * \rho_{body}}{m_{body} * \rho_{water}} \quad (4)$$

where:

m_{water} is measured by weighing

m_{body} is measured by weighing

$\rho_{body} = \frac{m_{body}}{V_{body}}$ and volume is measured by dimensions

$\rho_{water} = 1$ (assumed value)

In the cenosphere-based ceramic the distribution of actual or equivalent spherical diameters of cenosphere particles is random and the density of individual cenosphere particles is unknown because the internal void-volume fraction of those particles varies randomly and is not able to be predicted. There are only two non-cenosphere materials used in the cenosphere-based ceramic where density and constituent weights are known and where the equations appropriate to a dense, sintered clay-based ceramic might obtain. However the weights of these two materials combined constitute only ~19% of the whole. Where in a

porous solid total porosity is known, articulated porosity can be measured and hence closed porosity can be calculated.

3.3 Permeability

A porous medium or material may be defined as a solid that contains within its structure an interconnected or articulated network of pores that may be filled with a fluid or a gas. The interconnected void fraction is assumed to be continuous in three dimensions and is defined by and exists simultaneously with the structure's solid fraction, so producing two continuously interdependent scaffolds or matrices.

Naturally occurring structures such as rocks, foams and woods as well as bone are considered as porous media, with manufactured materials further including ceramics and expanded metallic foams.

Flow through porous media was first described by Darcy, who established the proportional relationship between the instantaneous flow rate through a porous medium, the viscosity of the fluid and the pressure drop over a given distance,

$$Q = \frac{-kA}{\mu} \frac{Pb - Pa}{L} \quad (5)$$

where Q is the flow rate defined as the unit of fluid volume per unit time, k is a constant expressed in units of area of the medium, A is the cross sectional area to flow, and $(Pb - Pa)$ is the pressure drop, μ is the dynamic viscosity in units of Pa.s and L is the length over which the pressure drop is taking place.

Chapter 3 Theoretical model

In this structure, where the volume of added powdered ceramic materials is increased, that increase will further occupy spaces between cenosphere particles. The result of such increase is reduction of available cross-sectional area and hence reduced permeability. If neck thickness is reduced the results will be reduction of available void cross-sectional area and reduced permeability.

But not all the fluid that fills the voids within a porous medium flows when a pressure difference is applied. Part of the fluid remains stagnated because of tortuosity and does not contribute to the fluid flow rate. The effective porosity that contributes to the flow can be defined as

$$\varepsilon^* = \frac{\text{vol. occupied by the flowing fluid}}{\text{total structure volume}} = \frac{V_F^*}{V_T}$$

If a porous structure is fed with a fluid with a volumetric rate Q , then:

$$Q = \frac{\text{volume of flowing fluid}}{\text{time}} = \frac{V_F^*}{t^*} \quad (6)$$

where t^* is the time of flow through the medium.

Therefore, measurement of Q includes the effect of tortuosity on sample ultimate permeability.

3.4 Elastic modulus

One of the most commonly used generic equations that describes the effect of porosity on mechanical properties is

$$X = X_0 \exp(-bVfp) \quad (7)$$

Where X is the mechanical property, Vfp is the volume fraction of porosity, b is an empirical constant and the subscript 0 indicates zero porosity [24].

Lu, et al (1999) [24] reported analysis of the relationship between porosity and the elastic modulus of porous materials. They state that the existing theoretical models are suitable for limited cases and some are mathematically complicated. They propose a new micromechanics model to explain experimental results for materials of porosity less than approximately 30%. One existing theory is employed for foams with porosity values greater than 30%.

The shear modulus of the porous material μ which is defined as

$\mu = \bar{\sigma} / \bar{\gamma}$, is given by

$$\frac{\mu_0}{\mu} = 1 + \frac{15(1 - \nu_0)}{7 - 5\nu_0} \phi \quad (8)$$

And similarly, the bulk modulus, k , of the porous material can be obtained as

$$\frac{k_0}{k} = 1 + \frac{3(1 - \nu_0)}{2(1 - 2\nu_0)} \phi \quad (9)$$

In the above two equations, μ_0 , ν_0 and k_0 are the elastic moduli of the material when the porosity is zero and ϕ is the total porosity. The Young's modulus, E , is related to μ and k by

$$E = \frac{9k\mu}{3k + \mu} \quad (10)$$

As the parameters μ_0 , ν_0 , E_0 and k_0 are inter-dependent, the authors report that ultimately the elastic modulus E is dependent upon the value of the initial value of the elastic modulus

(when porosity ϕ equals to zero) E_0 and the initial value of the Poisson's ratio ν_0 . The value of the Poisson's ratio in general is about 0.3 for ceramics. Numerical calculations show that the results are insensitive to the value of ν_0 in this range. Therefore, the elastic modulus mainly depends upon the value of E_0 .

$$E = E_0 \exp(-b \frac{V_{fp}}{E}) \quad (11)$$

3.5 Strength and fracture of porous ceramic sintered from spherical particles

Krasulin, *et al*, (1980) [25] report the mechanical properties of ceramics obtained by the sintering of stabilized zirconia microspheres and report strength at compression and tension, elastic deformation and modulus of elasticity at compression, specific works of fracture, of fracture initiation and stress intensity were determined.

Mechanical properties of porous material depend upon peculiarities of microstructure. In known expressions, peculiarities of microstructure and its effects on strength are, as a rule, taken into account through empirical coefficients. However, some of them indicate the necessity to form structure elements in order to minimize the stress concentrations.

According to Weiss [26], the stress concentration coefficient in porous material of grain structure may be written as

$$K_{\sigma} = K_1 K_2 [\rho / (\rho + 2y)] \quad (12)$$

where K_t is the stress concentration coefficient in the contact region between grains, depending on the geometrical form of the contact; K_b is the coefficient of stress concentration occurring due to defects in the contact; ρ is the radius of curvature in the contact profile and y is the distance of the defect from the contact edge.

As can be seen from eqn. (12), the value of K_σ is minimal when pores have a round shape and there are no defects in the contact. Such a type of macrostructure of a porous sample may be obtained, for example, by using grains of a spherical form.

3.6 Strength as a function of porosity

The structure is to a large extent determined by particle-size distribution of cenospheres, which constitute approximately 87% of volume, when sintered at temperatures up to 1400°C. The neck fraction formed during sintering from added ceramic materials principally affects porosity rather tortuosity and we therefore assume that changes to measured permeability are indicative of changes to porosity. We infer a relationship between permeability and porosity from Darcy's law.

Chapter 4

Experimental Methods and Techniques

4.01 Factors considered in the choice of raw materials

It was assumed that the structure needed to be sintered to acquire the strength otherwise absent in unsintered ceramic powder compacts. It was also assumed that the structure would be a compound material comprised by a number of materials that, as a function of their composition, their particle sizes and their distribution, would offer the potential for fusion at their contact points, so presenting the possibility of the creation of a network of interconnected voids.

While the temperature at which such a hypothetical articulated-void fraction would cease to be patent was unknown, it is clearly established that conventionally sintered clay/mineral compounds can be reliably regarded as porous in the range 900-1050°C. Sintering to 1000°C over approximately 8 hours is the general industrial and studio standard for biscuit or first-fired ware that is intended for subsequent glaze application and firing to maturation. We chose 1000°C as the starting point at which both higher and lower maximum temperature experimental sintering cycles should begin. It was thought possible that results might indicate a range of temperature maxima extending both above and below 1000°C. The possible extent of such a temperature range was unknown.

The choice of materials for use in combination in initial experiments was informed by our knowledge of individual material's sintered properties and potential for the achievement of specific eutectic temperatures. The possibility offered by the use of one material in

combination with another or others would be considered, tested, retained for examination and additional development or discarded. We held no fixed expectations as to outcomes and insofar as it was possible the conventions and limits explicit in the rubric of traditional ceramics' usage were ignored.

4.02 Sintering of samples

The first sintering of materials combinations was carried out in a 10cuft, directly observed, manually controlled pottery kiln in the Ceramic Workshop, National Institute of the Arts (NITA), Australian National University. Sample sintering rates and firing end-points were monitored by direct observation of Orton Seger pyrometric cones. Testing continued in that kiln until it was established that a strong, porous ceramic structure had been achieved. At that point it was obvious that a reliable, computer-controlled furnace, highly accurate in both control and recording of all aspects of firing cycles and temperatures, was required. Controlled multiple replicating firings were fundamental to the successful characterisation of the structure and the determination of its properties at successively higher temperatures. The Ceramic Workshop kiln displayed significant temperature variation within the volume of its packing space and was not able to deliver the accuracy required.

A computer-controlled furnace in the School of Aerospace, Civil & Mechanical Engineering (ACME), Australian Defence Force Academy (ADFA), Canberra, ACT, was next used to replicate results of firings performed in the NITA kiln. While the ADFA furnace was computer controlled and more accurate in the management of firing ramps

than its manually controlled predecessor, assessment of temperatures using Seger Orton cones set at multiple points along the length of its chamber showed significant variation, so rendering unreliable the results of sintering of multiple samples distributed along its length. Data from this series of firings were discarded and not included in this study.

Enquiry to the Materials Division, Australian Nuclear Science & Technology Organisation (ANSTO), Lucas Heights, New South Wales, revealed a computer-driven Laser Dilatometer Furnace. This furnace incorporates a laser dilatometer and allows the use of an infinitely variable firing cycle between ambient and 1550°C as well as the simultaneous recording of temperature and measurement of dimensional changes to multiple cylindrical samples at all points of any designated sintering cycle. This furnace was used in the sintering of every materials-combination sample for all of the the experimental programme in the characterisation of the porous-ceramic structure's properties.

4.03 Purchase of materials

All materials used in this study were purchased from commercial suppliers of manufactured ceramic materials, all are in daily use by the ceramics and other industries in applications not related to this work. Purchased materials were not then subject to any further processing, refinement, addition or alteration other than for being combined with other materials.

Materials that were rare, expensive, or required complex compounding, additional pre-use sintering or other preparation, or which were known to be compounds developed for specialized applications, or otherwise limited in their application were not considered.

It was necessary for chosen materials to be capable of being used in combinations appropriate to the range of temperatures contemplated, while also allowing the possible achievement of new properties, or properties at least reflecting or similar to those already exhibited in traditional non-porous sintered ceramics.

4.04 Description of materials used in precursor experiments

- Table salt
- Crushed brick
- Diatomaceous earth
- Kaolins and ball clays
- Liquid clay suspensions
- Lithium carbonate
- Polystyrene balls
- Powdered, commercial manufactured clays
- PVA glues
- Sawdust
- Sodium bicarbonate
- Sodium carbonate
- Sodium silicate
- Vermiculite

4.05 Precursor experiments in evaluation of materials

The materials listed in 4.04, above, were mixed either alone or in combination with kaolin or ball clays or liquid clay suspensions as the matrix to which one or more materials were added. The resultant compounds were variously dried, subjected to cold isostatic pressing (CIP) while unsintered, sintered after CIP, fracture faces were viewed and thin sections prepared for visualisation of sample structures using SEM. In each case materials chosen for sintering were fired in air to a maximum firing temperature of 1000°C.

SEM imaging and empirical observations did not establish evidence of the existence of an articulated void fraction in any of the materials combinations tested and all further testing of such materials combinations was abandoned.

4.06 Material used in the formation of the primary structure

4.06.1 Cenospheres

The primary material that depending upon constituent materials ratios can constitute between 60-90% of the sintered ceramic structure, are cenospheres, fine, dry, free-flowing powders that constitute approximately 3-5% fraction of fly ash, and are a waste by-product of coal combustion in electricity generation. Total world production of fly ash is estimated to be approximately 400m tonnes, with a potentially recoverable cenosphere fraction representing 12-20m tonnes. A reliable figure for actual world annual recovered-cenosphere tonnages is not available for any year.

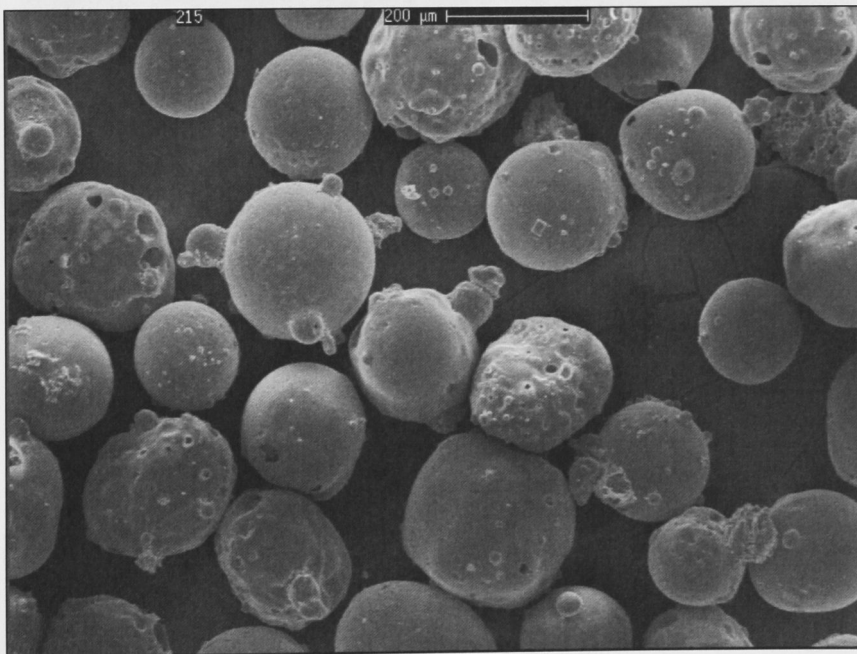


Figure 4.1: Electronmicrograph of SL500 grade cenosphere particles, x80

The literature describes cenospheres variously as a free-flowing white powder comprised by hollow alumino-silicate spheres in which wall thickness is approximately 10% of diameter. Available particle diameters are claimed to lie between 2.00 μm to 350 μm , but suppliers are either unable or reluctant to provide large-volumes of samples <45 μm and >250 μm , because of their relatively low distribution in bulk unsieved batches of recovered cenospheres.

Figure 4.2 shows SEM visualization of polished thin-sections of single spherical cenosphere particles where wall thickness varies and is less than 10% of diameter. As sample diameter increases beyond a nominal 80 μm , increasing numbers of individual particles are seen that are sintered ovoid aggregations of small, spherical particles, with surface irregularities reflecting the irregular diameters and distribution of their constituent particles.

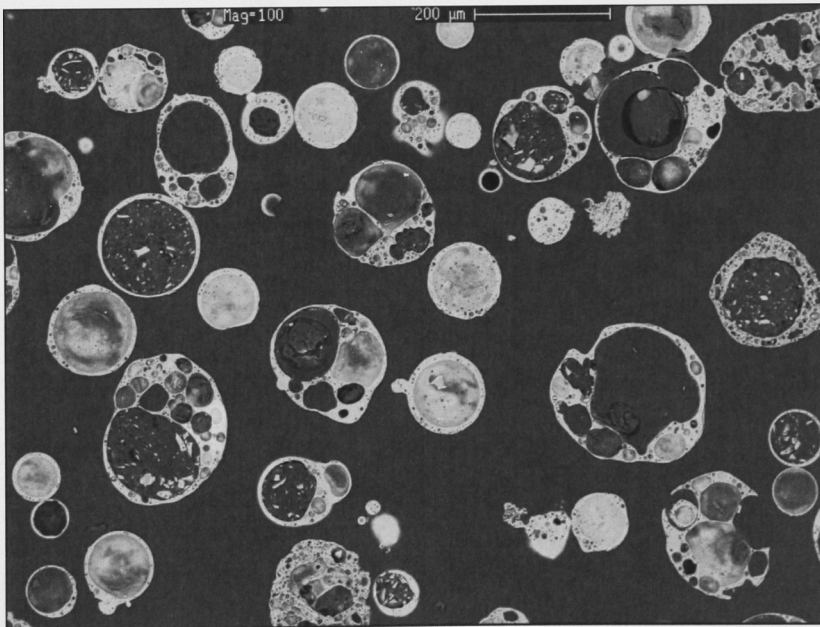


Figure 4.2: Electron micrograph of polished 30 μm thin section of SL500 cenospheres, x100

4.06.2 Cenospheres, available grades

Table 4.1: Cenospheres, marketed as econospheres, available grades, size ranges and diameter means

Grade	Nominal particle size range in microns	Approximate particle mean in microns
SLG	20 - 300	130
SL500	250 - 500	300
SL350	250 - 350	270
SL300	150 - 300	150
SL180	20 - 180	115
SL150	20 - 150	100
SL125	12 - 125	80
SL75	12 - 75	45

4.06.3 Description of cenosphere materials

This material is a waste by-product of coal combustion and a fraction of total fly ash production. Its supplier describes it as follows, (See Appendix 2, 3).

Table 4.2: E-Spheres, SL500 grade, supplier's technical specifications and physical properties:

Technical details	Physical properties
Form	Free flowing white powder
Particle size	250-250µm
Colour	White
Relative density	0.6-0.8g/cm ₃
Bulk density	0.4 g/cm ₃
Shell thickness	Approx. 10% of diameter
PH of water dispersion	6-8
Melting Point	1600-1800C
Compressive strength	45Mpa
Hardness	6 Moh's scale
Refractive index	1.53
Thermal conductivity	0.1W/m/Deg C
Oil absorption	7g/100g
Chemical properties, by weight	Typical
Silica	55-60%
Alumina	36-40%
Iron oxide	0.4-0.5%
Titanium dioxide	1.4-1.6%

4.06.4 Materials used in the formation of secondary structures

Frit DA4914
Kaolin, Eckalite #1

4.07 Choice of maximum sintering temperature range, °C

Limits on access to the ANSTO Materials Division laser-dilatometer furnace and to the number of standard samples that could be packed in its chamber for any one firing, required the design of a firing schedule that would include a sequence of six progressively higher maximum temperatures in the range 1100-1500°C for Groups A, B and C. Groups A-F were each fired to the benchmark initial firing point of 1000°C and subsequently to 1400°C, with Group G fired once to 1300°C.

Table 4.3: The range of sintering temperatures, °C, to which each of the specified materials Groups was fired.

Sintering temperature °C								
Group	1000	1100	1200	1300	1400	1400 (1)	1450 (2)	1500
A	•	•	•	•		•	•	•
B	•	•	•	•	•	•	•	•
C	•	•	•	•		•	•	•
D	•				•			
E	•				•			
F					•			
G				•				

Table 4.4: Identification of material's groups by sintering temperature, °C, and by constituent materials

Materials Group and Additions		Sintering temperature °C							
Group	Additions	1000	1100	1200	1300	1400 (2)	1400 (2)	1450	1500
A	Base	•	•	•	•		•	•	•
B	Base + silica fume +tin oxide	•	•	•	•	•	•	•	•
C	Base + silica fume + tin oxide + cobalt carbonate	•	•	•	•		•	•	•
D	Base + silica fume	•				•			

4.08 Constituent materials ratios by Group

4.08.1 Group A

Table 4.5: Group A, weight of constituent materials, g

Sample No	SL500 g	Frit DA4194 g	Kaolin g	Water ml
1-10	10	2.0	0.35	6.0

Group A is the materials-combination group upon which all subsequent variations are based. (For particle-size details of Kaolin see Appendix 4, 5). Samples of this Group were sintered to each of the temperature intervals specified in the range 1100°C and 1500°C, see Table 4.4. (For particle-size details and constitution of Frit DA4194 see Appendix 6, 7)

Group 4.08.2: Group B**Table 4.6:** Group B, weight of constituent materials, g

Group B	SL500 g	Frit DA4194 g	Kaolin g	Water ml	Silica Fume g	Tin oxide g
1	10	2.0	0.35	6.0	1.0	0.1
2	10	2.0	0.35	6.0	0.9	0.2
3	10	2.0	0.35	6.0	0.8	0.3
4	10	2.0	0.35	6.0	0.7	0.4
5	10	2.0	0.35	6.0	0.6	0.5
6	10	2.0	0.35	6.0	0.5	0.6
7	10	2.0	0.35	6.0	0.4	0.7
8	10	2.0	0.35	6.0	0.3	0.8
9	10	2.0	0.35	6.0	0.2	0.9
10	10	2.0	0.35	6.0	0.1	1.0

Group B, above, is comprised of base Group A, with additions of silica fume and tin oxide added as a double line blend, in which the weight of one of those two materials additions decreases incrementally at a constant rate, while the weight of the other material addition increases incrementally at a constant rate.

In this Group all materials other than the two added, silica fume and tin oxide, remain constant in their weight ratios, g. The two additional materials, silica fume (See Appendix 8, 9) and tin oxid, SnO₂, respectively, see their weight ratios vary predictably, by either being increased (silica fume) or decreased (SnO₂) at the same constant 0.1g weight-increment.

Silica fume is a byproduct of the production of silicon metal or ferrosilicon alloys. Silicon metal and alloys are produced in electric furnaces in which the raw materials are quartz, coal, and woodchips. The smoke that results from furnace operation is collected and sold as silica fume.



Figure 4.3: Electronmicrograph of silica fume particles, x100

Perhaps the most important use of this material is as a mineral admixture in concrete,¹ with 95% of particle sizes typically $<1\mu\text{m}$, with particle density approximately $2.2\text{g}/\text{cm}^3$ and total surface area within the range $15\text{-}30\text{m}^2/\text{g}$. Silica fume was added in the form purchased, and not sieved or otherwise processed.

Tin oxide, SnO , a material that is widely used in the ceramics industry as an opacifier in glazes, is also used as a means by which a localized reducing atmosphere can be achieved within a powdered ceramic compact in an otherwise overall oxidising atmosphere. It was for this latter capacity that tin oxide was added to the list of constituent materials in Group C.

¹ Silica Fume Association, <http://www.silicafume.org/reprints.html>

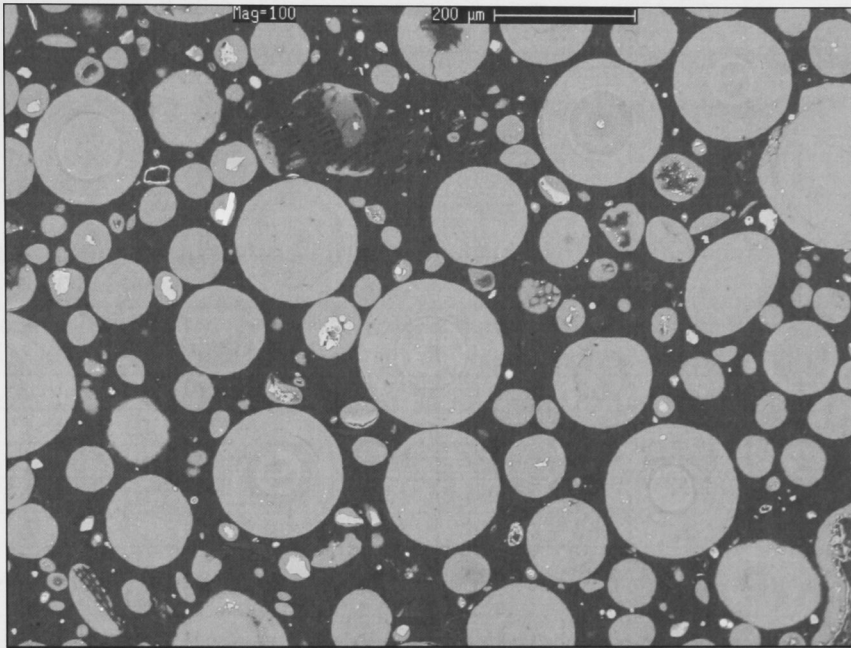


Figure 4.4: Electronmicrograph of 30µm polished thin section of silica fume, x100

With silica fume a source of not only silica and alumina but also FeO and CaO, it was hypothesized that additions of tin oxide might have a measurable influence on the rate and extent to which any structure formed by the constituent materials might sinter and melt. It was also hypothesized that this materials combination might allow the achievement of properties that could otherwise be achievable only at higher temperatures when fired in a standard oxidising atmosphere in the absence of tin oxide.

The purpose in the use of the double-line blend mechanism for the simultaneous addition and reduction of two materials is as follows:

1. the creation of ten, new sample combinations
2. the measurement and calculation of those samples' individual properties after sintering to each specified, successively higher temperature

3. the comparison of each of those samples' measured and calculated properties with each of the other sample's averages within Group B
4. the comparison of Group B individual-sample properties with those averaged Group A properties at each specified sintering temperature, °C

4.08.3 Group C

Table 4.7: Group C, weight of constituent materials, g

Sample No	SL500 g	Frit DA4194 g	Kaolin g	Water ml	Silica Fume g	Tin oxide g	Cobalt carbonate
1	10	2.0	0.35	6.0	1.0	0.1	0.07
2	10	2.0	0.35	6.0	0.9	0.2	0.07
3	10	2.0	0.35	6.0	0.8	0.3	0.07
4	10	2.0	0.35	6.0	0.7	0.4	0.07
5	10	2.0	0.35	6.0	0.6	0.5	0.07
6	10	2.0	0.35	6.0	0.5	0.6	0.07
7	10	2.0	0.35	6.0	0.4	0.7	0.07
8	10	2.0	0.35	6.0	0.3	0.8	0.07
9	10	2.0	0.35	6.0	0.2	0.9	0.07
10	10	2.0	0.35	6.0	0.1	1.0	0.07

Group C, is comprised by Group B, with the addition of cobalt carbonate at a constant weight, 0.07g, to each of its ten individual constituent samples. The reasoning informing the choice of materials constituting Group B is explained in 4.08.2.

Cobalt carbonate (**for particle-size details see Appendix 6**) was chosen for addition to the Group B series because of its capacity for volatility between 750-900°C and its potential to assist in the formation of eutectic mixtures that were modifications of mixtures that had formed and sintered previously in its absence.

The purpose in the use of cobalt carbonate as a single addition material is as follows:

1. the creation of ten, new sample combinations

2. the measurement and calculation of those samples' individual properties after sintering to each successively higher temperature
3. the comparison of each of those ten samples' averaged measured and calculated properties with each of the other sample's averages within Group B
4. the comparison of Group C individual-sample properties with those averaged Group A properties at each specified sintering temperature, °C

4.08.4 Group D

Table 4.8: Group D, weight of constituent materials, g

Sample Number	SL500 g	Frit DA4194 g	Kaolin g	Water ml	Silica Fume g
1	10	2.0	0.35	6.0	1.0
2	10	2.0	0.35	6.0	0.9
3	10	2.0	0.35	6.0	0.8
4	10	2.0	0.35	6.0	0.7
5	10	2.0	0.35	6.0	0.6
6	10	2.0	0.35	6.0	0.5
7	10	2.0	0.35	6.0	0.4
8	10	2.0	0.35	6.0	0.3
9	10	2.0	0.35	6.0	0.2
10	10	2.0	0.35	6.0	0.1

Group D, Table 4.8 above, is comprised by Group B, with the addition of silica fume to each of its ten individual constituent samples, with the weight, g, addition for each sample decreasing incrementally by 0.1g.

The purpose in the use of this single addition material is as follows:

1. the creation of ten, new sample combinations
2. the measurement and calculation of those samples' individual properties after sintering to each successively higher temperature
3. the comparison of each of those samples' measured and calculated properties with each of the other sample's averages within Group B

4. the comparison of Group C individual-sample properties with those averaged Group A, B and C properties at each specified sintering temperature, °C

4.09 Determination of sample form

All sintered samples are to be measured for their compressive strength and a cylindrical form was chosen as appropriate for the characterisation of the sintered structures' properties, particularly also as it applied to measurement and firing in ANSTO's Laser Dilatometer Furnace.

4.09.1 Choice of the dimensions of the cylindrical form

Paper cylinders of diameter 32mm and length 60mm were made, batches of raw materials combinations weighing 10g, 15g and 20g were prepared, each batch was placed in a paper cylindrical form, each was compacted and their dry volumes measured.

A sample containing 10g of the primary raw material, with dimensions length 30mm, diameter 32mm, and average unsintered volume 25cm^3 when compacted, was chosen as standard for the production of uniform samples for sintering and the subsequent characterisation of their properties.

4.09.2 Choice of material for cylindrical container form

Paper was chosen as the cylindrical-former material in the knowledge that it would burn off at low temperature, $\sim 250\text{-}300^\circ\text{C}$, in the initial stages of the sintering cycle, leaving its sintered contents available for handling and measurement in a visually and manually accessible form.

It was decided to leave the samples within their cylindrical paper formers as removal of the paper from dried samples made samples fragile, with particles sticking to the paper surface and creating problems in their safe transport from Canberra to the ANSTO facility on the outskirts of Sydney.

The paper's negligible ash residue on combustion would not contaminate the cylinder's contents or its surfaces and hence could be disregarded as a possible variable to be included in the multiple factors contributing to sintered properties.

Visual observation of combustion trials of sample cylinders showed the paper former initially blackening, smoldering and buckling, eventually catching fire with its burning fragments curling away from the contained ceramic material and falling on to the kiln shelf on which the samples sat. Elapsed time from first charring of the paper former to complete removal by combustion averaged five minutes, a period in which it was not possible for the local temperatures reached by the burning paper to have affected the course of subsequent sintering of the powdered ceramic fractions contained within it.

Samples removed from the furnace after combustion of the paper cylinders did not show any observable alteration to the otherwise unsintered ceramic structures.

Post-firing comparison of unsintered and sintered ceramic samples after firing to 1000°C showed no optical or microscopic evidence of blocking, uncharacteristic alteration to or constriction of voids on cylinder surfaces, or the presence of any fraction not

characteristic of the interior surfaces of the porous ceramic's void fraction. With $>700^{\circ}\text{C}$ the firing end point for all samples, any carbon residue of the paper former that might have still existed at 300°C can be assumed to be completely removed in the oxidising atmosphere of the firing by the time samples had reached 700°C . The sellotape used to seal and strengthen the cylindrical paper form left no observable residue on completion of the sintering cycle.

4.09.3 Fabrication of cylindrical paper container form

Multiple paper cylinders were prepared. Standard filter paper², was used to make a triple-layer thickness cylinder form with a closed base, diameter 32mm, length 40mm, by rolling cut strips of 40mm width filter paper around a 32mm diameter, stainless steel mandrel, where each cylinder wall and base was comprised by three layers of paper, with all seams sealed by clear adhesive sellotape, with the finished cylinder further strengthened by wrapping with overlapping layers of clear adhesive tape.

4.10 Identification of samples

Each materials combination was given a label as detailed in Appendix 10

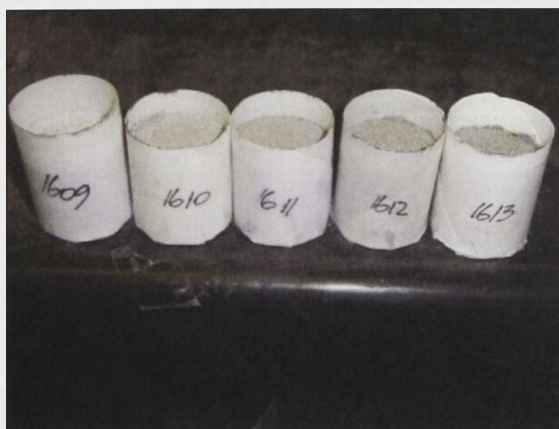


Figure 4.5: Unsintered, dried samples showing numbering sequence

² Whatman Filter Papers #1, 24.0cm, Circular #1001 240

4.11 Mixing of dry materials for sintering

Where two or more materials were to be combined, the standard 10g cenosphere sample was first placed in a glass beaker and the first of the other dry material was added and mixed by stirring with a stainless steel spatula until observation suggested that each was well mixed with the other. Each additional material was then added to the existing mix with each mixed thoroughly before the next addition. After all dry materials were mixed water was added as required by using a single-measure burette and immediately mixed thoroughly into the combined dry-mixed sample material.

4.11.1 Compaction of samples in paper cylindrical former

The wet-mixed material composite is transferred to a standard paper cylinder and compacted using a cylindrical wooden compacting rod, the diameter of which is 0.05mm smaller than the diameter of the paper cylinder. When compacted the sample is then transferred to a bench drill press where it is further compressed by a turned stainless steel platen to ensure that the planes of the top and bottom faces of the cylindrical form are parallel with each other and at 90° to the cylinder's longitudinal axis.

Mixed samples were then dried, first uncovered in air for 24 hours and then for 48 hours in an electric drying oven at 80°C.

4.11.2 Identification of samples after removal from the firing chamber

After firing, furnace shelves were removed and sintered samples were then individually removed in the reverse order to that in which they had been packed. the sample's identifying number was then written on the top and side of each sample and placed into a

numbered cliplock bag that had each been marked with the same number. Samples were then further sorted into their sequence groups and bagged in larger cliplock bags that identified a) date, b) maximum firing temperature °C, c) series numbers, d) Group letter as appropriate, e) place of firing.

4.12 Choice of firing maximum sintering temperatures

The furnace used in the sintering of all samples in this study was a Laser Dilatometer Furnace sited in the Materials Division, Australian Nuclear Science and Technology Organisation, ANSTO, Lucas Heights, New South Wales. This furnace is computer driven and infinitely variable in its programmable firing cycle/sequences limits, with a maximum available firing temperature of 1550°C. (See Appendix 11).

Successive firings were then conducted at 100°C intervals between 1100°C and 1400°C, with the interval 1400°C to 1500°C then varied to include a 50°C increase to 1450°C, with the period of time at which the contents were soaked or held at maximum temperature remaining constant in all firings.

4.13 Design of firing cycle

If a residually damp dense clay-based ceramic were heated at a temperature-increase rate which sees the rapid achievement of 100°C, the residual water within its structure will boil and form steam. If the rate at which that residual water vaporizes and forms steam exceeds the rate at which that steam can be vented safely to the outside via its void

fraction, the risk of damage to the ceramic's structure from an explosive release of steam pressure is almost inevitable.

The highly porous nature of the unsintered, mixed cenosphere structure, its uniformly high proportion of large spherical particles and the regularity of its articulated void fraction, meant that this ceramic structure was not subject to those explosive dangers. This permitted both the design of a firing cycle that would allow a more rapid heating rate than would otherwise have been possible if conventional clay-based fine-particle ceramic materials and firing cycles had been in use as well as the use of longer, slower firing cycles if desired.

Preliminary test firing of samples in the ANSTO Laser Dilatometer furnace, Figure 4.6, showed observable exfoliation of fine surface particles at approximately 460°C. The firing cycle common to all firings, including the latter three, was adjusted to accommodate this phenomenon by reducing the average temperature rate °C increase between 300-800°C to 60°C/hr from the 160°C/hr employed between switch-on/ambient and 300°C.

4.14 Sintering of samples

Computer control of the firing of ANSTO's Laser Dilatometer Furnace, the repeated use of both the same shelves and the same number of pieces of kiln furniture and the packing of the same number and approximately the same total volume of samples produced a total ceramic mass that was replicated almost exactly in each firing. While the density of the

total ceramic mass in each firing did vary, it varied predictably such that the distribution of the various density ranges within the furnace was constant. Having established the initial firing cycle that was then replicated across the series, we saw it as unnecessary to depend upon pyrometric cones for the determination of the firing end point. (For detail of firing cycles see Appendix 12, 13).

Samples were packed on thin sheets of high-alumina ceramic sheeting, which had been dusted with fine zirconium particles, with each material acting as complimentary refractory layers between the shelf and samples. The packed chamber with its shelves and furniture in place was photographed before each firing.



Figure 4.6: Group A, pre-firing in ANSTO Laser dilatometer furnace, 1300°C, showing silicon carbide shelving and high alumina sheeting

After passing through the successive replicated ramps the chamber achieved its programmed maximum temperature, was then soaked for a specified time to allow the achievement of optimally even temperature distribution within samples and was then fired down at 2.6°C/min until 400°C, at which point the furnace switched off automatically and then cooled at the rate natural to its insulation and construction.

4.15 Recording of data.

- Each sintered sample was measured using electronic Vernier calipers with sample length and diameter each measured at four points, recorded and averaged.
- All sample dimensions were recorded at the time of mixing
- All sample wet-mixed weights were recorded at the time of mixing.
- Sample dry, fired weight was recorded immediately after removal from the kiln's chamber, identified and bagged.

4.16 Measurement of permeability rates post firing

Each sample was subjected to flow-rate measurement testing after weighing to determine dry-weight post firing. Samples were encased in two layers of adhesive, grey gaffer tape, so that only the top and bottom cylinder faces were open to the passage of water. The enclosed sample was then placed at the base of a hollow, turned stainless-steel cylinder, with the junction of the sample and the cylinder then further sealed by two layers of the same adhesive, grey gaffer tape. The stainless steel cylinder was itself permanently

attached to the base of a funnel, so producing a head of water of length 25cm and diameter 30mm.

The funnel was attached to a standard laboratory retort stand and was filled with tap water, water was allowed to pass through the sample, the initial collection was discarded and water was then collected for a further two minutes.

Water loss from the funnel reserve was replaced at a rate equal to its loss during flow measurement so that head height and volume remained constant.

Each sample's flow rate was measured five times with results recorded and averaged.

4.17 Measurement of compressive strength

The measurement of sample compressive strength was chosen for the determination of the properties of mechanical failure and modulus of elasticity for the reason that the highly porous nature of the sintered structures presented an insurmountable problem in the concentration of stress at the grip location on the sample if subject to tensile axial loading.

All sintered samples were tested for compressive strength using an Instron model 4505 Universal Testing System with 100kN load cell.

The top and bottom faces of each dry sample were lightly ground using P800 grade emery paper to remove any protuberant irregularities and to achieve an approximately even horizontal plane for each surface. Each ground surface was then cleaned with

compressed air before testing. Each cylindrical sample was placed on the Instron 4504 moveable crossbeam with its marked top surface uppermost.

The same steel compression platen was used on the upper surface of each sample in each test. The identifying number of each sample was recorded with each result. All recoverable remains were collected, bagged, labeled and reserved for subsequent examination.

4.18 Imaging and analysis of samples using SEM

4.18.1 Preparation of sample thin sections for SEM

Samples requiring imaging of polished sections and analysis using SEM were prepared as 30 μ m polished thin sections in the Thin-section Laboratory, Department of Earth & Marine Sciences, Australian National University. Each sample was prepared in the following sequence:

1. The section for preparation was cut using a water cooled, diamond saw with moveable armature and static blade to a thickness of approximately 1.2mm.
2. The sample cut face was hand ground using P800 wet and dry papers to minimize irregularities within the cut surface.
3. The sample was dried on a hot plate and when cooled was attached to a standard petrology slide using Petropoxy that had first been applied and absorbed and absorbed into the porous structure of the sample before slide attachment.

4. The sample number was inscribed into the lower face of the slide using a diamond-tipped scriber.
5. Using 15 μm standard alumina oxide grit each sample was then reduced to 35 μm average thickness on the laboratory's Logitech LP30 production lapping and optical polishing equipment.
6. The sample was then polished and further reduced in thickness using 2.5 μm paste and oil, with the final polished 30 μm section finished on Pellon cloth with 1 μm diamond paste and oil.

4.18.2 SEM imaging of sample thin sections and fracture faces

The facilities of the University's Electron Microscopy Unit, (EMU), were then used in the further preparation of polished thin sections for imaging and analysis. Depending upon the intention, samples were mounted on appropriate stubs, which were marked on their upper and lower faces with their sample numbers, and then either sputter coated with gold, for imaging using the Cambridge 360 instrument, or carbon-sputter coated for X-ray analysis using the Jeol 6400. Electronic records of both images and analyses obtained from polished thin-section samples were individually identified with their appropriate sample number and retained, with each image showing sample number, magnification and scale bar. Samples were observed at x80, x250, x800 and x2500 as appropriate and recorded and saved electronically.

Large remnant fracture samples were attached to mounting stubs using nail polish, which when hardened was then gold sputter-coated for observation on the Cambridge 360

instrument. Samples were observed at appropriate magnifications and images recorded and saved electronically with each image showing sample number, magnification and scale bar.

4.19 Preparation of core samples for tomographic imaging

Cores were cut from the central longitudinal axis of selected, full-size, sintered cylindrical samples in the Mineral Separation Laboratory, RSES, Australian National University, using a 2mm water-cooled, hollow-core drill and were then washed and dried. Samples were marked with their sample number and placed in appropriately numbered clip-lock bags. Each sample was dried for 24 hours in a drying oven in the Materials Laboratory, Department of Engineering, before being taken to the Tomography Unit, Department of Applied Mathematics, RSPHysSE, Australian National University.

Tomographic analysis of cores was performed by Dr Tim Senden, with data retained and translation of data into three dimensional images performed by Dr Adrian Sheppard.

4.20 Vacuum infiltration of sintered samples by polymerics

4.20.1 Vacuum infiltration

Fourteen hollow plastic cylindrical forms were turned, where finished cylinder length was 40mm, inner diameter 34mm and wall thickness 4mm. Each hollow cylindrical form included a removable, fitted base plug turned from the same material that when removed allowed the extraction of the hardened but uncured, infiltrated polymer plug, within which was contained an infiltrated sintered sample. The surfaces of the mould forms were

Chapter 4 Experimental Methods & Techniques

cleaned inside and out with acetone and dried. The interior walls of the containers and their base plugs that were to be in contact with polymer were coated twice with mould release and allowed to dry for ten minutes. Base plugs were inserted into the cylinder base. An adhesive label showing the identifying test number of the sample to be infiltrated was placed on the outside of the cylinder wall.

The polymeric for infiltration were mixed in accordance with manufacturer's directions in a mortar and pestle and poured into a container. The container was identified by marking with the appropriate sample number.

Minerals and other materials mixed with the polymer included:

Table 4.9: Materials used in the compounding of materials for vacuum infiltration

Sb_2O_3	Antimony oxide	MnO_2	Manganese dioxide
$BaSO_4$	Barium sulphate	NiO	Nickel oxide
Al_2O_3	Calcined alumina		Polymers
$CaCO_3$	Calcium carbonate	$K_2O.Al_2O_3.6SiO_2$	Potassium feldspar
PbO	Canary yellow litharge	SiO_2	Silica quartz
Cr_2O_3	Chromium oxide	Fe_2O_3	Red iron oxide
$CoCO_3$	Cobalt carbonate	Pb_3O_4	Red lead
$CuCO_3$	Copper carbonate		Silica fume
CuO	Copper oxide	SnO_2	Tin oxide
$NaCl$	Domestic common salt	TiO_2	Titanium dioxide

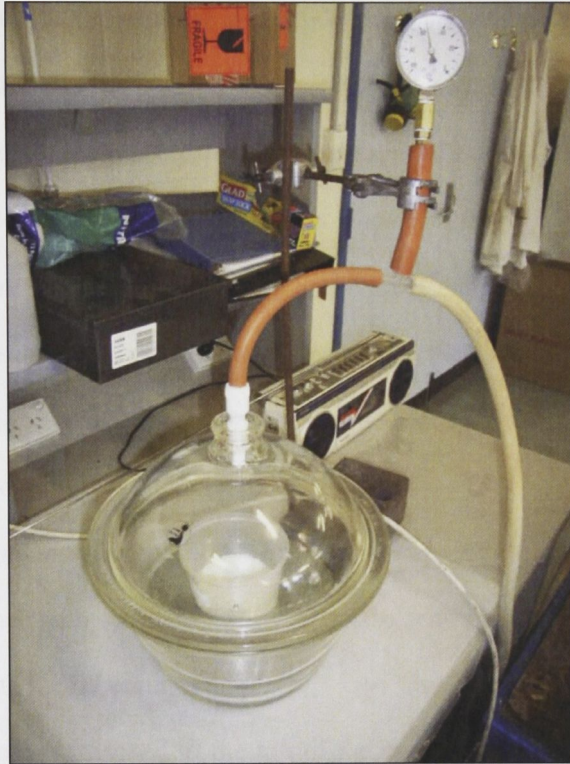


Figure 4.7: Desiccator chamber containing sample for de-airing, with vacuum pump attached

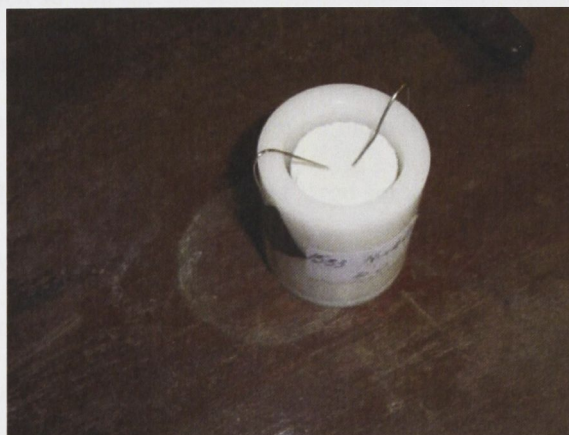


Figure 4.8: Sintered sample in container prior to vacuum infiltration

4.20.2 Summary of mixing sequence and infiltration under vacuum of polymeric

1. A standard sample that had been previously sintered to 1100°C is placed in a cylindrical receptacle with a removable base plug, the interior of which had been cleaned and coated with mould release.
2. Two cut-wire holding pins, Figure 4.8, are attached to the cylinder's outer wall and secured against the upper surface of the cylindrical sample to prevent it floating when the polymer compound for infiltration is poured around and over it
3. The containment cylinder is identified with the appropriate sample number
4. The container with its mixed polymeric is placed in a lidded desiccator chamber with the lid securely in place
5. A rubber hose is attached to the top of the evacuation outlet and then to the inlet point on the vacuum pump, the vacuum pump is switched on
6. Pressure within the desiccator is reduced to -70kPa and the outlet/inlet valve is closed so that the vacuum is maintained. The pump is switched off and the sample observed for out gassing
7. When bubbles have stopped forming on the polymer's upper surface from within the fluid polymer volume and large surface bubbles have burst, the outlet/inlet valve is opened and internal pressure is returned to ambient.
8. This sequence of pressure reduction, valve closure, out gassing and restitution of ambient external pressure within the desiccator is repeated three times.

9. The de-aired sample is removed from the desiccator and the unused fluid polymer is poured over and around the sample secured by wire holding pins within its cylindrical container.
10. The polymer is absorbed into the void fraction of the sintered sample and the cylinder is topped up from the de-aired bulk source until such times as no more polymer is absorbed and its fluid level is 3-4mm below the upper level of the cylinder
11. The cylinder + sample + polymer is placed into the desiccator, its lid is replaced and well seated and the vacuum pump is switched on. Large bubbles are observed coming to the surface of the polymer from the sides of the sample.
12. When the gauge shows internal pressure as -70kPa the outlet/inlet valve is closed and the chamber and its contents held for one minute. The inlet/outlet valve is opened and pressure within the desiccator is allowed to return to ambient, in the process of which polymer is forced into the articulated void fraction of the sample and the polymer level is seen to drop significantly
13. The lid is removed and the polymer level within the cylinder container is again topped up to a point 3-4mm below the level of the top of the container cylinder
14. The sequence 11-13 is repeated until a) no bubbles are observed as out gassing from the contained porous sample and b) the level of the polymer

- reservoir within the cylinder does not drop after pressure is returned to ambient
15. The vacuum pump is switched off, internal pressure is returned to ambient, the desiccator lid is removed; the infiltrated sample is removed and placed to one side to cure. The residual unused polymer in its labeled container is placed next to the labeled infiltrated sample for cure.
 16. The cured, hard sample is removed from its containment cylinder and immediately labeled appropriately.
 17. Hard infiltrated samples are placed in a temperature-controlled oven and heated to 90°C for 4 hours for final cure and achievement of maximum hardness, or, in the case of infiltrated polymers that do not require heating for final cure, allowed to stand for the period of time specified as necessary for final cure.

4.20.3 Summary of mixing sequence and infiltration of polymer-minerals and other compounds under vacuum

1. The polymeric for infiltration is mixed in accordance with manufacturer's directions in a mortar and pestle, an appropriate volume of acetone is added at this point to reduce the sample's viscosity and mixed thoroughly. The chosen mineral is added to the polymer/acetone mix and thoroughly mixed. The mixed polymer/acetone/mineral compound poured into a container. The container is identified by marking with the appropriate sample number.

2. When bubbles have stopped forming on the polymer's upper surface from within the fluid polymer volume and large aggregated surface bubbles have burst, the outlet/inlet valve is opened and internal pressure is returned to ambient.
3. The sequence shown in Section 4.20.2 is repeated until a) no bubbles are observed as out gassing from the contained porous sample and b) the level of the polymer reservoir within the cylinder does not drop after pressure is returned to ambient.



Figure 4.9: Cylinders of hardened polymer/mineral composite, each containing an infiltrated sintered sample

4.20.4 Choice of polymer for infiltration

Derakane 411-3350 Epoxy Vinyl Ester Resin[®] was selected for use as the polymer to be infiltrated under vacuum into the structure's void fraction. Its properties are summarized as follows:

Table 4.10: Properties of Derakane 411-3350 Epoxy Vinyl Ester Resin[®]

Property	Value
Density, 25°C/77°F	1.046g/mL
Dynamic Viscosity, 25°C/77°F	370mPa-s
Kinematic Viscosity	350 cSt
Styrene Content	45%
Shelf Life, Dark, 25°C/77°F	7 months

The properties that might be desirable in a successfully infiltrated structure were unknown, and the benefits ascribed to Derakane 411-3350 by its manufacturer, see Appendix 14, made it an attractive choice for investigation:

- Resistance to a wide range of acids, alkalis, bleaches and solvents
- Tolerates heavy design loads without causing failure due to resin damage
- Superior elongation and toughness provides FRP equipment with better impact resistance and less cracking due to cyclic temperature, pressure fluctuations and mechanical shocks
- Gel times could be manipulated to produce a range of working times.

4.20.5 Curing of samples infiltrated with a polymer

After removal from their formers, hardened sample were placed in either a small electric furnace, shown in Fig 4.10, or an autoclave, Fig. 4.11, and heated to 90°C and held for four hours in accord with the manufacturer's recommendations.



Figure 4.10: Small furnace used to cure infiltrated samples, Materials Laboratory, Department of Engineering



Figure 4.11: Autoclave used to cure infiltrated samples, Materials Laboratory, Department of Engineering

4.20.6 Preparation of cured, infiltrated samples for compression testing

Cured samples were turned on a lathe to a diameter appropriate to expose the outer layer of ceramic within the polymer matrix, approximately 28mm, length 27mm.

4.20.7 Measurement of cured, infiltrated sample compressive strength

All sintered samples were tested for compressive strength using an Instron model 4505 Universal Testing System with 100kN load cell.

The same preparation procedure was used as was previously described in Section 4.20.2.

4.20.8 Preparation of samples for X-ray analysis

All samples intended for X-ray analysis using the Joel 6400 SEM, Electron Microscopy Unit, ANU, were turned to 25mm diameter, sawn to 10mm length using an electric

water-cooled diamond saw. Top and bottom faces were further polished using P800 wet and dry paper with water and dried.

4.20.9 X-Ray analysis of samples

Data from five analyses of each sample were collected using the Joel 6400 instrument and averaged. Calculation of percentage ratios of elements present in each sample was performed by Dr Frank Brink, EMU, RSBS, ANU.

4.20.10 Measurement of attenuation of signal

Experiments confirming the hypothesis that the sintered Group A structure could be infiltrated with a polymer/mineral composite were performed at the Photon Factory Beamline, Tsukuba, Japan, by Dr Mark Ridgway, RSPHysSE, ANU, after preparation by the author in the Electronic Materials Engineering Laboratory, RSPHysSE. Samples for testing were cleaned and sawn to within the thickness range 50-60 μm .

4.20.11 Tomographic imaging of sintered sample

Cores for tomographic imaging were prepared in the mineral separation laboratory, RSES, ANU. Cores were cut with water-cooled, 5mm internal diameter diamond drill, dried and held at 100°C overnight in a drying oven. On removal cores were identified and immediately bagged.

Chapter 5

Results

5.1 Estimation of errors

In this work there are four properties of the materials that we have measured and which are of primary significance to the definition of their functionality, these are

- a) Density
- b) Permeability
- c) Strength
- d) Modulus

We begin by deriving the possible errors in these quantities from the measurements that were carried out.

a) Density:

$$\rho = \frac{m}{V} \quad error[\rho] = \frac{\Delta m}{m} + 3 \frac{\Delta l}{l}$$

b) Permeability:

$$P = \frac{W.l}{A.t} \quad error[P] = \frac{\Delta W}{W} + \frac{\Delta l}{l} + 2 \frac{\Delta d}{d} + \frac{\Delta t}{t}$$

c) Strength:

$$\sigma = \frac{F}{A} \quad error[\sigma] = \frac{\Delta F}{F} + 2 \frac{\Delta d}{d}$$

d) Modulus

$$E = \frac{Fl}{A\Delta l} \quad error[E] = \frac{\Delta F}{F} + 2 \frac{\Delta d}{d} + \frac{\Delta l}{l} + \frac{\Delta(\Delta l)}{\Delta l}$$

5.1.1 Measurement of dimensions

Sample dimensions were measured with standard workshop instruments capable of accuracy to 0.01mm.

The expected relative error for sample length = $0.01/30 \approx \pm 3 \times 10^{-4}$

The expected relative error for sample diameter = $0.01/32 \approx \pm 3 \times 10^{-4}$

5.1.2 Measurement of weight

Typical sample weight = 13g. Sample weight was determined using laboratory scales with resolution of 0.0001g

The expected relative error for weight = $0.0001/13 \approx \pm 8 \times 10^{-6}$

5.1.3 Measurement of mechanical properties

Measurement of mechanical properties has been carried out on a calibrated Instron Testing Machine, which has the following specifications:

Load cell accuracy = 0.01% (10^{-4})

Displacement resolution = 0.01mm

The stiffness of the load frame, the load cell and the compression platens is estimated to be 10^6 N/mm. This contributes approximately 2% to the calculated value of the modulus.

Therefore the expected error for stress is estimated to be less than 10^{-3} and **the expected error for elastic modulus is estimated to be of the order of 10^{-2} .**

5.1.4 Measurement of particle size

Particle size determination was carried out by sedimentation in a fluid medium. The exact error has not been determined and it has been confirmed that the calibration of the instrument has been routinely carried out by the technical staff of Particle Surface Sciences Pty Ltd. It is assumed that maximum error in particle-size determination does not exceed $\pm 5\%$.

5.1.5 Sintering temperature

Sintering of samples was carried out in a Laser Dilatometer Furnace. Calibration of the furnace's controls was routinely performed by the appropriate staff of the Materials Division, Australian Nuclear Science & Technology Organisation.

The maximum error for temperature in sintering does not exceed $\pm 1\%$.

5.1.6 Calculation of density

The expected relative error for density = $1.5 \times 10^{-3} \text{g/cm}^3$

These predicted errors are of the order of less than 1%, however, it appears that the relative error is typically larger than the predicted error and on the basis of our previous experience we assign an error of 5% to the primary properties of density, permeability, strength and modulus.

5.2 Results

5.2.1 Density

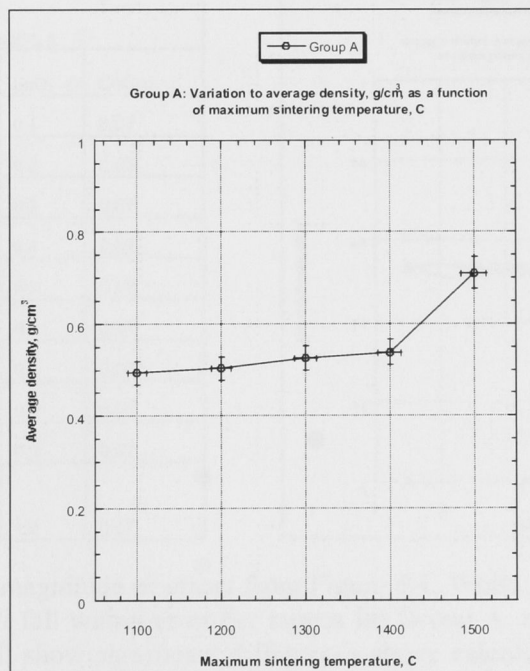


Figure 5.1: Group A, small increase in density is seen between 1100°C and 1400°C , with a significantly greater increase seen after 1400°C . Each point represents an average of five measurements, with error bars assigned according to calculations shown in Chapter 5.

Legend Figure 5.2
Group B samples
Constituent materials, g

Sample No	Silica fume	SnO ₂
1	1.0	0.1
2	0.9	0.2
3	0.8	0.3
4	0.7	0.4
5	0.6	0.5
6	0.5	0.6
7	0.4	0.7
8	0.3	0.8
9	0.2	0.9
10	0.1	1.0

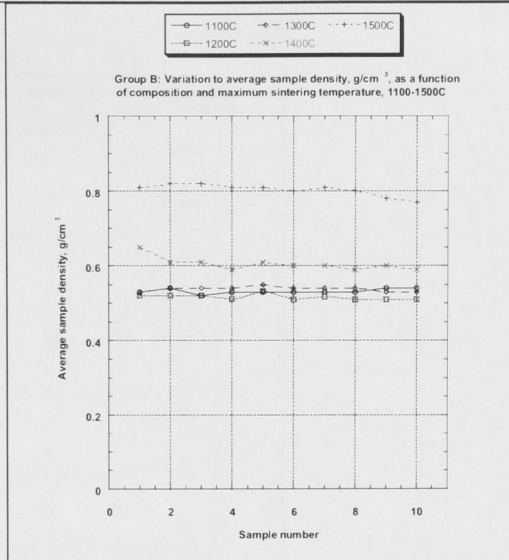


Figure 5.2: Group B, note the magnitude of errors from Figure 5.1, results for 1100°C, 1200°C and 1300°C all fall within error bars for Group A, however results for 1400°C and 1500C all show significant differences above calculated errors. Each point represents an average of five measurements, with error bars assigned according to calculations shown in Chapter 5. Variation to constituent-materials ratios is seen only in additions of silica fume and SnO₂, where all other materials do not vary.

Legend Figure 5.3
Group C samples
Constituent materials by weight, g

Sample No	Silica fume	SnO ₂	CoCo ₃
1	1.0	0.1	0.07
2	0.9	0.2	0.07
3	0.8	0.3	0.07
4	0.7	0.4	0.07
5	0.6	0.5	0.07
6	0.5	0.6	0.07
7	0.4	0.7	0.07
8	0.3	0.8	0.07
9	0.2	0.9	0.07
10	0.1	1.0	0.07

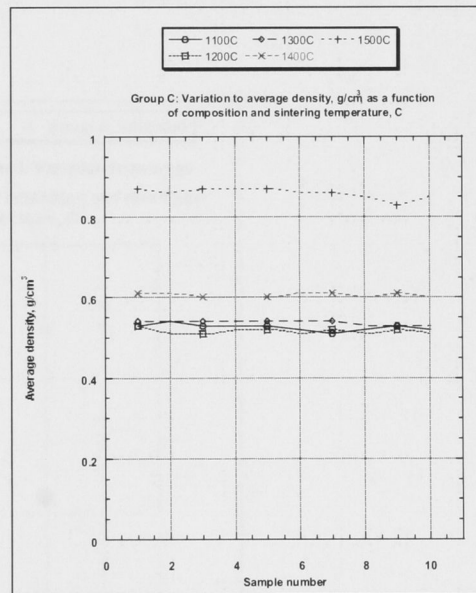


Figure 5.3: Note the magnitude of errors from Figure 5.1. While results for 1100°C, 1200°C and 1300C all fall within error-bar ranges for Group A, results for Group C 1400°C and 1500C all show significant differences above calculated errors for both Group A and Group B. Each point represents an average of five measurements. Note that variation to constituent-materials ratios is seen only in additions of silica fume, SnO₂ and CoCo₃, where all other materials do not vary.

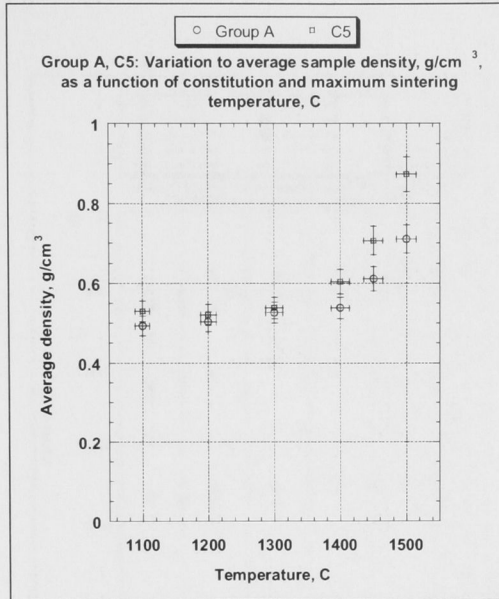


Figure 5.4 compares results for variation to average density for Group A and C5 and illustrates the potential for Group A properties to be amended by the addition of materials, where results for 1100°C show C5 approximating average density for Group A as at 1400°C. Each point represents an average of five measurements, with error bars assigned according to calculations shown in Chapter 5.

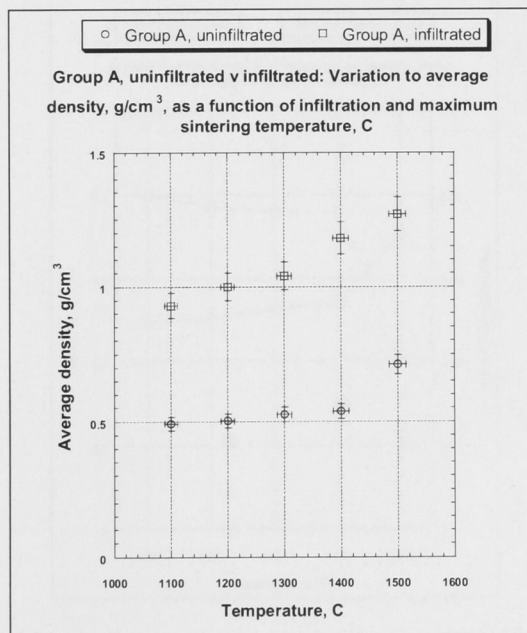


Figure 5.5 shows significant variation to average density for Group A structures before and after their infiltration by a polymer and its subsequent curing.

5.2.2 Permeability

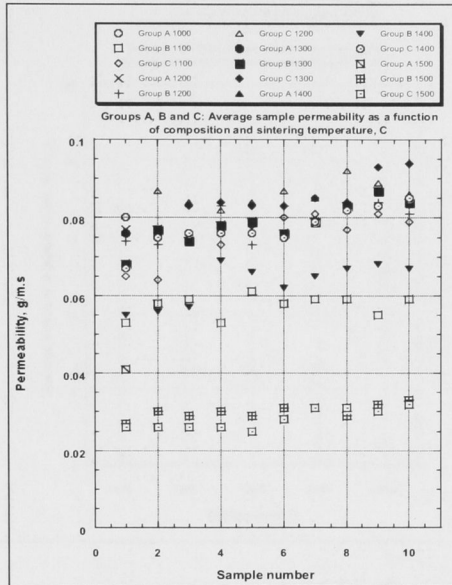


Figure 5.6 shows the distribution of averaged values for permeability in each materials Group and series after their sintering at each of the maximum temperatures specified in Table 1.0, 1100-1500°C. Note that no value, P, is recorded as lower than 0.02, indicating the existence of an open, articulated-void fraction in all sintered samples at each temperature. Each point represents an average of five measurements.

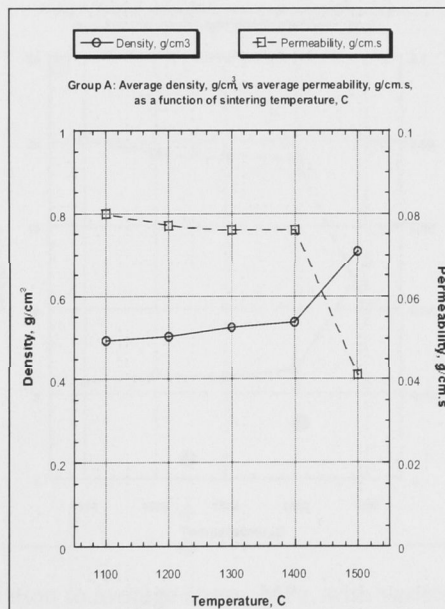


Figure 5.7 compares variation to average density, g/cm^3 , with variation to average permeability, g/cm.s , as a function to maximum sintering temperature, °C. Note that between 1100-1400°C decrease to permeability reflects increase to average density, with an unexpected reduction at 1400°C and a disproportionate increase over that of density between 1400°C and 1500°C.

5.2.3 Strength

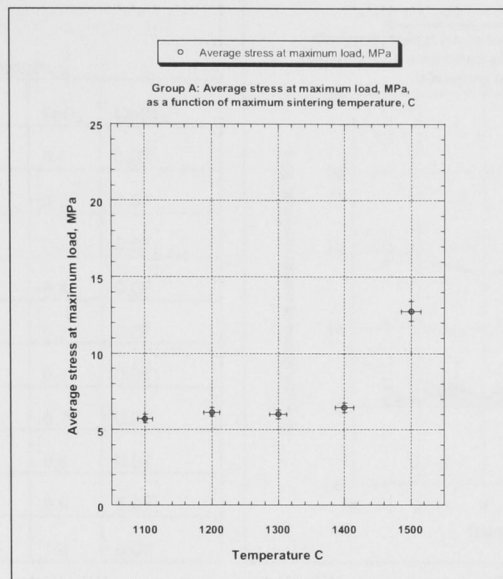


Figure 5.8 shows increase to stress at maximum load for Group A, where each point is an average of five measurements, with error bars assigned as outlined at the beginning of Chapter 5. Increase between 1300°C and 1400°C is marginal and increases significantly between 1400°C and 1500°C. Each point is an average of five measurements.

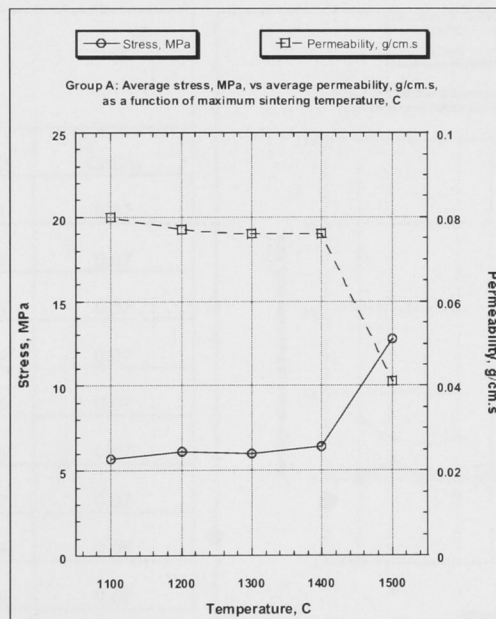


Figure 5.9 compares variation to average stress, MPa, with variation to permeability, g/cm.s, as a function of maximum sintering temperature, °C. Decrease to permeability across the range 1100-1400°C is marginal, and with the exception of a slightly greater increase seen at 1200°C approximates the decrease in permeability seen over the same range. At 1500°C maximum stress has doubled where permeability has halved over values for 1400°C.

Legend Figure 5.10
Group C samples
Constituent materials by weight, g

Sample No	Silica fume	SnO ₂	CoCo ₃
1	1.0	0.1	0.07
2	0.9	0.2	0.07
3	0.8	0.3	0.07
4	0.7	0.4	0.07
5	0.6	0.5	0.07
6	0.5	0.6	0.07
7	0.4	0.7	0.07
8	0.3	0.8	0.07
9	0.2	0.9	0.07
10	0.1	1.0	0.07

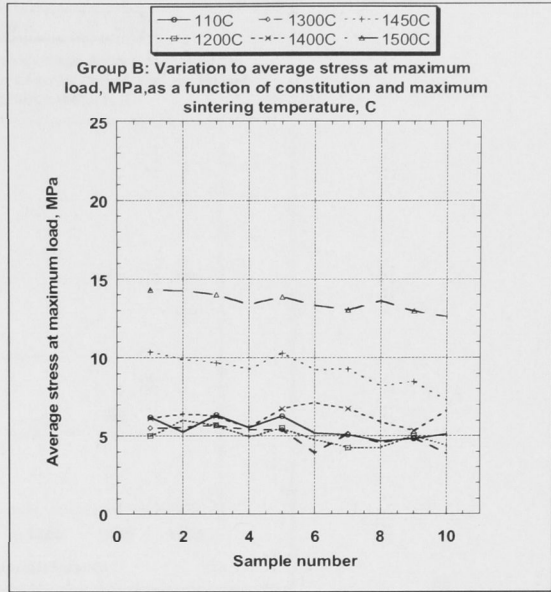


Figure 5.10 shows increase to stress at maximum load for Group B, where each point is an average of five measurements, with error bars assigned as outlined at the beginning of Chapter 5. Variation to constituent-materials ratios is seen only in additions of silica fume and SnO₂, where all other materials do not vary.

Legend Figure 5.11
Group C samples
Constituent materials, g

Sample No	Silica fume	SnO ₂	CoCo ₃
1	1.0	0.1	0.07
2	0.9	0.2	0.07
3	0.8	0.3	0.07
4	0.7	0.4	0.07
5	0.6	0.5	0.07
6	0.5	0.6	0.07
7	0.4	0.7	0.07
8	0.3	0.8	0.07
9	0.2	0.9	0.07
10	0.1	1.0	0.07

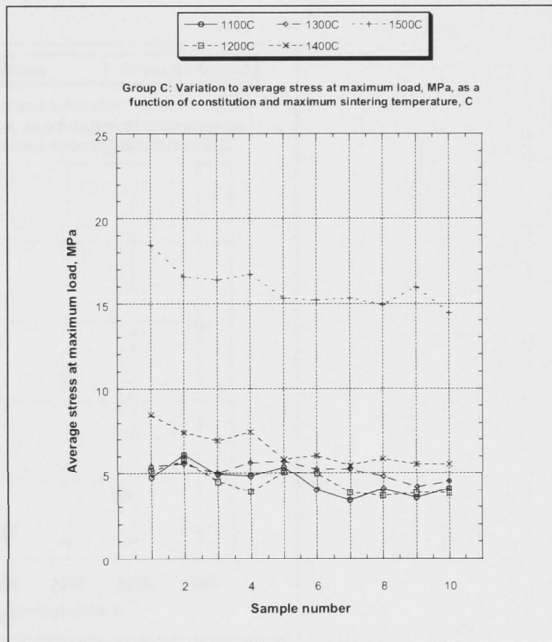


Figure 5.11: Note differences to increase in average stress at maximum load, MPa, to Group C samples when compared with results for Group B, Figure 5.10, for the temperature range 1300-1500°C. Each point is an average of five measurements. Variation to constituent-materials ratios is seen only in additions of silica fume, SnO₂ and CoCo₃ where all other materials are constant.

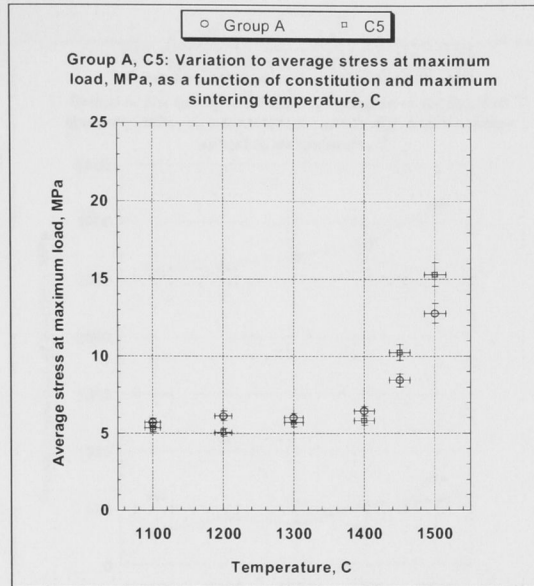


Figure 5.12 compares average stress at maximum load, MPa, for Group A and C5 samples, with divergence of values at 1200°C and then with significant increase to C5 between 1400°C and 1500°C. Each point is an average of five measurements, with error bars assigned as outlined in Chapter 5.

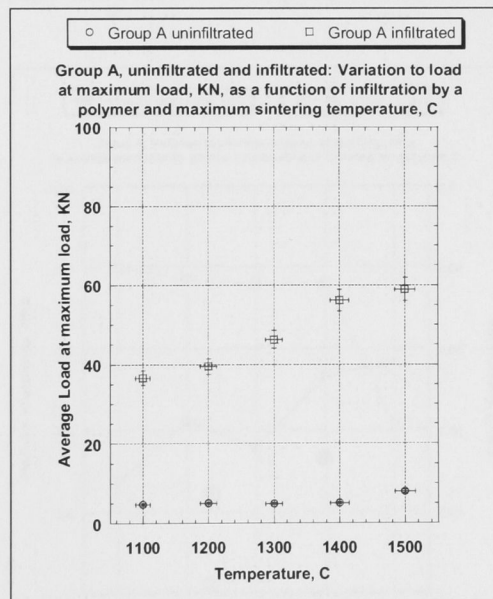


Figure 5.13 compares variation to average load at maximum load, kN, for Group A samples when uninfiltred and infiltred with a polymer and subsequently cured. Where uninfiltred variation is insignificant until 1400°C, increase for infiltred samples across the range 1100-1500°C is constant with increase for 1500°C double that of 1100°C. Increase at 1500°C for infiltred samples is almost five times that of the increase seen for uninfiltred samples. Each point is an average of five measurements, with error bars assigned as outlined in Chapter 5.

5.2.4 Modulus

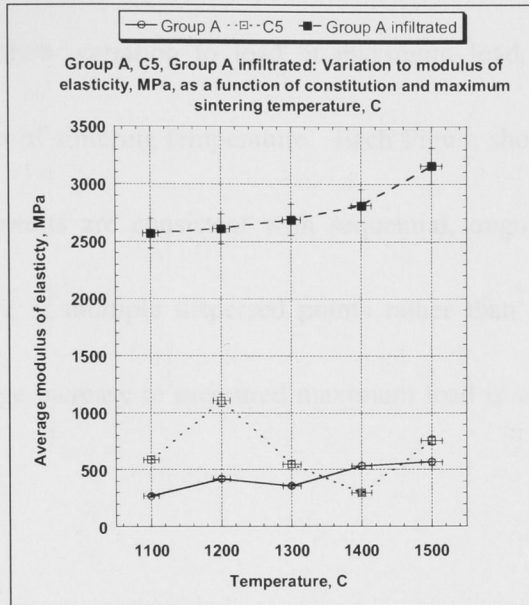


Figure 5.14 compares variation to modulus of elasticity, MPa, for Group A, C5, and Group A infiltrated with a polymer and cured. Differences between Group A and C5 are attributed to variation to C5 constituents, where those of Group A are constant.

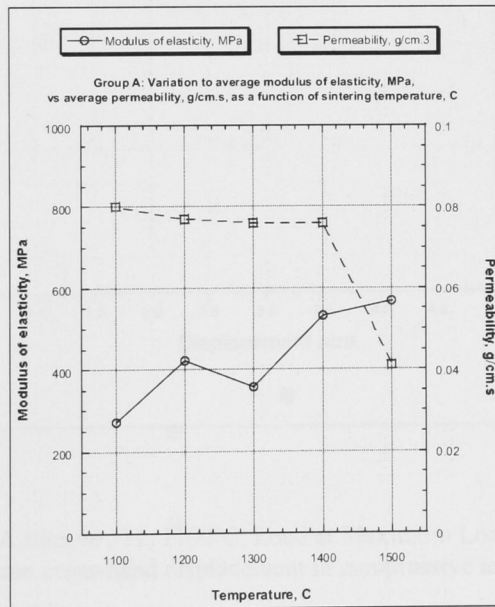


Figure 5.15 compares variation to modulus of elasticity, MPa, with permeability, g/cm.s, for Group A samples.

5.2.5 Mechanical behaviour under compression

Figures 5.16-5.20 show variation to load at maximum load, during compression testing as a function of sintering temperature. Each Figure shows small variation to plotted data, and results are consistent with sequential, ongoing failure reflecting crushing and failure at multiple dispersed points rather than a single catastrophic failure event. A large increase to measured maximum load is seen to occur between 1400°C and 1500°C.

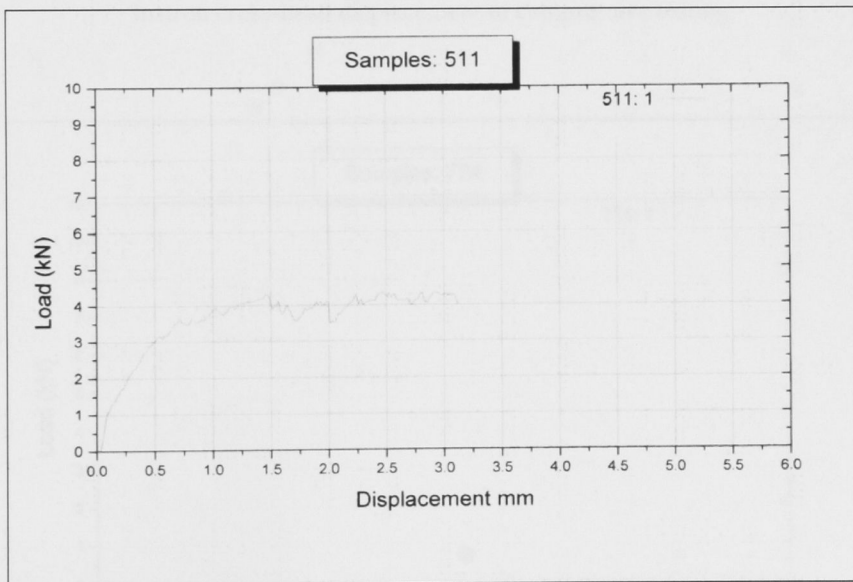


Figure 5.16: Group A sample 511, 1100°C, Load at Maximum Load, kN, as a function of Instron cross-head displacement in compressive testing.

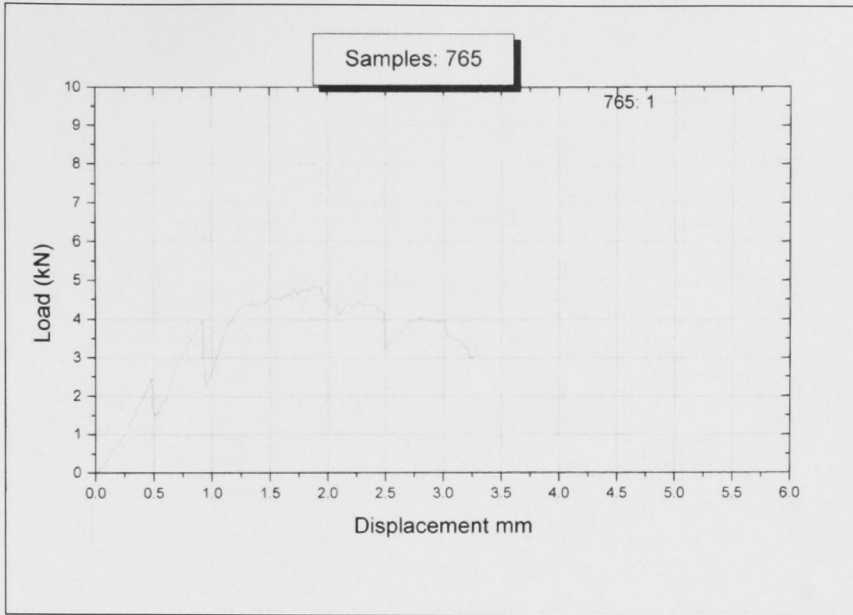


Figure 5.17: Group A sample 765, 1200°C, Load at Maximum load, kN, as a function of Instron cross-head displacement in compressive testing.

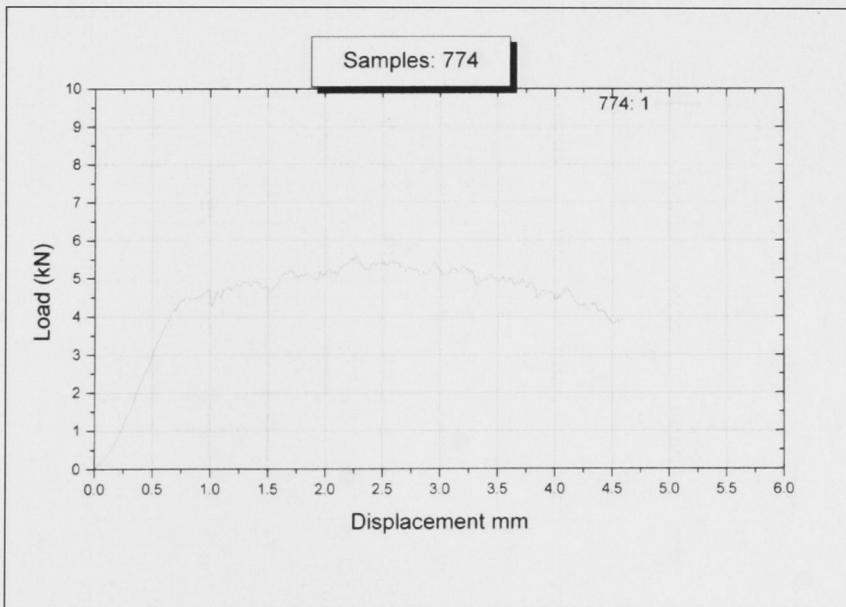


Figure 5.18: Group A sample 774, 1300°C, Load at Maximum Load, kN, as a function of Instron cross-head displacement in compressive testing.

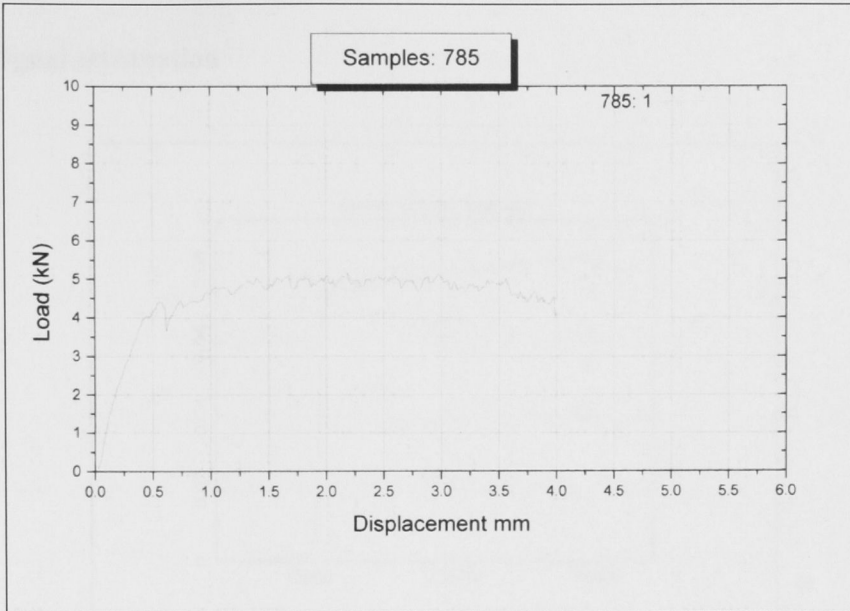


Figure 5.19: Group A sample 785, 1400°C, Load at Maximum Load, kN, as a function of Instron cross-head displacement in compressive testing.

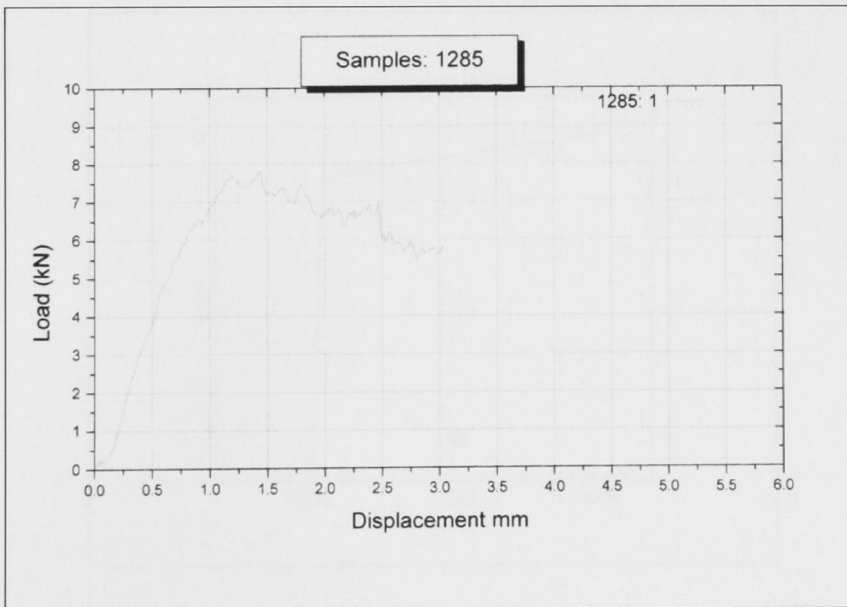


Figure 5.20: Group A sample 1285, 1500°C, Load at Maximum Load, kN, as a function of Instron cross-head displacement in compressive testing.

5.2.6 Signal attenuation

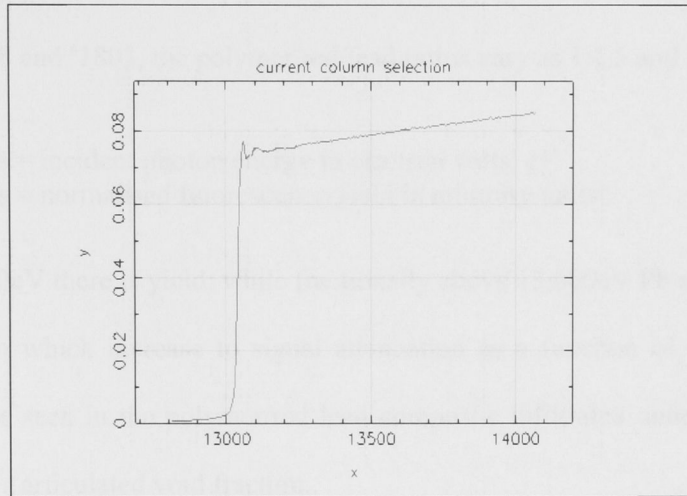


Figure 5.21: Results of Tsukuba Beamline testing, sample #1768, where X axis = incident photon energy in electron volts, eV and Y axis = normalised fluorescence yield in arbitrary units

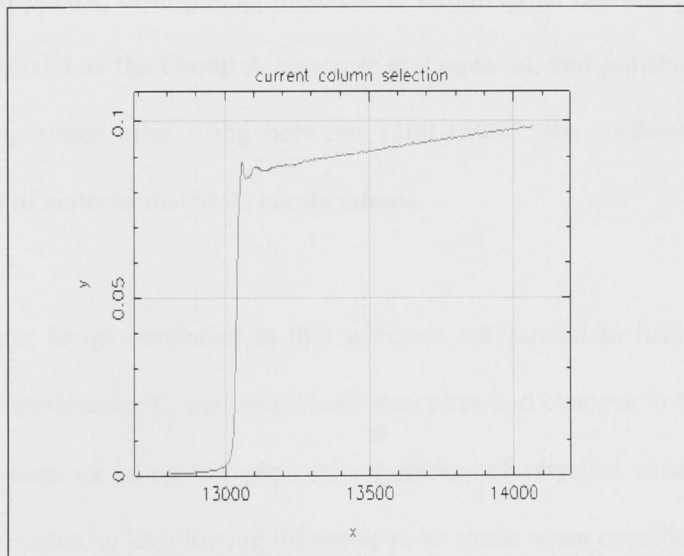


Figure 5.22: Results of Tsukuba Beamline testing, sample #1803, where X axis = incident photon energy in electron volts, eV and Y axis = normalised fluorescence yield in arbitrary units

Figures 5.21 and 5.22 show results of Tsukoba Beamline testing of a standard Group A sample sintered to 1100C, infiltrated with a polymer/red lead composite under vacuum, hardened, cured and sectioned to 50 μ m. In each of Figures 5.22 and 5.23, samples #1768 and #1803, the polymer red/lead ratios vary as 1:1.5 and 1:2.5,

X axis = incident photon energy in electron volts, eV

Y axis = normalised fluorescence yield in arbitrary units

Below 13,000eV there is yield, while fractionally above 13,000eV Pb additions create a structure in which increase to signal attenuation as a function of increase to Pb distribution is seen in the polymer/red lead composite infiltrated under vacuum into the structure's articulated void fraction.

5.3 Sample morphology

Pages 90-95 show a range of electron micrograph images that includes unsintered, unmixed cenospheres, cenospheres mixed with kaolin as an unsintered porous solid, cenospheres mixed as the Group A structure and sintered, and polished thin sections of sintered structures after firing between 1100-1500C, the surfaces of cores and fracture faces of sintered materials combinations.

The backscatter images included in this selection correspond to firings at specified maximum temperatures, °C, and show both structures and changes to those structures that may be seen as being either in corroboration of physical measurements and derived calculations, or as allowing inference to be made when considered in the light of those data.

Polished thin sections allow the observation of a selection of the micro structures that are critical to the formation and understanding of post-firing properties. However,

they also simultaneously present a problem, in that each is a single cross-sectional slice of a sample from which inference might be drawn, but which does not otherwise provide explanation of three-dimensional structures above and below the plane of the image.

Images of unfractured-surface formations assist the understanding of the three dimensional sintered structure, but, like the thin sections, are limited as predictors of three-dimensional structures below the surface. Figures 5.33 and 5.34, much larger-scale images, are the result of the manipulation of data obtained by x-ray tomography. Taken together, the thin sections, the faces of sintered samples and polished sections in conjunction with tomographic imaging allow a more accessible understanding of this structure.

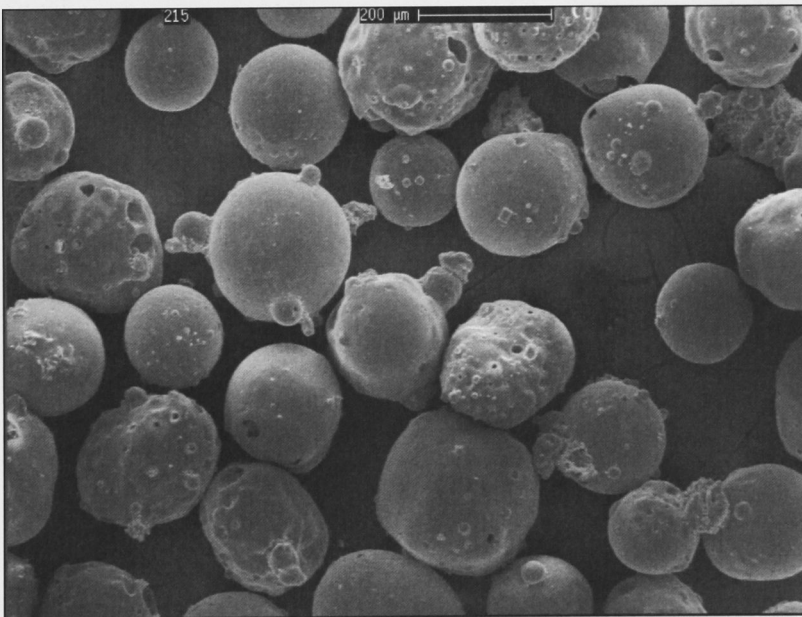


Figure 5.23: Electron micrograph of unsintered SL500 cenosphere particles mounted on carbon tape

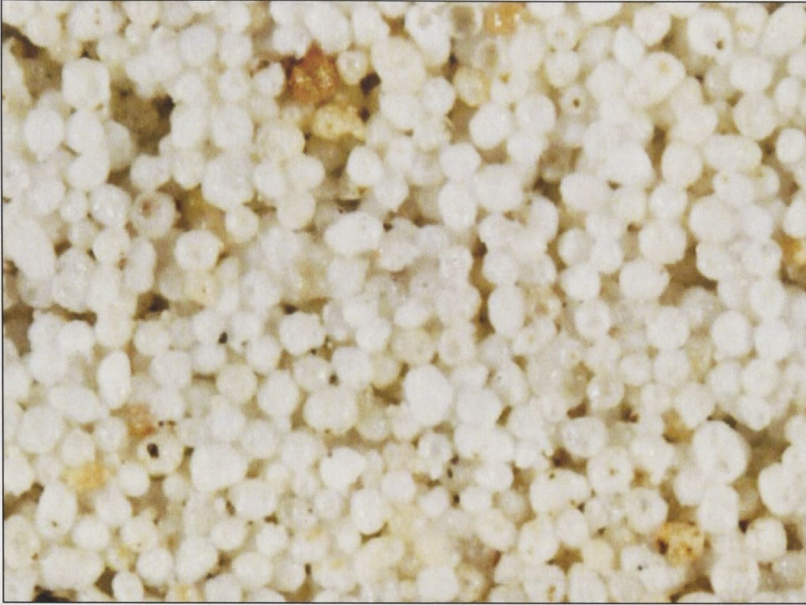


Figure 5.24: Enlarged photographic image of surface of a Group A sample after sintering to 1100°C, initially x5.

Note that Figure 5.25 shows that the sintered body is highly porous and clearly shows individual cenosphere particles that are also seen as unsintered in the unsintered, non-compound form in Figure 5.23.

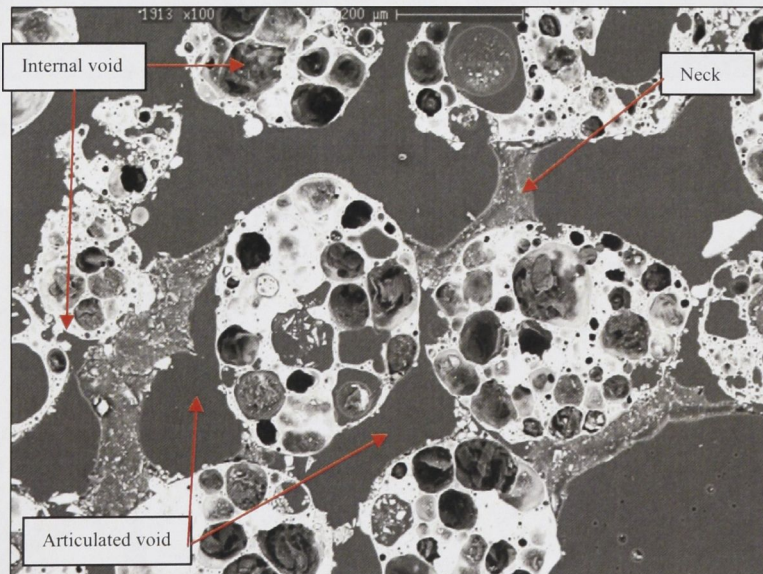


Figure 5.25: Group A, cenospheres + kaolin + Frit, before sintering. An electron micrograph of polished thin section embedded in epoxy resin.

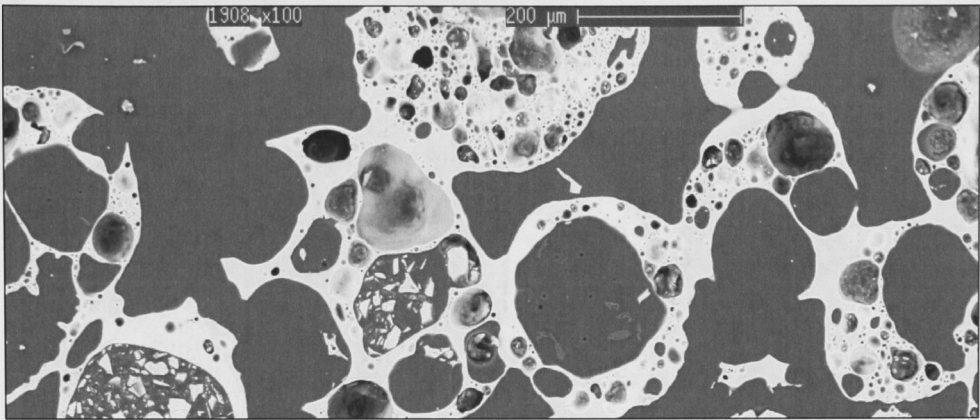


Figure 5.26: Group A, sintered to 1100°C, electron micrograph of polished thin section

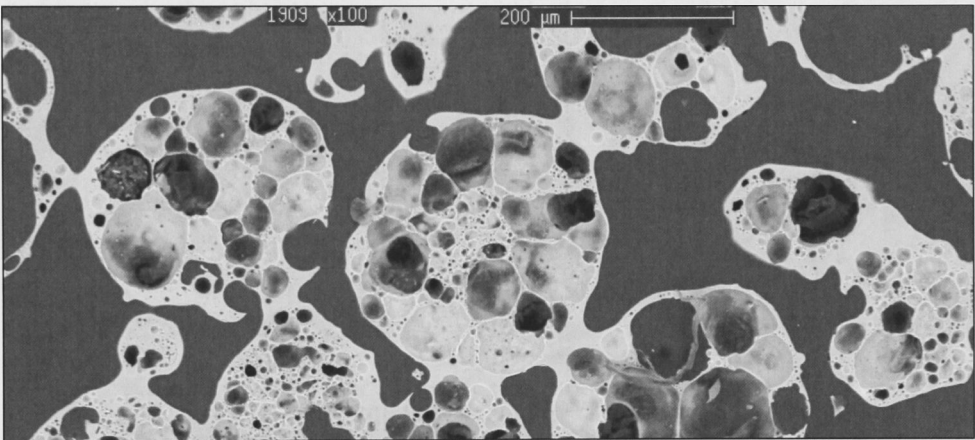


Figure 5.27: Group A, sintered to 1200°C, electron micrograph of polished thin section

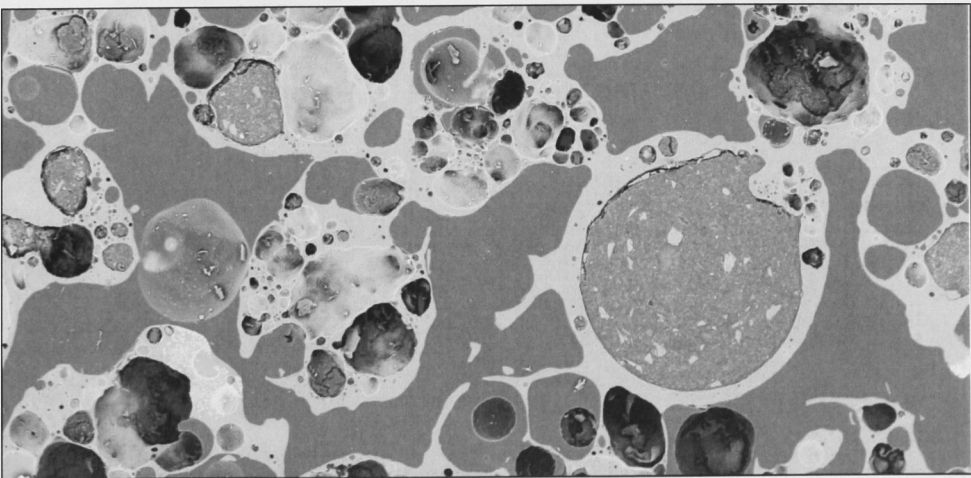


Figure 5.28: Group A, 1300°C, electron micrograph of polished thin section

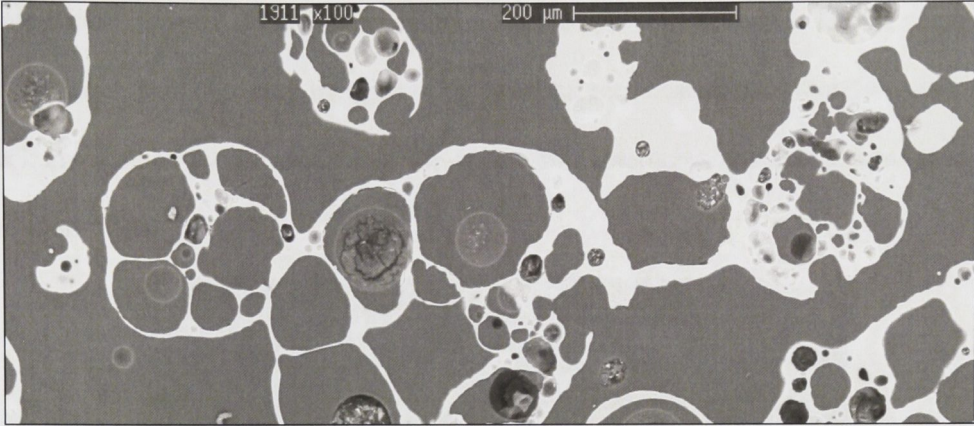


Figure 5.29: Group A, sintered to 1400°C, electron micrograph of polished thin section

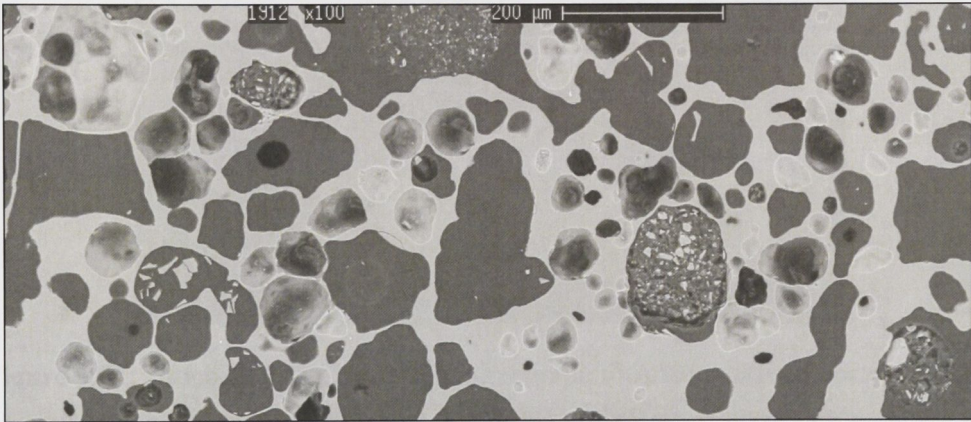


Figure 5.30: Group A, sintered to 1500°C, electron micrograph of polished thin section

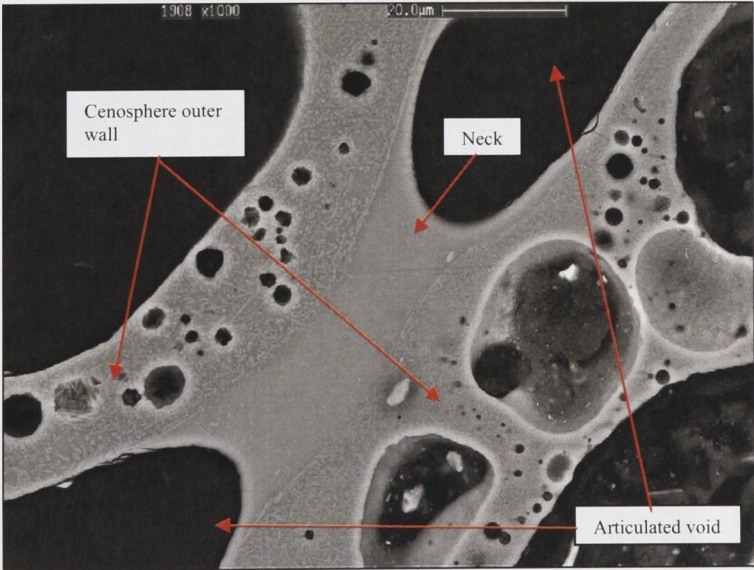


Figure 5.31: Group A, 1100C, electron micrograph of a polished thin section, showing the outer shells of two cenospheres, joined by a sintered neck structure.

Note that in Figure 5.31 the shells contain a range of micro voids that are the result of initial formation. The outer margins of the shells at the point of their interface with the neck are defined by the absence of the needle-like microcrystalline structures seen in the shell walls.

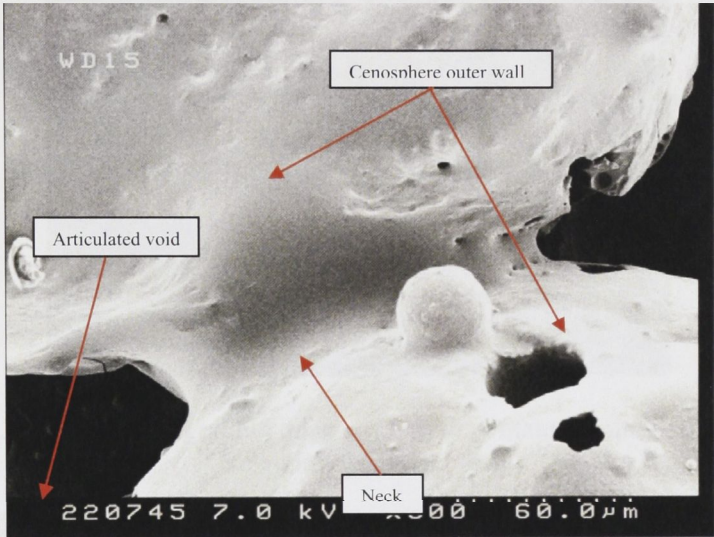


Figure 5.32: Group A, 1100C, electron micrograph showing two cenosphere particles joined by a typical neck structure

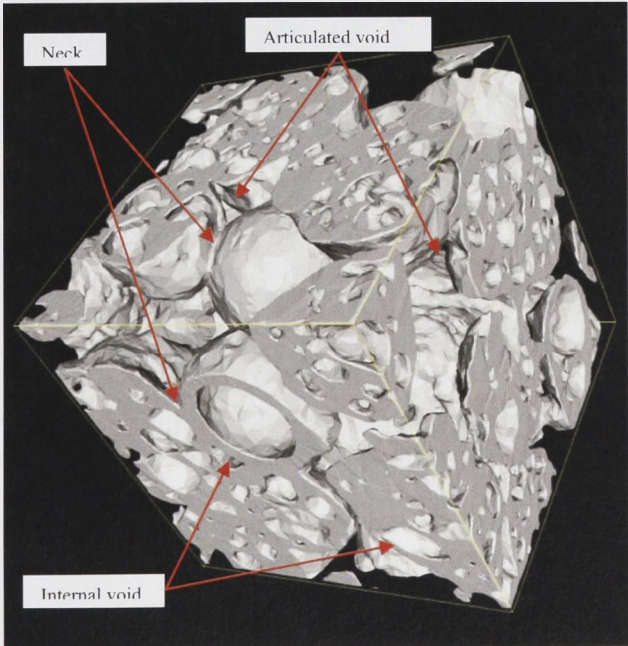


Figure 5.33: X-ray tomography image of Group A material sintered to 1100°C

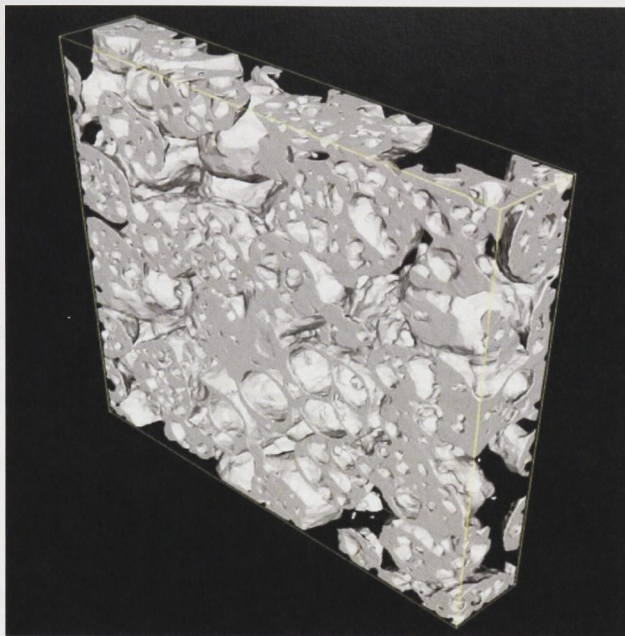


Figure 5.34: X-ray tomographic image of Group A material sintered to 1100°C, selection from data set

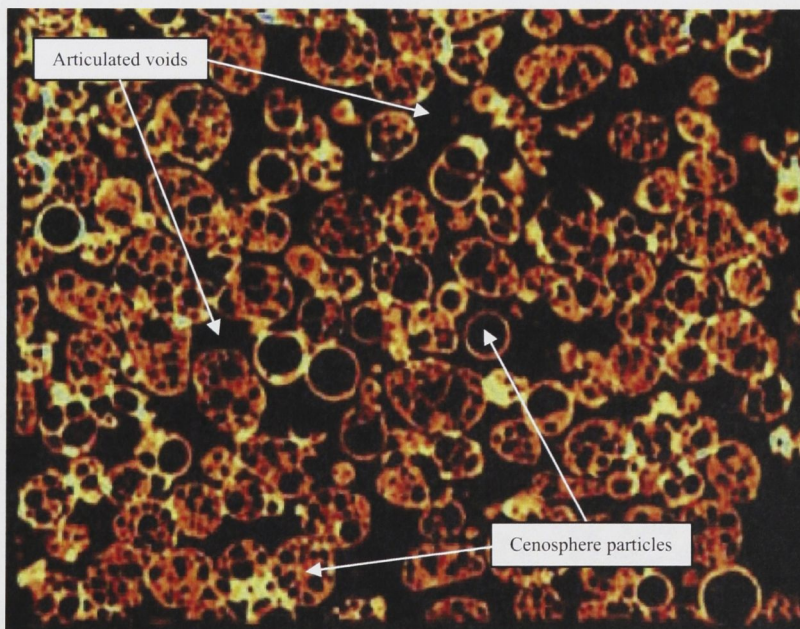


Figure 5.35: Image of section of a single 100µm slice taken from a tomographic X-ray MPEG movie of a 5mm core cut from a Group A sample after sintering to 1100°C

Chapter 6 Discussion

The testing of compounds of cenospheres, kaolin, frit 4194 and water allowed the choice of the materials ratios that are the foundation for this discussion.

6.1 Structure formation

The unsintered neck/meniscus structure was identified in an electron micrograph of a compound of cenospheres and kaolin that had been mixed, compacted and allowed to dry in air. When dry the cenospheres-based compound had formed a solid structure through which air could be sucked while continuing to retain its structural integrity. Appraisal of a range of similar dry, unsintered cenosphere-kaolin structures, where the sole variable was the weight of kaolin that was added to a standard 10g batch of cenospheres, saw the decision to further examine the sample that contained 3.5% added kaolin.

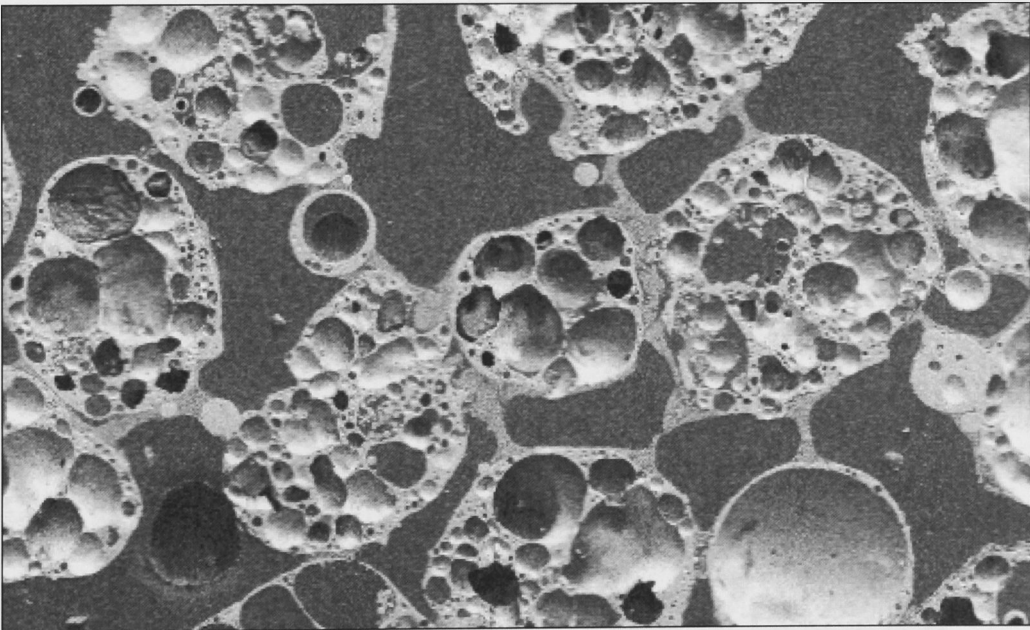


Figure 6.1: Electron micrograph of a polished thin section of the unsintered cenosphere-kaolin compound, x250

Figure 6.1 shows an electron micrograph of a 30 μm polished thin section of the dry, unsintered cenosphere-kaolin compound referred to above, which at this point contained no fritted material. The kaolin fraction, 0.35g/3.5%, added to 10 gm cenospheres and mixed with 6.0ml water, has formed neck-like structures that link the outer surfaces of cenospheres particles, a structure that offered potential for the creation of a solid sintered porous structure. Figure 6.2, x2000, shows sections of the same neck structure in which aggregations of lamellar kaolin particles are in approximately parallel alignment, having been carried in water within the structure's void fraction formed during mixing and packing of the cenosphere particles. The resultant water/kaolin structure is a meniscus formed in satisfaction of the molecular forces existing in the surface film, leading to the contraction of the volume into a form with the least surface area.

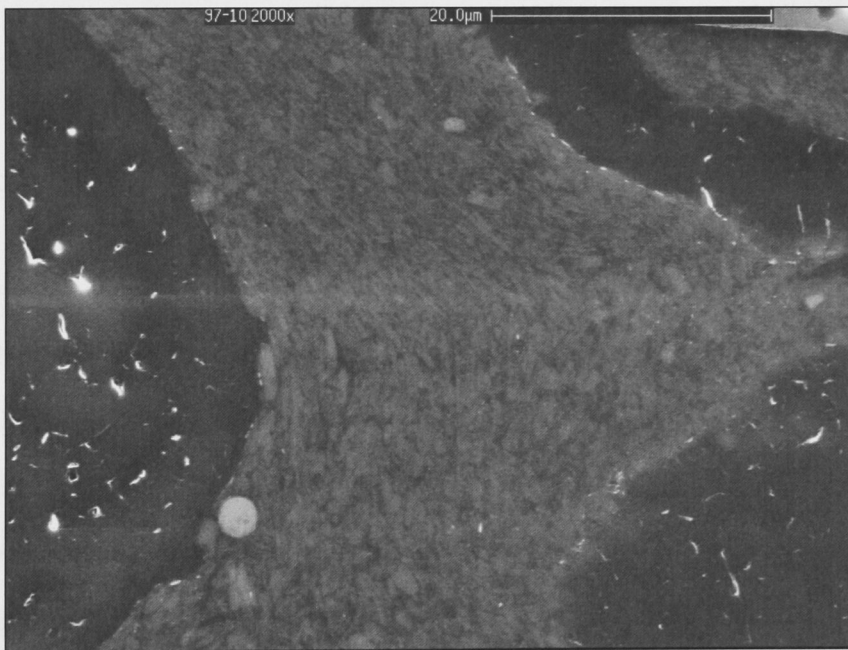


Figure 6.2: Electron micrograph of aggregated kaolin particles, x2000, enlarged detail from Figure 6.1

The random distribution of cenosphere particles within the samples tested in this research results in a corresponding but not necessarily equally random distribution of void geometries and volumes within sample cross sections. Notwithstanding that observation it will be shown that within such observed random distributions there is

- (i) An optimal ratio of dry particulate materials and water such that the movement of particles suspended within the added water in the formation of the meniscus is both facilitated and achieved and which on sintering produces the contact-point fusion of particles that constitute the structure.
- (ii) Insufficient kaolin and other materials added to either totally fill the structure's articulated void fraction, or block it to the extent that it is no longer articulated.
- (iii) It is proposed that the volume of kaolin particles added to the cenosphere batches is insufficient to completely absorb within its own void fraction the added water and so prevent the movement of the water\kaolin\frit compound and the formation of the meniscus seen in close association with either contact points or the closely adjacent shells of cenosphere particles.

Sintering of samples allowed SEM examination of the neck structure. Figure 6.3 shows cenosphere particles fused together by neck structures described above. This shows the upper face of a 25mmx5mm diameter core removed from the central longitudinal axis of a standard cylindrical sample after sintering to 1100°C. The differing sizes and shapes of the constituent SL500 grade cenospheres that constitute its scaffold are seen, as well as the interstitial spaces that are formed by the fusion one to another of those particles by the neck structures seen in Figure 6.1, above.

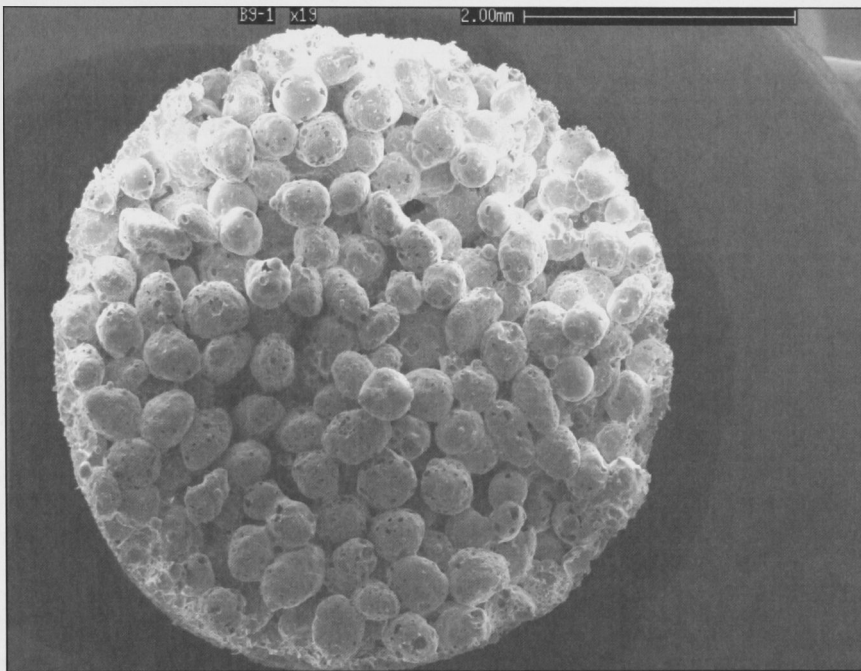


Figure 6.3: Electron micrograph of a Group A, 5mm core sample, x19. All particles are joined by neck structures not clearly visible at this magnification

Figure 6.3 shows the upper face of the core and is not fractured or otherwise altered. The black spots and specks on the surface of individual cenosphere particles are points at which the outer shell has been broken, during formation, during collection and grading, or during decrepitation at approximately 300°C. While it is clear that individual elements of the void fraction formed by contact-point sintering are neither regular in geometry nor distribution, it is proposed that the absence of other than spherical or ovoid particles creates a void geometry and distribution which conforms to certain maxima that are themselves defined by the profiles and distribution of those spherical and ovoid constituents.

Figures 6.41-6.44 show 3-D images from different perspectives of the same solid structure from a data set selected from the tomographic X-ray analysis of the sample seen in Figure 6.34, above. The relationship of the cenosphere particles one to another and the

void fraction their fusion creates are seen, including detail of the nature of the articulation of the void fraction that is otherwise only implied by the data obtained from physical testing, measurement of sintered-structure properties and SEM imaging.



Figure 6.41

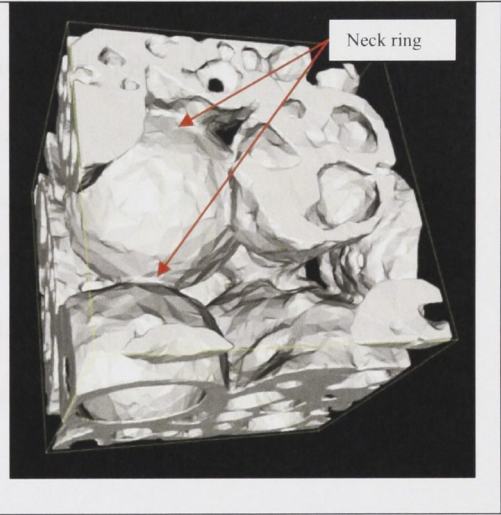


Figure 6.42



Figure 6.43

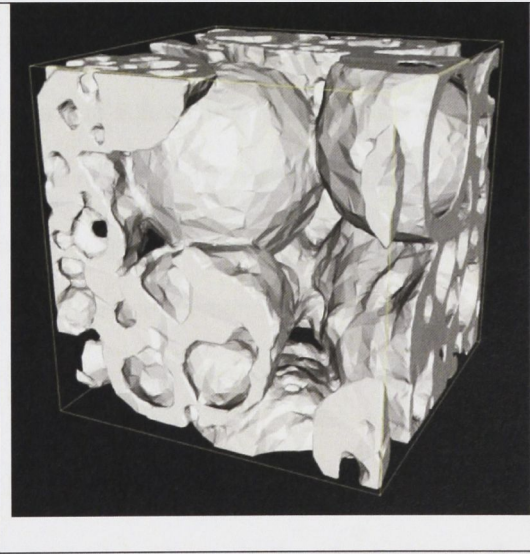


Figure 6.44

Figure 6.41-6.44: 3-D tomographic images of the same Group A sintered structure, 1100°C, illustrating the relationship of the cenosphere particles and the articulated void structure

Figures 6.41-6.44 also shows cross-section detail of the interiors of large particles containing multiple enclosed voids. The placement during mixing of the kaolin/frit composite so that when sintered it forms a collar-like structure around the contact points of particles is also depicted. The multiple angular planes on the surfaces of the cenosphere particles are an artifact of 3-D visualisation of the relevant data set. Variation to cross-section geometry of internal skeletal members within large particles illustrates the problem of the calculation of individual particle void volumes as well as particle density, an issue that can only be solved through the use of particles with diameters smaller than $80\mu\text{m}$, for at that diameter and below particles are almost entirely spherical and multiple enclosed voids are rarely found and the thicknesses of the walls of single-void spheres are also more uniform.

Figure 5.32, Chapter 5, shows detail of two cenospheres joined by a characteristic neck structure with an external blister explained by Raask, E., [1] as a consequence of the generation of too much gas within the ash particle's formation phase, when it burst leaving a blob with the process of expansion then repeated. The three holes seen on the upper surface of the lower of the two spheres show the thickness of the cell wall at that point as well as an interior cavity, with the convex surface surrounding the smaller of the two holes suggesting a enclosed void that is characteristic of cenosphere particles of this size.

The presence of holes on the surface of cenospheres is important in the process by which the sintered structure is infiltrated with polymers and polymer composites under vacuum.

Where surface holes exist the infiltration of part or whole of the interior of a particle has the potential to increase the volume of polymer alone and that of a polymer/mineral composite that may be infiltrated into the structure's void fraction. The neck that fuses and joins the surfaces of adjacent cenosphere particles is typical of those seen in the sintered structures across the temperature range 1100-1500°C.

Figure 6.5, below, shows a series of twelve sequential images that represent X-Ray tomography slices selected at approximately 25 frame intervals through a 400 frame, 5mm core taken from the longitudinal axis of a Group A structure after sintering to 1100°C. The images allow the non-destructive observation of the internal structure of constituent cenosphere particles as well as the distribution of voids formed by their random packing, the addition of the added ceramic neck material and the porous solid structure formed by its subsequent sintering to 1100°C. The images in Figure 6.5 were taken from a much larger data-set core in which the image depicted in Figure 5.35 coincides with its diameter. Each of the sequential images seen in Figure 6.5 was selected at approximately 200µm intervals and defined using the same pixel-based co-ordinates.

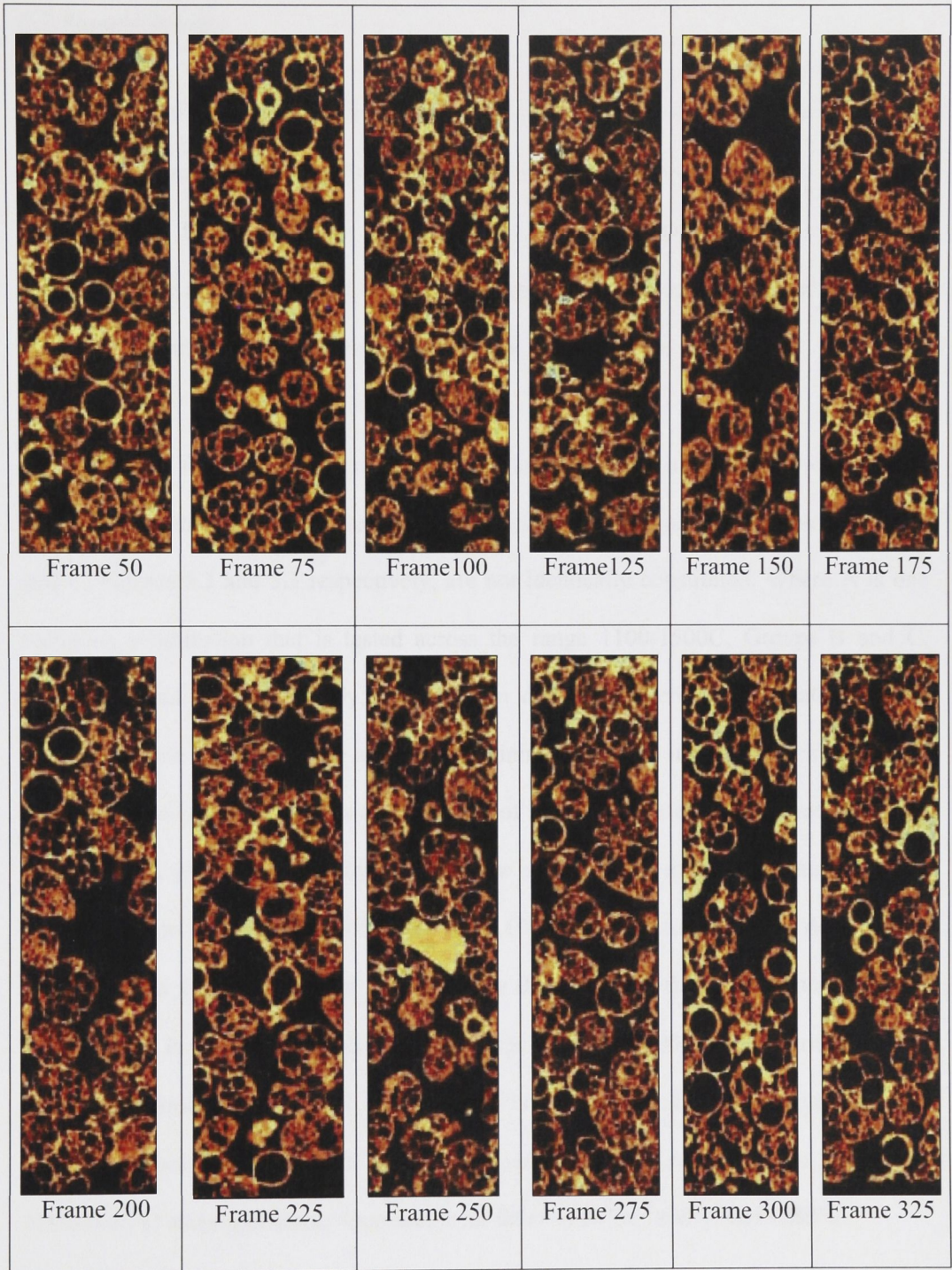


Figure 6.5: Distribution of particles and voids at 25 frame intervals

6.2 Sample density

As outlined in Chapter 4, Experimental Methods and Techniques, the materials-combination common to each of the Groups tested is that of Group A and it is against the data collected from it that the results of both Groups B and C are compared and contrasted. The results for variation to constituent materials ratios represented by Groups D-F were not sufficiently different to justify further examination.

Density results for Group A, Figure 5.1, show a small increase in density between 1100C and 1400C, with significantly greater increase between 1400C and 1500C, but Groups B and C, Figures 5.2 and 5.3 respectively, are not identically constituted. Where A is one materials combination that is tested across the range 1100-1500C, Groups B and C, Tables 4.6 and 4.7 respectively, are each ten different materials combinations tested across the same range, with the aim of determining the effect, if any, on their properties of variation to constituent ratios as a function of maximum sintering temperature. While there is small variation to density in results for both B and C at the maximum sintering temperatures to which each was fired between 1000-1500°C, comparison of densities for Groups B and C at 1400°C and 1500°C show divergence at those temperatures that is greater than is recorded for the same Groups at 1100-1400°C. Comparison of the densities of Group A, Figure 5.1, with those of both Groups B, Figure 5.2, and C, Figure 5.3, show densities for B and C marginally increased over those of Group A between 1100-1400°C and significantly increased over those of A for 1400°C and 1500°C.

Figure 5.4 compares results for variation to average density for Group A and C5 and illustrates the potential for Group A density to be amended by the incorporation of additional materials combinations.

Results for C5 at 1100°C are approximately equal to those of Group A at 1400°C. By adding materials that alter the Group A solid-neck fraction composite, while leaving the weight of the primary cenosphere fraction constant, it is possible to simultaneously produce sintered structures of different densities that would otherwise require separate firings with different maximum temperatures. In this case C5 varies from the base Group A composition through the addition of 6% silica fume, 5% tin oxide and 0.7% cobalt carbonate.

Figure 5.4, while showing convergence of density values for Group A and C5 at 1200°C and 1300°C shows further divergence with C5 increasing in density over Group A at 1400°C and 1500°C, with the increase between 1450°C and 1500°C almost double that seen between 1400°C and 1500°C.

It is proposed that the kaolin/frit compound used in the production of the neck fraction has no equivalent in industrial usage. The closest illustration of the effect of sintering in industrial applications is seen in both changes to both microstructures and void fractions in Figures 6.61-6.64.

In a traditional clay-based ceramic the intention in its sintering is the elimination of as much of its void fraction as is possible in the achievement of a state that is as close as is possible to theoretical density for that compound, while not losing its pyroplastic properties that would lead to slumping, deformation and loss of its intended application, Flynn (2000).

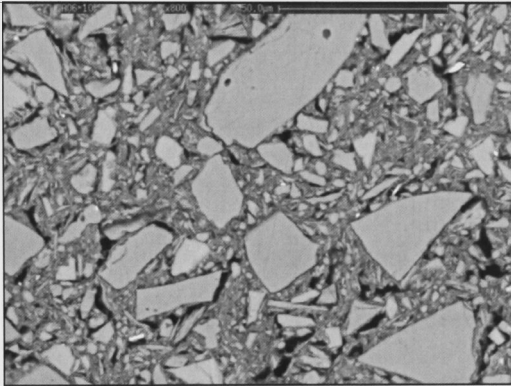


Figure 6.61: Cone 06 (960°C), x800

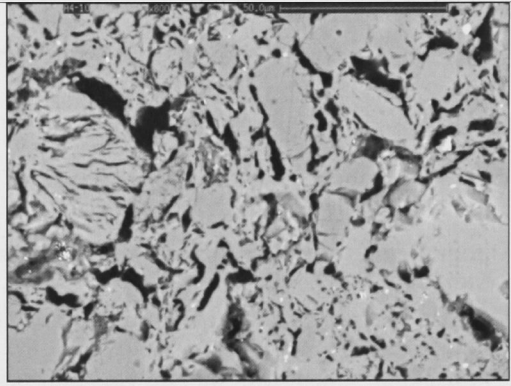


Figure 6.62: Cone 04 (1050°C), x800

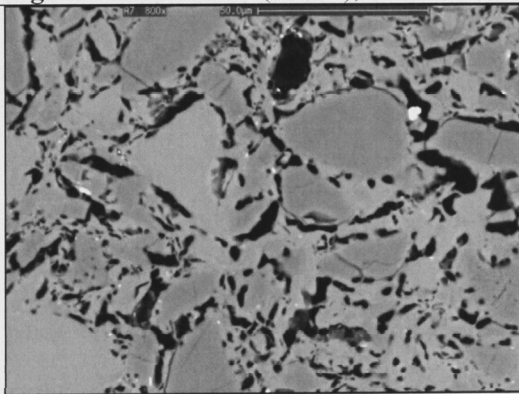


Figure 6.63: Cone 7 (1215°C), x800

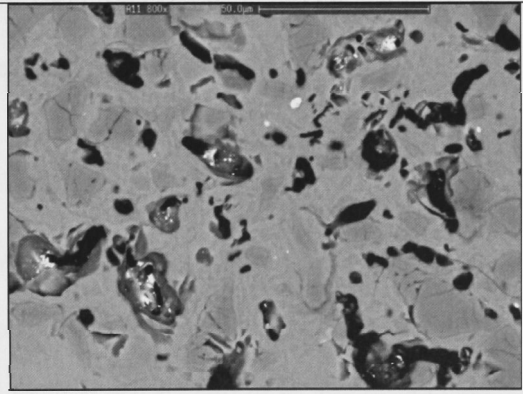


Figure 6.64: Cone 11 (1294°C), x800

Figures 6.61-6.64: Electron micrographs of a stoneware clay body, sintered to four temperatures in the range 960-1294°C, illustrate changes to microstructures, polished 30µm thin sections, x800

Porosity in a fine-particulate clay-based composite is long understood and shown as reducing as a function of progressively higher maximum sintering temperatures, resulting in increasing density of the solid. The number of articulated voids decreases while initially the number of blind or sealed voids increases simultaneously with that decrease. However, with further increase to maximum sintering temperature the number of sealed voids below a threshold diameter decreases and the geometry of those remaining voids that are too large to be eliminated in the increasing pyroplasticity of the body become rounder and softer in profile.

In Figure 6.61-6.64 visible sealed voids initially increase with sintering temperature. Micro voids that are not visible decrease significantly across the same temperature range. In Figure 6.63 there is a further decrease in void numbers and an observable increase in void volumes, while in the final image, Figure 6.64, numbers of voids have decreased significantly and overall void volume has decreased.

In this study the sintered structure that is characterised is comprised by a mixture of particle sizes that range from macro for cenospheres, 35-250 μm , to micro for kaolin, 0.1-1.0 μm . Those particles that constitute the neck fraction occupy part of an articulated void fraction that is calculated after sintering on the basis of relative densities as occupying approximately 20% of the bulk volume of samples. The percentage of the articulated void volume that is occupied by the sintered neck fraction is unknown and has not been able to be determined in this study. However, electron micrographs, the measurement of sample

permeability as a function of maximum sintering temperature and X-Ray tomography combine to suggest that the actual volume loss on mixing and sintering is not substantial.

6.3 Permeability

Figure 5.6 shows the point at which 160 sets of results are distributed; each is an average of five measurements. Values for permeability lie within the range $P = 0.5-2.5$, where none of the results falls below 0.5, allowing the conclusion to be drawn that all samples so depicted are permeable. Section 4.16 describes the method by which the flow rate per 2mins through the sample was achieved and, in that the head of water above the sample was maintained at a constant level during the collection period, such that water was added at a rate equal to that of its depletion, it is proposed that results may be regarded as valid and reliable.

While electron micrographs and X-ray tomography images show both the solid structure and the articulated void fraction that it forms, X-ray tomography images, Figure 6.41-6.44, also show that distribution of particles and the neck fractions that fuse them together are random, with the result that the conclusion must be drawn that permeability exists despite this random distribution and that the random distribution of the neck fraction structures is achieved in such a way that such distribution neither impedes nor impinges upon flow volumes for water under constant pressure in its passage through samples. These results and the conclusion drawn from them bring important implications for the structures and their potential uses in their infiltration by polymer compounds

under vacuum and their absorption, transmission and diffusion of heat when used in high-temperature insulation.

6.4 Compression testing of uninfiltreated samples

Figure 5.8 shows average increase to stress at maximum load for Group A samples. Where increase to stress between 1100°C and 1400°C is only marginal, the increase between 1400°C and 1500°C is almost six times that seen between 1300°C and 1400°C, with all points on Figure 5.6 reflecting changes to density in Group A materials seen in Figure 5.1.

Failure of Group A samples at maximum load is not consistent with results and expectations for solid, fine-particulate dense sintered ceramics. Sammis and Ashby (1985) examined the process of progressive microfracture in brittle porous materials, considering the roles of pore size and confining pressures compared with experiments with glass and brittle plastic. Using cylindrical forms subject to axial compression as a function of confining pressure it was found that unconfined samples tended to fail by “slabbing”, that “individual micro cracks initiate at flaws or stress concentrations, or small (often) grain-sized cracks left by its earlier thermal history. When cracks emanate from the holes, the shape of the unit cell changes....the cracks grow between each other, carving the solid into beams which become narrower and longer as the cracks extend....Cracks which were not neighbours when they were shorter become neighbours

as they grow longer – although the total number of cracks has not changed...As cracks grow from the holes the modulus of the solid falls.”

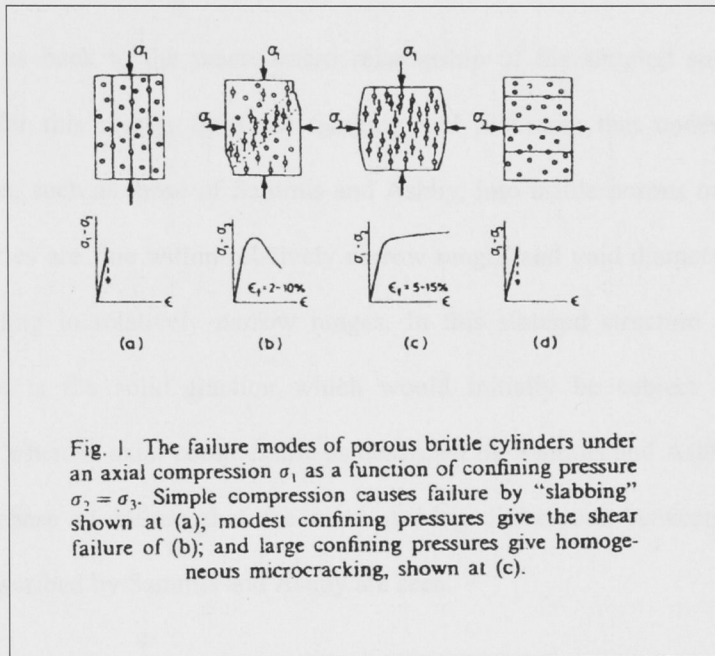


Figure 6.7: Failure modes of porous brittle cylinders under axial compression, Sammis and Ashby (1985)

Sammis and Ashby state further, “Brittle solids fail in compression by a process of progressive microfracture. Acoustic emission shows that micro fracturing begins at about one half the ultimate failure stress and that the number and length of the micro cracks increases as the stress is increased further, causing the sample volume to increase even though the stress state is compressive. Near failure the density of micro cracks and the dilatency increases rapidly. Microscopy shows that individual micro cracks propagate in a direction that is more or less parallel to the largest principal compressive stress until they link to form one of the several types of macroscopic failure. In their conclusion they

state, “After an initial period of unstable growth, the cracks grow stably, meaning that the loads must be increased to cause further crack extension, the cracks ultimately become unstable again and propagate catastrophically.”

This brings us back to the macro/micro relationship of the sintered structure and its divergence for this reason from the thinking and processes that underlie reports of investigations, such as those of Sammis and Ashby, into brittle porous materials where matrix particles are fine within relatively narrow ranges and void diameters are equally fine and falling in relatively narrow ranges. In this sintered structure it is the neck material that is the solid fraction which would initially be subject to the failure mechanisms when in axial compression as described by Sammis and Ashby, and it is in this initial phase of failure that the most striking differences between it and those structures described by Sammis and Ashby are seen.

The network of normal contact branches depicted in Figure 2.4, while referring to the points of contact between solid salt tablets, may be considered in relation to the theoretical distribution of contact points and particle-particle contact forces in the Group A sintered structure when in axial compression. Failure in compression in the sintered sample is not caused by the swift growth of micro cracks which “propagate in a direction that is more or less parallel to the largest principal compressive stress” and which with increased load propagate catastrophically.

With the density of individual particles being determined not only by their internal geometry, whether or not they are a single sphere or multi-sphere structures, but also by

variation to their wall thickness and that of internal skeletal structures, see Figure 6.1, failure in compression is not swift and catastrophic but a succession of multiple, cumulative small failures which sees neck material and cenosphere particles fail locally when a load sufficient to cause the failure of the weakest element of part of a small local structure is applied. The small failures may be both individual and sequential or the sequential simultaneous failure of groups of two or more otherwise local structures with similar or equal properties in compression.

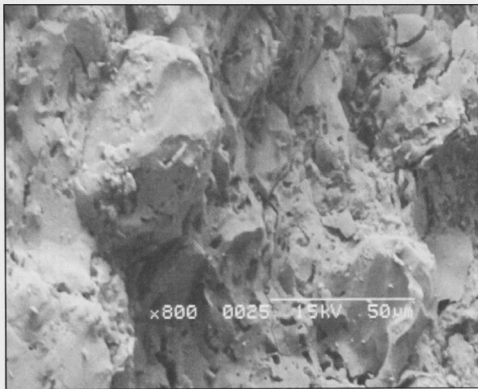


Figure 6.8(i)

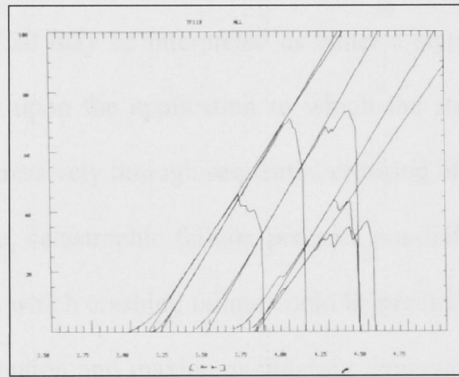


Figure 6.8(ii)

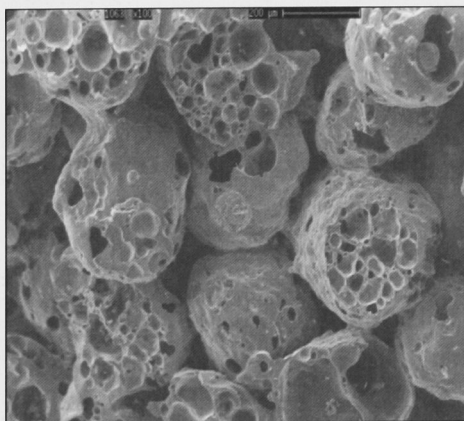


Figure 6.8(iii)

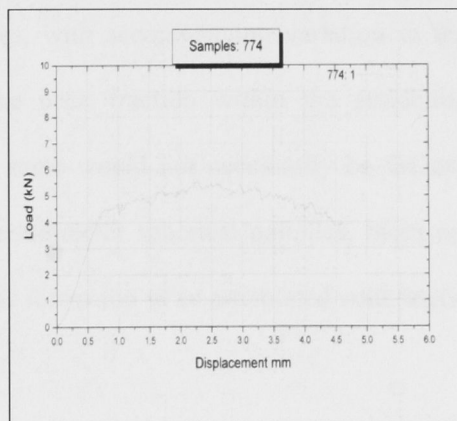


Figure 6.8(iv)

Figures 6.8(i)-(iv): Comparison of fracture-face images and differences in Instron recordings of failure in compression of two ceramic samples.

Figures 6.8 (i)-(iv) compare images and associated Instron recordings of compression of two types of sintered-ceramic samples. Figure 6.8(i) shows a dense, low-porosity stoneware body sintered to 1300°C, (Appendix 15), and Figure 6.8(iii) depicts the fracture face of Group A materials that had been sintered to 1400°C. Note that the cenosphere particles reveal internal structures seen in Figure 6.8(iii), illustrating progressive, crushing failure reflected in the recording shown in Figure 6.8(iv) as opposed to the sudden catastrophic failures seen in the recordings in Figure 6.8(ii).

Implications of Progressive Failure

Progressive failure seen in Figures 5.16-5.20 may be interpreted as either a significant disadvantage or an advantage, depending upon the application to which the structure might be applied. The capacity to fail progressively through sequential crushing of micro structures, rather than by swift destructive, catastrophic failure, presents possibility for the further development of this structure in which crushing failure could be predicted as a function of cenosphere particle-size distribution and maximum-sintering temperature. It is proposed that the range of random particle sizes and their equivalent spherical diameters seen in the Group A structures, with accompanying variation to individual particle densities and distribution of the neck fraction within the structure, would facilitate controlled crushing, where the same would not necessarily be the case for a structure comprised by uniformly smaller-diameter spherical particles, more narrow in their distribution ranges and facilitating the formation of an articulated void fraction more regular in its geometry and volumes.

Variation to density, Figure 5.1, and increase to stress at maximum load, Figure 5.8, may in part be explained by changes to the microstructures of thin-section images seen in Figures 5.26-5.30. The most notable differences between thin-section images for 1100°C and 1500°C lie in the distribution of what in the 1100°C sample may be regarded as normal and expected volumes of solid-neck fractions and their distribution within the image. The image for the sample fired to 1500°C, however, shows not only large areas of what would otherwise be voids filled by a solid-ceramic fraction, but also, and most interestingly, thinning of the walls of the cenosphere particles. Apparent in-filling of voids within particles with the same solid-ceramic fraction suggests that, while speculative, what is seen in this image, Figure 5.30, is a consequence of a progressive and accelerated melting above 1400°C of the alumino-silicate walls and internal skeleton of the particles, either in conjunction with or in addition to the neck material.

Imagery of neck structures after firing to 1500°C show the formation of interlocking crystalline structures that suggest the material from which they have grown has been sufficiently molten for a period of time appropriate to permit and facilitate their growth.

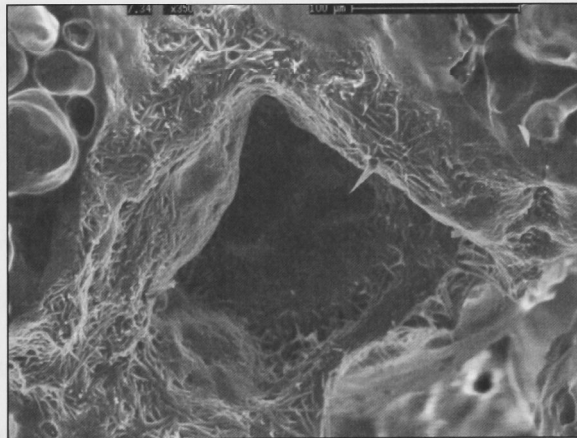


Figure 6.9: Electron micrograph, void fraction and neck structure, Group A, 1500°C, showing crystal growth in association with neck materials in fused particles, x350

There is no electron micrograph image available, other than Figure 5.30, of reduced or altered void-fraction volumes that confirms the melting-and-transport of neck-material hypothesis in the explanation of the marked increase to densification of the structure that is seen between 1400°C and 1500°C. Despite having been sintered using the same heating-and-cooling firing cycle to 1400°C, Group A structures show no crystal development similar to that of Figure 6.9, above, and it should be noted that the internal walls of the particle in Figure 6.10 do not appear altered or out of the ordinary.

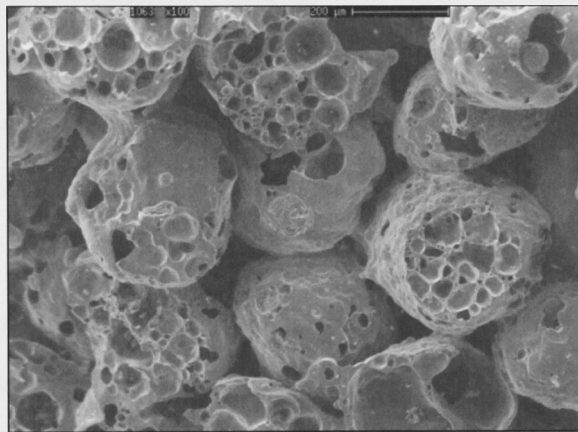


Figure 6.10: Void fraction and neck structure, Group A, fracture face, 1400°C, showing intact internal skeletal structures in fused particles, x100

6.5 Infiltration of the sintered structure with a polymer

Only Group A samples sintered across the range 1100-1500°C were infiltrated under vacuum with a polymer. Measured strength increases, therefore making it more suitable for use as a structural material.

The purposes of infiltration are two-fold,

- a) the production of a more coherent structural material with potential for use in thermal insulation and sound proofing

- b) the introduction of radiation absorbing substances into the structure's void fraction, thus making the new material suitable for a range of signal attenuation applications, While temperature and sound insulation properties have not been tested, preliminary testing of signal attenuation properties has been performed, see Figures 5.19 and 5.20.

The properties measured in compressive testing after vacuum infiltration of the sintered structure by a polymer, as described in Chapter 4, 4.20.2, are radically different from those of the uninfiltreated structure described above. Figure 5.5 shows variation to average density for Group A structures before and after infiltration, with average density at each of the five firing points approximately double that of averages for uninfiltreated samples.

In Figure 5.13 values for variation to load at maximum load, kN, for sample averages at each of the firing points diverge significantly. Where in uninfiltreated samples the increase to average maximum load values in the sintering range 1100-1500°C is insignificant until 1400°C, the rate of increase for infiltrated samples across the range 1100-1500°C is almost constant with increase for 1500°C double that of 1100°C. Increase at 1500°C for infiltrated samples is almost five times that of the increase seen for uninfiltreated samples.

Variation to modulus of elasticity is seen in Figure 5.14, where values for uninfiltreated and infiltrated samples are compared with those of the uninfiltreated C5 sample. Increase for infiltrated samples is almost constant until 1400°C, then increasing to 1500°C, while values for uninfiltreated samples, with minor variation between 1100-1400°C show similar trends. Increase over the 100°C interval to 1500°C does not reflect that of infiltrated samples.

6.5.1 Infiltration of Group A samples with polymer/mineral composites

Using the procedure outlined in Section 4.20.2, Group A samples that had been sintered to 1100°C were infiltrated with a range of Derakane 411-3350 Epoxy Vinyl Ester Resin[®] and mineral composites.

Uninfiltrated samples were initially infiltrated under vacuum without alteration, with the result that as the weight of mineral mixed with Derakane increased, so too did resultant batch viscosity, until a point was reached that was different for each of the composites, where infiltration was impeded and became uneven. Samples were drilled using a 2mm diameter bit to provide three access channels for the composite, two transverse, one longitudinal. Figure 6.11 shows the relative positions of the three access channels, with the two transverse channels each intersecting the central longitudinal channel.

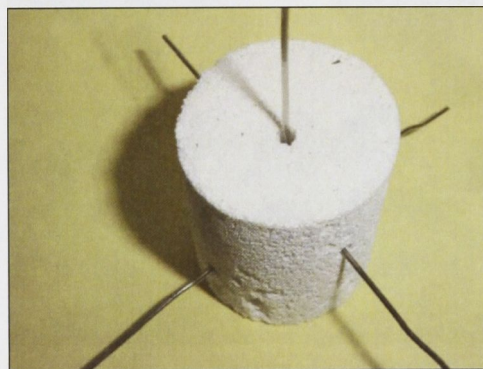


Figure 6.11: Group A sample, 1100°C, showing transverse and longitudinal access points prior to vacuum infiltration

Testing of vacuum infiltration of samples configured with three access channels, sectioning and subsequent SEM of their polished faces showed that penetration of the visible void fractions by the Derakane mineral composite both in close proximity to the drilled holes and at mid points between the three holes did not show observable differences in the distribution of particles within the Derakane matrix. All subsequent infiltration with the Derakane mineral composites under vacuum were performed using standard samples with access channels drilled in the same planes and aspects.

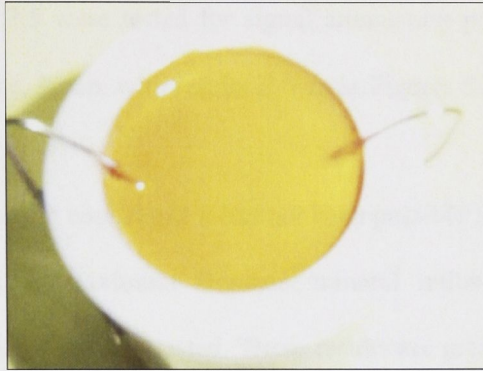


Figure 6.12: Group A sample, 1100°C, showing a hardened upper surface after vacuum infiltration with Derakane 411-3350 Epoxy Vinyl Ester Resin and yellow lead, 1:2.5

After vacuum infiltration and hardening the Derakane/yellow lead composite is seen in Figure 6.12, above, prior to removal.

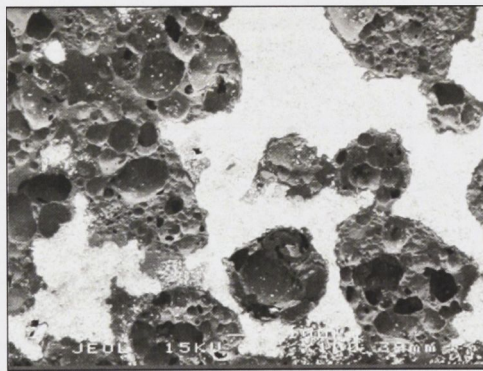


Figure 6.13: Electron micrograph of a Group A structure, 1100°C infiltrated with Derakane/yellow lead composite 1:2.5, x80

Figure 6.13, above, shows a section of a Group A sample after infiltration with a Derakane/yellow lead composite, 1:2.5, where cenosphere particles are seen amidst aggregated white particles of lead. Sawing has removed some of the larger cenosphere structural elements that are seen as approximately hemispherical cavities. Particles also show infiltration of interior cavities where the Derakane fraction contains few, if any lead particles. 50µm thick sawn samples of the structure infiltrated with Derakane/lead

composite 1:1.5 and 1:2.5 were tested for signal attenuation properties at the Tsukuba Photon Factory beamline, Japan, with results shown as Figures 5.21 and 5.22.

Because of time and costing constraints it has not been possible for us to determine either appropriate viscosities or maximum Derakane/mineral ratios for the full range of element-source composites initially tested. These results are presented as indicative, and not definitive. Samples infiltrated with Derakane/mineral composites were not tested for any properties other than signal attenuation.

Table 6.1: Comparison of specific compressive strength of materials

Material	Density, ρ [g/cm ³]	Compressive strength, σ_c [MPa]	Specific compressive strength, σ_c/ρ
Sintered ceramic	~0.5	15	30
Bone	0.05-0.7	19	270
Wood Parallel to grain Perpendicular to grain	0.37-0.65	38-49 3.4-5.4	78 8.3
Cork	~0.15	-	-
Concrete	2.4	40-130	33

Table 6.1 reports properties of four porous solids in addition to those of the sintered ceramic that is the subject of this thesis. From this comparison it is clear that natural porous structures, namely bone and wood, are superior to synthetic structures. Nevertheless, the sintered porous structure developed in this work has specific strength comparable to that of concrete.

Chapter 7 Conclusion

A new ceramic structure is described in this work and is characterised as a strong porous ceramic material in which porosity is predictably variable by composition and sintering. Its primary constituent is cenospheres, a form of fly ash and a by-product of the combustion of pulverized coal in the furnaces of electricity-generating power stations. The addition of powdered-ceramic materials creates the neck structure that allows individual cenospheres to be fused into a porous solid. The development of the sintered ceramic structure comprising multiple, readily available raw materials has been achieved.

In its basic, sintered form the structure is a low density ceramic [$\sim 500\text{kg/m}^3$], it is light-weight, strong [15 MPa], and permeable [0.1g/m.s]. It offers potential for use in association with high temperatures, up to 1400°C , it may be readily sawn and shaped and when infiltrated with a polymer and cured it may be machined to precise tolerances [$\sim 0.05\text{mm}$].

The sintered ceramic may be produced over a range of temperatures, $1100\text{-}1500^\circ\text{C}$, and in its uninfiltrated form may be further varied through

- a) choice of constituent-materials ratios
- b) choice of maximum sintering temperature within the range demonstrated

Because of its continuously articulated void fraction, during sintering the structure is not subject to the same average-hourly temperature-increase constraints as traditional, dense, fine-particle ceramic composites. It is proposed that the structure may be sintered very

Chapter 7 Conclusion

slowly, in conjunction with other composites requiring such a regimen, or alone and quickly at rates that would otherwise see the destruction of the same dense composites.

The structure is highly porous, strong and incorporates a void fraction that is articulated in three dimensions, the volume of which is predictable as a function of composition and maximum sintering temperature. The structure's properties may be varied to satisfy specific requirements, such as void-fraction volume, permeability, maximum strength and density, either through choice of constituent-materials ratios or maximum sintering temperature, or by the choice of variables from each.

*

References

- 1 Raask, E., (1968). Cenospheres in pulverised-fuel ash. *Journal of the Institute of Fuel* 11; 339
- 2 Hoy, H.R., Roberts, A.G., and Wilkins, D.M. (1962) Some investigation into the gasification of solid fuel in a slagging fixed-bed gasifier. Joint Conference of The Institution of Gas Engineers and The Institute of Fuel on gasification processes, Paper 5, pages 1-11. Institute of Fuel.
- 3 Ghosal, S., & Self, S.A., (1994). Particle size-density relation and cenosphere content of coal fly ash. *Fuel*. 74:522-529
- 4 Gentzis, T., & Chambers, A., 1993. A Microscopic Study of the combustion residues of subbituminous and bituminous coals from Alberta, Canada. *International Journal of Coal Geology*, 24:245-257
- 5 Georgakopoulos, A., Filippidis, A., and Kassoli-Fournaraki, A., (1994). Morphology and trace element contents of the fly ash from main and Northern lignite fields, Ptolemais, Greece. *Fuel*, 73:1802-1804
- 6 Kolay, P.K., & Singh, D.N., (2000). Physical, chemical mineralogical and thermal properties of cenospheres from an ash lagoon. *Cement and Concrete Research* 31 (4):539-542
- 7 Zheng, Y., & Wang, Z., (1996). Distribution and burning modes of char particles during combustion. *Fuel*, 75:434-1440
- 8 Gay, A.J., Littlejohn, R.F., and van Duin P.J., (1984). Studies of carbonaceous cenospheres from fluidised-bed combustors. *The Science of the Total Environment*, 36:239-246
- 9 Ozdemir, O., & Celik, M.S., (2002). Characterisation and recovery of lignitic fly ash byproducts from the Tuncbilek power station. *Canadian Metallurgical Quarterly* 41 (2):143-150
- 10 Wu, H-C., & Sun, P., (2005). New building materials from fly ash-based lightweight inorganic polymer. *Construction and Building Materials* 21 (1):211-217
- 11 Ayers, S.R., & Van Erp, G.M., (2003). Characterisation of new structural core materials based on vinyl ester and hollow ceramic microspheres. *Proceedings of the Institution of Mechanical Engineers Part L – Journal of Materials-Design and Applications* 217 (L3):211-228
- 12 Cardoso, R.J, Shukla, A., & Bose, A., (2002). The effect of particle size and surface treatment on constitutive properties of polyester-cenosphere composites. *Journal of Materials Science* 37 (3):603-613

References

- 13 Gupta, N., and Woldesenbet, e., (2003). Hygrothermal studies on syntactic foams and compressive strength determination. *Composite Structures* 61 (4):311-320
- 14 Souvignier, C.W., Sercombe, T.B., Huo, S.H., Calvert, P., & Schaffer, G.B., (2001). *Journal of Materials Research* 16 (9): 2613-2618
- 15 Rohatgi, P.K., Kim, J.K., Gupta, N., Alaraj, S., & Daoud, A., (2006). Compressive characteristics of A356/fly ash cenosphere composites synthesised by pressure infiltration technique. *Composites Part A: Applied Science and Manufacturing* 37 (3):430-437
- 16 Ozcivici, E., & Singh, R., (2005). Fabrication and characterisation of ceramic foams based on silicon carbide matrix and hollow alumino-silicate spheres. *Journal of the American Ceramic Society* 88 (12):3338-3345. doi: 10.1111/j.1551-2916.2005.00612.x
- 17 Anshits, A.G., Anshits, N.N., & Deribas, A.A., (2005) Detonation velocity of emulsion explosives containing cenospheres. *Combustion, Explosion and Shock Waves*, 41 (5) 591-598
- 18 Montgomery, D., & Diamond, S., (1984). The influence of fly ash cenospheres on the details of cracking in flyash-bearing cement pastes. *Cement and Concrete Research*, 14:767-775
- 19 Tiwari, V., Shukla, A., & Bose, A., (2004). Acoustic properties of cenosphere reinforced cement and asphalt concrete. *Applied Acoustics* 65 (3):263-275
- 20 Vasil'eva, N.G., Anshits, N.N., Sharonova, O.M., Burdin, M.V., & Anshits, A.G., (2005). Immobilisation of cesium and strontium radionuclides in framework aluminosilicates with the use of porous glass-ceramic matrices on coal fly ash cenospheres. *Glass Physics and Chemistry* 31 (5):637-647
- 21 Shukla. S., Seal, S., Rahaman, Z., & Scammon, K., (2001). Electroless copper coating of cenospheres using silver nitrate activator. *Materials Letters* 57 (1):151-156
- 22 Tsoungui, O., Vallet, D., & Charmet, J-C., (1998). Use of contact area trace to study the force distribution inside 2D granular systems. *Granular Matter* 1: 65-69
- 23 He, D., and Ekere, N.N., (2001). Structure simulation of concentrated suspensions of hard spherical particles. *AIChE Journal* 47 1: 53-59
- 24 Lu, G., Lu, G.Q., & Xiao, Z.M., (1999). Mechanical properties of porous Materials. *Journal of Porous materials* 6: 359-368
- 25 Krasulin, Yu.L., Timofeev, V.N., Barinov, S.M., Ivanov, A.B., (1980). Strength and fracture of porous ceramic sintered from spherical particles. *Journal of Materials Science* 15: 1402-1406

Bibliography

- Acquaviva, S. J., and Borty, S. A., *Structural Ceramics and testing of Brittle Materials*, Gordon & Breach Science Publishers (1968)
- Andreev, G. E., *Brittle Failure of Rock Materials: Test Results and Constitutive Models*, A. A. Balkema (1995)
- Ashby, M. F., and Jones D. R. H., *Engineering Materials 1* Pergamom Press (1993)
- Ashby, M. F., and Jones D. R. H., *Engineering Materials 2: An Introduction to Microstructures, Processing and Design*, Pergamom Press (1986)
- Bradt, R. C., Hasselman, D. P. H. and Lange, F. F., (Eds) *Fracture Mechanics of Ceramics: Vol 4, Crack Growth and Microstructures*, Plenum Press (1978)
- Brandt, A. M., *Cement-based Composites: Materials, Mechanical properties and Performance*, E. & F. N. Spon (1975)
- Brindley, G. W., and Brown, G., *Crystal Structures of Clay Minerals and the X-Ray Identification*, Mineralogical Society Monograph No 5, London
- Brontman, L. J., and Krock, R J., (Eds) *Modern Composite Materials*, Addison-Wesley Publishing Company (1967)
- Chalmers, B., *Principals of Solidification*, Robert E. Kreiger Publishing Company (1982)
- Clarke, A. B., and Disney R. L., *Probability and Random Processes*, John Wiley & Sons (1985)
- Davidge, R. W., *Mechanical Behaviour of Materials*, Cambridge University Press, (1979)
- Flynn, A. J., M.A. Thesis, *Structure/Property Relationships in Three Stoneware-clay Bodies*, (2000) Australian National University
- Grimshaw, R. W., *The Chemistry and Physics of Clays and other Ceramic Materials* Wiley Interscience, John Wiley & Sons (1971)
- Hayden, H. W., Moffatt, W. G., and Wulff, J., *The structures and Properties of Material, Vol III: Mechanical Behaviour*, John Wiley & Sons (1965)
- Jumikis, A. R., *Rock Mechanics*, Trans Tech Publications (1979)
- Henning, H-K., and Storr, M., *Electron Micrographs (TEM, SEM) of Clays and Clay Minerals*, Schriftenreihe fur Geologische Wissenschaften, Akademie-Verlag, Berlin, (1986)

Bibliography

- Lawrence, G. W., *Ceramic Science for the Potter*, Chilton Book Company (1972)
- Matsuo, S., and Inoue, G. Crisp, J. (Ed) *The Strength, Fracture and Fatigue of Materials*, P Nordhoff (1964)
- Nemecz, E., (Trans. B Balkay) *Clay Minerals*, Akademia Kiado, Budapest
- Singer, F., and Singer, S. S., *Industrial Ceramics*, Chapman and Hall (1971)
- Van Vlack, L. H., *Elements of Materials Science*, Addison-Wesley Publishing Company (1964)
- Van Vlack, L. H., *Physical Ceramics for Engineers*, Addison-Wesley Publishing Company (1964)
- Wilson, M. J., (Ed), *A Handbook of Determinative Methods in Clay Mineralogy*, Blackie, Glasgow (1987)
- Wyatt, O. H., and Dew-Hughes, D., *Metals, Ceramics and Polymers*, Cambridge University Press (1974)

Appendix

- 1 ACAA: Coal Combustion Products, information sheet
- 2 Envirospheres Pty Ltd, E-sphere specifications
- 3 Envirospheres Pty Ltd, Materials data sheet
- 4 Particle Surface Sciences, Eckalite kaolin #1, particle-size analysis
- 5 Imerys Minerals Australia Pty Ltd, Eckalite 1, 2, and 120, data sheet
- 6 Particle Surface Sciences, Frit 4194, particle-size analysis
- 7 Walker Ceramics, Frits analysis chart
- 8 Micro Silica Pty Ltd, Silica fume specifications
- 9 Particle Surface Sciences, Silica fume, particle-size analysis
- 10 Identification of samples, record sheet, page 24
- 11 ANSTO information: Scanning Laser Dilatometer, technical details
- 12 Firing cycle record, ANSTO, Lucas Heights, Laboratory Book record
- 13 SLD021209, plot of firing log, Laser Dilatometer Furnace, Materials Division, ANSTO
- 14 Ashland Inc, Derakane 411-1350 Epoxy Vinyl Ester Resin
- 15 Microstructure and properties of stoneware clay bodies, Flynn & Stachurski



Coal Combustion Products

Coal-burning powerplants, which supply more than half of U.S. electricity, also generate coal combustion products, which can be both a resource and a disposal problem. The U.S. Geological Survey collaborates with the American Coal Ash Association in preparing its annual report on coal combustion products (Kalyoncu, 2000). This Fact Sheet answers questions about present and potential uses of coal combustion products.

What are coal combustion products?

Coal combustion products (CCP's) are the inorganic residues that remain after pulverized coal is burned. Coarse particles (bottom ash and boiler slag) settle to the bottom of the combustion chamber, and the fine portion (fly ash, fig. 1) is removed from the flue gas by electrostatic precipitators or other gas-scrubbing systems.

Because of concerns about air quality and acid rain, the U.S. Congress passed the Clean Air Act Amendments of 1990 (Public Law 101-549), which included stringent restrictions on sulfur

oxide emissions. Most electric utilities in the Eastern and Midwestern States use bituminous coal having high sulfur contents of 2–3.5 percent. In order to meet the emission standards, many utilities have installed flue-gas-desulfurization (FGD) equipment. The FGD products are included in coal combustion products. The components of CCP's are as follows: fly ash, 57 percent; FGD products, 24 percent; bottom ash, 16 percent; and boiler slag, 3 percent.

What is flue gas desulfurization?

Flue gas desulfurization is a chemical process to remove sulfur oxides from the flue gas at coal-burning powerplants. Many FGD methods have been developed to varying stages of applicability (Radian Corp., 1983). Their goal is to chemically combine the sulfur gases released in coal combustion by reacting them with a sorbent, such as limestone (calcium carbonate, CaCO_3), lime (calcium oxide, CaO), or ammonia (NH_3). Of the FGD systems in the United States, 90 percent use limestone or lime as the sorbent (fig. 2). As the flue gas

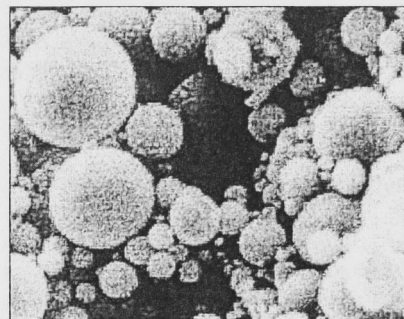


Figure 1. Fly ash from powerplants contains tiny ceramic spheres, typically ranging in diameter from 5 to 75 micrometers, which are called cenospheres; they have many uses. Scanning electron photomicrograph from the American Coal Ash Association.

comes in contact with the slurry of calcium salts, sulfur dioxide (SO_2) reacts with the calcium to form hydrous calcium sulfate ($\text{CaSO}_4 \cdot 2\text{H}_2\text{O}$, gypsum).

What quantities of CCP's are generated?

About 100 million metric tons (Mt) of CCP's are generated annually by U.S. coal-burning electric utilities.

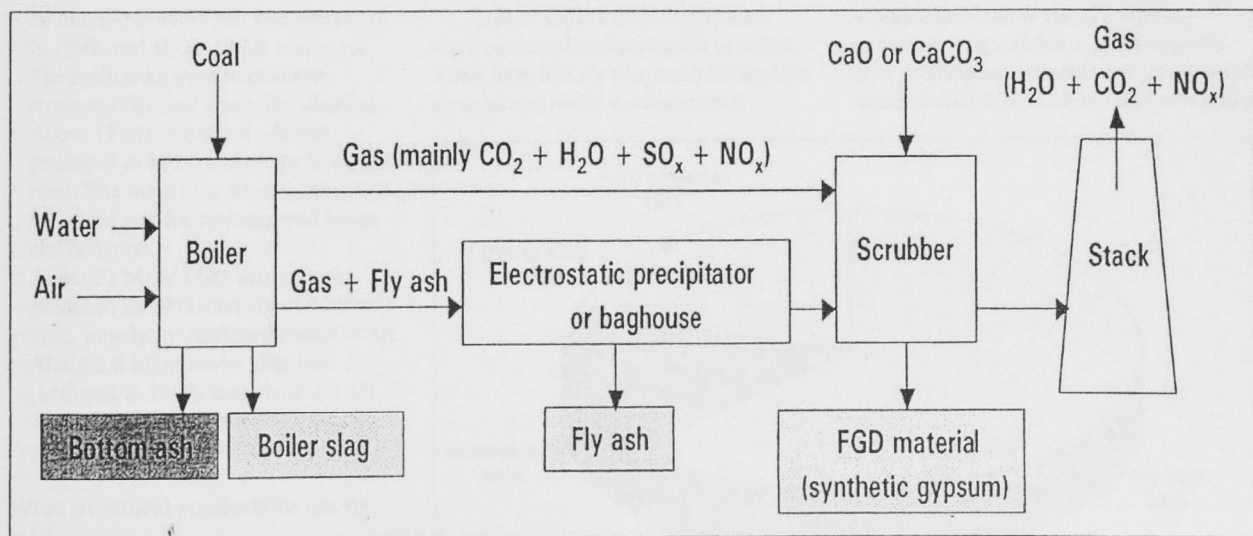


Figure 2. Flow diagram of the flue-gas-desulfurization process based on lime (CaO) or limestone (CaCO_3), which are the sorbents used by 90 percent of FGD systems in the United States.

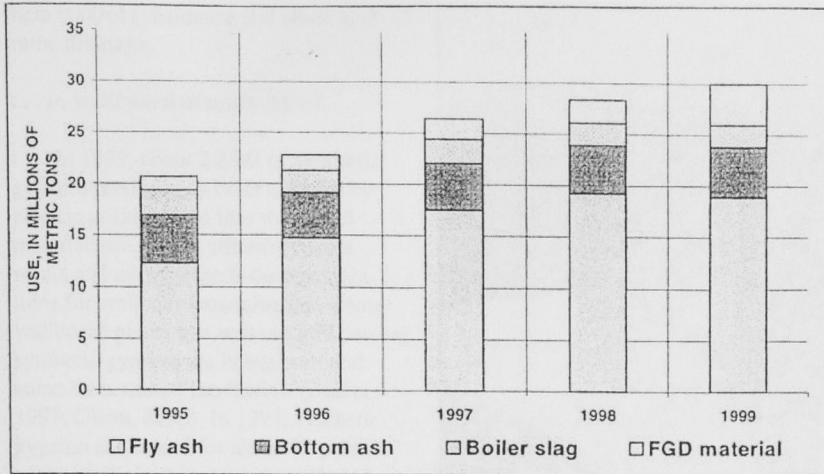


Figure 3. Amounts of coal combustion products used in the United States, 1995-99. Data from the American Coal Ash Association.

What are the uses for CCP's?

In the United States in 1999, approximately 30 percent of CCP's were used rather than discarded. The use of CCP's has increased over the years and reached 30 Mt in 1999 (fig. 3). Fly ash is the most used CCP; in 1999, it made up about 64 percent of the total CCP's used (fig. 4). CCP's are used, in decreasing tonnage, in cement and concrete, structural fill, road bases, agriculture, and other applications. Components of CCP's have different chemical and physical properties that make them suitable for different applications (Kalyoncu, 2000):

- About 57 Mt of fly ash was produced in 1999, and about 19 Mt was used. The main uses were in concrete, structural fill, and waste stabilization.
- About 15 Mt of bottom ash was produced in 1999, and about 5 Mt was used. The main uses were in structural fill, snow and ice control, road bases, and concrete.
- About 22 Mt of FGD material was produced in 1999, and about 4 Mt was used, mostly in wallboard manufacture.
- About 2.6 Mt of boiler slag was produced in 1999, and about 2.1 Mt was used, predominantly in blasting grit and roofing applications.

What structural applications use fly ash?

Fly ash is added to cement and concrete and is used in many large-scale construction projects. Fly ash is a vital

component in high-strength concrete in buildings that grace the skylines of major U.S. cities. Fly ash concrete is used in the decks and piers of many highway bridges. Concrete pavements containing fly ash are very durable and cost effective. Between 1950 and 1970, concrete with fly ash contents as high as 50 percent was used in an estimated 100 major dam construction projects. In the construction of Hungry Horse Dam in 1953, for example, 120,000 metric tons of fly ash were used (fig. 5).

What are the benefits of using CCP's in all applications?

Use of CCP's offers significant environmental and economic benefits. Their long history of successful applications attests to the environmental

acceptability of CCP's. When CCP's are used, natural resources can last longer and mining costs can be reduced. In 1999, the productive use of 30 Mt of CCP's saved \$620 million in disposal costs and about 350 acres of landfill space and generated \$150 million in sales, bringing total benefits to \$770 million.

... in cement and concrete?

The largest use of CCP's (mostly fly ash) is in cement and concrete. The CCP's displace portland cement and significantly reduce emissions of carbon dioxide (CO₂), a greenhouse gas that may be associated with global warming. Portland cement manufacture requires the burning of fossil fuels and decomposition of carbonates, which release large amounts of carbon dioxide into the atmosphere. Use of CCP's can potentially reduce carbon dioxide emissions by 10-14 Mt annually. In 1998, 10.5 Mt of fly ash was used in cement and concrete, replacing 7 Mt of portland cement and thereby reducing carbon dioxide emissions by 7 Mt.

... in mine reclamation?

Large cavities left by underground mining make the ground susceptible to subsidence. Acid water draining from some underground mines reaches surface streams and lowers the pH, causing serious ecological damage. Demonstration projects have shown that injection of alkaline CCP's into abandoned mines can

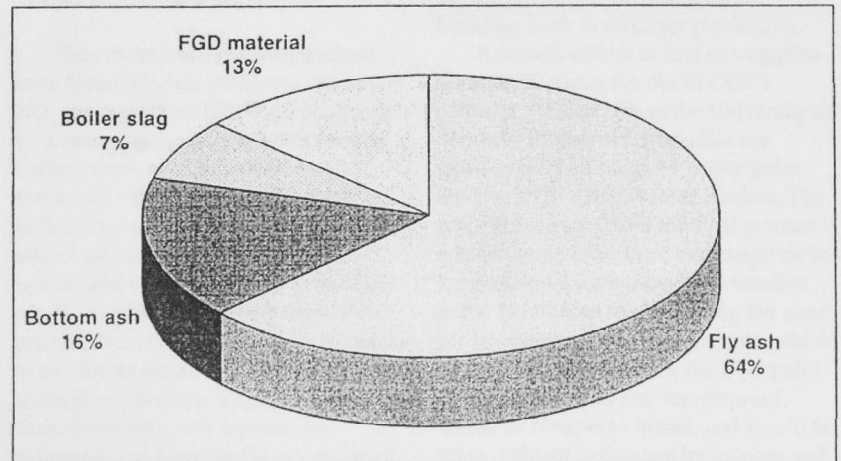


Figure 4. Coal combustion product use by type in the United States, 1999. Data from the American Coal Ash Association.

help control subsidence and abate acid mine drainage.

... in wallboard manufacture?

In 1999, about 2.8 Mt of synthetic gypsum produced as FGD material by electric utilities went into wallboard manufacture. The synthetic gypsum meets and often exceeds the specifications for wallboard manufacture. Some wallboard plants that will use 100 percent synthetic gypsum are being built and some have started production (Drake, 1997; Olson, 2000). In 1999, synthetic gypsum accounted for about 17 percent of the total gypsum used in wallboard manufacture, and this figure is expected to increase.

How can cenospheres in fly ash be used?

Fly ash contains tiny, hollow, particulate ceramic spheres, typically ranging in diameter from 5 to 75 micrometers, which are called cenospheres (fig. 1). They exhibit some unique properties, such as high energy absorption, which results in protection against electromagnetic interference. They are used as fillers in composite materials, in insulations, and in paints. A potential application of cenospheres is as heat-reflecting coatings for rooftops. Widespread use of such coatings could lower average city temperatures in summer and reduce the need for air conditioning.

How can ammonium sulfate FGD's be used in agriculture?

A flue-gas-desulfurization method popular in Europe uses ammonia (NH_3) as the sorbent; the FGD product is ammonium sulfate ($(\text{NH}_4)_2\text{SO}_4$). Sulfate is the preferred form of sulfur readily assimilated by crops, and ammonium sulfate is the ideal sulfate compound for soil supplements because it also provides nitrogen from the ammonium. The use of ammonium sulfate in large-scale fertilizer formulations has been growing gradually. This growth provides a market for FGD products and could make FGD processes based on ammonia attractive alternatives to the processes based on lime and limestone.

The estimated worldwide annual shortage of almost 11 Mt of elemental

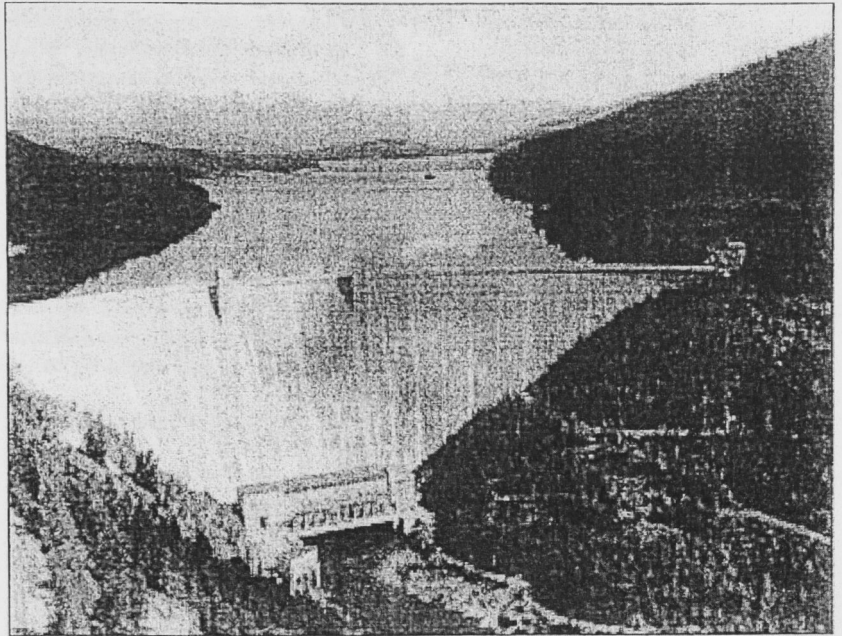


Figure 5. Hungry Horse Dam, Montana, is a thick-arch structure that was built between 1948 and 1953 with concrete containing 120,000 metric tons of fly ash. The use of coal fly ash in cement and concrete displaces portland cement. Photograph from the U.S. Bureau of Reclamation.

sulfur for agricultural applications could be supplied by 45 Mt of ammonium sulfate (Ellison, 1999). This much FGD product could result from 170,000 megawatt-hours (MWh) of electricity production if plants burned coal containing 2.5–3 percent sulfur. A relatively large powerplant generates 1,000 MWh of electricity per year. Thus, 170 large powerplants burning high-sulfur coal and using FGD methods based on ammonia could produce the amount of ammonium sulfate needed for proper plant nutrition.

What research is being done?

Recent environmental regulations have forced electric utilities to use low- NO_x burners (“low- NO_x ” is a designation for burners that greatly reduce nitrogen oxide emissions). These burners leave some coal unburned, which leads to higher free carbon contents in fly ash and makes the ash unsuitable for use in cement and concrete applications. Many powerplants that previously could earn revenue from selling the fly ash have had to pay for its disposal. However, a novel technology, developed at Pennsylvania State University, can separate the unburned coal from the fly ash and may soon eliminate this problem. Moreover, the coal from the separation process is

activated under steam at 850°C and can be used in water and gas purification.

Utilities will continue to look for pollution-prevention technologies that will yield smaller quantities of FGD products that will be purer and have higher value than those presently produced. An example is the Basin Electric Cooperative’s Dakota Gasification plant in Beulah, N. Dak., where a wet ammonia-based FGD process is used for SO_2 removal in combustion of otherwise unsalable fuels derived from gasification of lignite. The resulting ammonium sulfate is sold and used as a sulfur blending stock in fertilizer production.

Research efforts to find new applications and increase the use of CCP’s continue. Researchers at the University of Southern Illinois at Carbondale are working on the design for utility poles made of CCP’s and organic binders. The researchers expect that the final product will be comparable to or even superior to the traditional creosote-coated wooden poles. In addition to eliminating the need for weatherproofing with creosote, which pollutes rainwater runoff, the CCP poles would be fireproof and termiteproof, would be cheaper to install, and would be more resistant to damage by humans and animals. It is estimated that 250,000 poles averaging 30–40 feet (9–12 meters)

in height and another million poles 15–30 feet (4.5–9 meters) in height are used annually in the Midwestern United States alone. Replacing wooden poles with CCP poles could double the use of fly ash while sparing millions of trees annually.

What are the barriers to CCP use?

There are many technical, economic, regulatory, and institutional barriers to increased use of CCP's. A lack of standards and guidelines for specific applications heads the list of technical barriers. Transportation costs lead the economic barriers, which limit the shipment of CCP's to within about a 50-mile (80-kilometer) radius of the powerplants.

The industry's ability to recycle CCP's may be limited by more restrictive environmental controls. In April 2000, the U.S. Environmental Protection Agency (EPA) stated that the use of CCP's does not warrant regulatory oversight but left the door open to stricter regulation of CCP's in the future. A few weeks later, the EPA nearly issued a ruling that would have classified CCP's as hazardous wastes under the Resource Conservation and Recovery Act (RCRA). In May 2000, the EPA reaffirmed its position that CCP's are nonhazardous.

Environmental regulation may also lead to the generation of lower quality, less usable CCP's. As mentioned above, the required use of low-NO_x burners has resulted in fly ash having an unburned coal content that makes it unsuitable for concrete; until new technologies are applied, this fly ash must be used in other products or disposed of.

Other barriers to CCP use are the RCRA designation of CCP's as solid wastes, regardless of their composition,

even when they are used as resources rather than disposed of; the lack of governmental incentive; and the lack of education among the user groups (engineers, contractors, and regulators).

With industry and government cooperation, steps toward increasing CCP use can include (1) establishing a research and development infrastructure to address the technical barriers to CCP use and to design innovative FGD methods and (2) providing objective scientific information.

What is the bottom line?

Coal combustion products have many economic and environmentally safe uses. For example, in construction, a metric ton of fly ash used in cement and concrete can save the equivalent of a barrel of oil and can reduce carbon dioxide releases that may affect global warming. The use of CCP's saves landfill space. CCP's can replace clay, sand, limestone, gravel, and natural gypsum, thus preserving the Nation's natural resources and helping to save energy and other costs associated with mining.

References Cited

- Drake, Robert, 1997, Wallboard plants to use 100% synthetic gypsum: *Rock Products*, v. 100, no. 8, p. 7.
- Ellison, William, 1999, Update on major commercial advancements by ammonia FGD: *International Technical Conference on Coal Utilization and Fuel Systems*, 24th, Clearwater, Fla., March 8–11, 1999, Proceedings Preprint.
- Kalyoncu, R.S. [2000], Coal combustion products: U.S. Geological Survey *Minerals Yearbook 1999*, v. 1,

available online at <http://minerals.usgs.gov/minerals/pubs/commodity/coal/874499.pdf>.

Olson, D.W. [2000], Gypsum: U.S. Geological Survey *Minerals Yearbook 1999*, v. 1, available online at <http://minerals.usgs.gov/minerals/pubs/commodity/gypsum/320499.pdf>.

Radian Corporation, 1983, The evaluation and status of the flue gas desulfurization systems, Research Project 982–28: Austin, Tex., Final Report, 631 p.

For more information, please contact:

Rustu S. Kalyoncu
Coal Combustion Products
Commodity Specialist
U.S. Geological Survey
983 National Center
Reston, VA 20192
Telephone: (703) 648–7720
Fax: (703) 648–7722
E-mail: rkayonc@usgs.gov

Donald W. Olson
Gypsum Commodity Specialist
U.S. Geological Survey
983 National Center
Reston, VA 20192
Telephone: (703) 648–7721
Fax: (703) 648–7722
E-mail: dolson@usgs.gov
Web site:
<http://minerals.usgs.gov/minerals>

Executive Director
American Coal Ash Association
6940 South Kings Highway
Alexandria, VA 22310
Telephone: (703) 317–2400
Fax: (703) 317–2409
Web site: www.aaa-usa.org

E-SPHERES SPECIFICATIONS

GRADE – SL500

Microns	% Retained in Range (Typical)
Above 500	0 – 10
250 – 500	80 – 100
Below 250	0 - 10
Typical Physical Properties	
Bulk Density	0.32 – 0.42 g/cc
Relative Density	0.80 – 0.90 g/cc
Moisture Content (maximum)	0.3%
Floaters % by volume (mimimum)	96 %

NB Moisture level quoted is that at time of dispatch from factory. Moisture level may be subject to variation depending on atmospheric conditions at point of usage.

S-SL500.doc
Effective 01.04.2002

MATERIAL SAFETY DATA SHEET

Date of Issue: July 1999

PRODUCT NAME

E - SPHERES

Not classified as hazardous according to criteria of Worksafe Australia.

COMPANY DETAILS

Company Name: Enviropheres Pty Ltd (ACN 077 898 849)
Address: PO Box 497 Lindfield NSW 2070 Australia
Telephone, Fax: Telephone + 61 (0)2 9416 5644 Fax + 61 (0)2 9416 1718
E-mail: enviros@enviropheres.com.au

IDENTIFICATION

Product Name: E-SPHERES
Manufacturer's Product Code: SL Series, BL Series
UN Number: None allocated
DG Classification: None allocated
Hazchem Code: None allocated
Poisons Schedule Number: None allocated
Product Use: Lightweight inert filler

Physical Data and Other Properties

Appearance: SL Series: fine white powder, no odour. BL Series: fine grey/tan powder, no odour.
Specific Gravity: 0.6 - 0.8g/cc
Melting Point: 1600° - 1800°C
Boiling Point: N/A
Vapour Pressure: N/A

Flash Point: N/A
Flammability Limits: N/A
Solubility in Water: Insoluble

Ingredients

Hollow spheres of fused alumino silicate (CAS 68131-74-8) containing the following inseparable phases :

Chemical Name	CAS Number	Proportion
Amorphous alumino silicate	1327-36-2	65 - 80%
Mullite	1202-93-8	25 - 35%
Quartz	14808-60-7	0 - 1%
Calcite	1317-65-3	0 - 1%

HEALTH HAZARD INFORMATION

Acute Health Effects

Swallowed: If ingested in sufficient quantity may cause temporary gastric irritation.
Eye: Physical irritation. Abrasive action may cause damage to outer surface of the eye.
Skin: May cause irritation and inflammation due to defatting or mechanical action.
Inhalation: Irritation to nose, throat and upper respiratory tract.

Chronic Health Effects: None expected, refer Other Information

First Aid

- Swallowed:** Drink water do not induce vomiting.
Eye: Flush continuously with water for 15 minutes, Eyelids to be held open, do not rub eyes.
Skin: If skin becomes irritated remove clothing wash areas of contact with soap and water. Using a skin cream or lotion may be helpful in reducing irritation..
Inhalation: Remove exposed person to fresh air.

Advice to Doctor: Treat symptomatically for irritant effects.

PRECAUTIONS FOR USE

Exposure Standards: 10 mg/m³ Dust Not Otherwise Classified (inspirable dust) , (NOHSC 1995)
10 mg/m³ particulates Not Otherwise Classified (inhalable dust), (ACGIH)

Engineering Controls: Where possible use local exhaust ventilation.

Personal Protection Equipment:

Where overhead work is involved, goggles and head covering should be worn; and
A half-face (P1 or P2) respirator should be worn during work in poorly ventilated spaces, or where evidence suggests that inspirable dust levels may exceed 10 mg/m³.

All respiratory devices should be tested for compliance with AS/NZS 1715 & AS/NZS 1716 or local equivalent standard.

Flammability: Non flammable

SAFE HANDLING INFORMATION

Storage and Transport: Keep dry. No special storage or transport requirements.

Spills: Shovel up bulk, use vacuum cleaner to clean up residues.

Waste Disposal: Waste should be placed in containers, plastic bags or other methods which prevent dust emission, and disposed of in accordance with the local waste disposal authority requirements.

Fire/Explosion hazard: Not flammable and not explosive

OTHER INFORMATION

E-SPHERES consist of amorphous and poorly crystalline alumino silicates with a very low crystalline silica content. They are inert and do not leach detectable levels of heavy metals. In line with evidence from other naturally occurring non-fibrous alumino silicates, if dust exposures are kept below the exposure standard, no long term health or toxic effects such as pneumoconiosis or cancer are expected.

Reference: Replaces MSDS of September 1998.

CONTACT POINT

During Business Hours Telephone:
Emergency After Hours Contact:

Technical Manager (02) 9416 5644
Technical Manager (02) 9416 5644 voice mail

Eckhardt #1
Kardis

PsS Applications Laboratory

Saturn DigiSizer 5200 V1.06 Saturn DigiSizer 5200 V1.06 Serial Number 127 Page 1

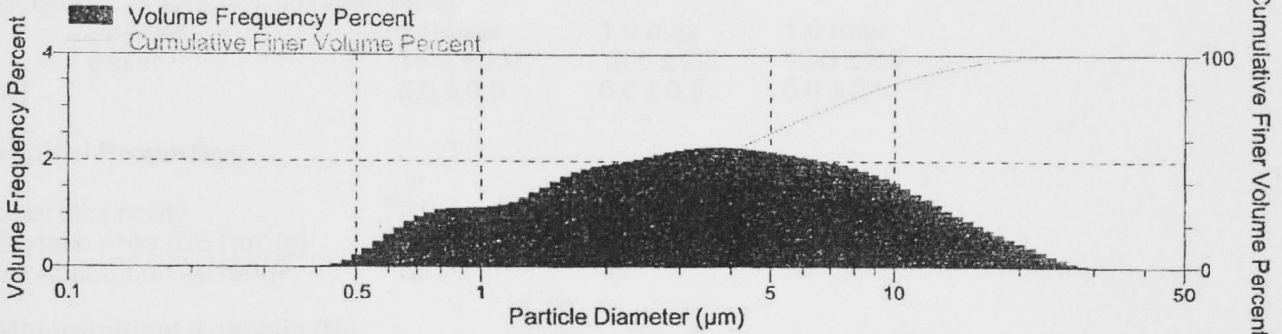
Sample: 494
 Operator: CM
 Submitter: ANU
 File: C:\5200\DATA\131\000-339.SMP

Test Number: Avg of 3
 Analyzed: 8/1/02 11:08:35AM
 Reported: 8/1/02 3:31:06PM
 Background: 8/1/02 10:18:48AM

Model: Fraunhofer, 1.331
 Material: Fraunhofer / Water
 Background: Water RI 1.331
 Smoothing: Medium

Combined Report

Volume Frequency vs. Diameter



Summary Report

Analysis Conditions

FlowRate: 12.0 l/m
 Circulation time: 120 sec

Ultrasonic intensity: Not Used
 Ultrasonic time: Not Used

Sample

Sample Concentration: 0.0116 %
 Obscuration: 18.1 %

Volume Distribution Arithmetic Statistics

	Std Dev of 3			Std Dev of 3	
Mean	5.091	0.035	Mode	3.774	0.217
Median	3.566	0.047	Std. Dev.	4.560	
Coef. Var.	0.896		Skewness	1.660	
Kurtosis	2.936				

Peaks

Peak Number	% of Dist.*	% of Dist. Std Dev of 3	Mean	Mean Std Dev of 3	Median	Median Std Dev of 3	Mode
1	100.0	0.0	5.091	0.035	3.566	0.047	3.774

* Peaks must comprise at least 5.00 % of the distribution.

ECKALITE 1, 2 and 120

ECKALITE 1, 2 and 120 are high quality water washed china clays with controlled colour and particle size distribution.

PHYSICAL PROPERTIES	ECKALITE 1	ECKALITE 2	ECKALITE 120
Brightness (ISO457nm)	84.0 ± 1.0	80.0 ± 1.0	80.0 ± 1.0
Wt% +53 Micron	0.05 max	0.05 max	1.0 max
Wt% +10 Micron	1.0 max	7.0 ± 2.0	20 (Typical)
Wt% -2 Micron	87.0 ± 3.0	73.0 ± 3.0	55 (Typical)
Moisture Content (Wt %) (when packed)			
- Powder	1.0 max	1.0 max	1.0 max
- Pellet	10.0 ± 2.0	10.0 ± 2.0	10.0 ± 2.0
pH	5.0 ± 0.5	5.0 ± 0.5	5.0 ± 0.5

Typical Properties

Specific gravity	2.6	2.6	2.6
Surface Area (BET;m ² /g)	18	16	13
Oil Absorption (g/100g)	50	45	44

Mineralogical Analysis (%)

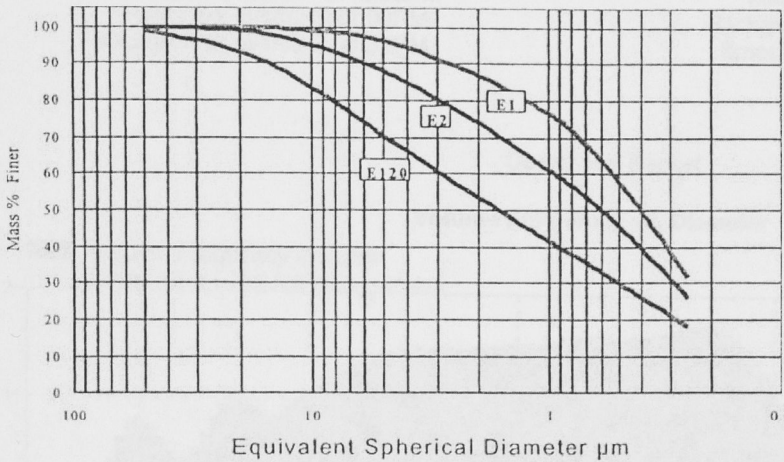
Kaolinite	99	98	94
Mica	1	1	2
Quartz	trace	1	4

CHEMICAL ANALYSIS (by X-ray Fluorescence) (%)

SiO ₂	46	47	49
Al ₂ O ₃	38	38	37
Fe ₂ O ₃	0.60	0.75	0.83
TiO ₂	0.70	0.80	0.72
CaO	0.05	0.05	0.05
MgO	0.07	0.08	0.08
K ₂ O	0.14	0.16	0.25
Na ₂ O	0.10	0.12	0.10
Loss on Ignition (1000°C)	14.0	13.7	13.0

ECKALITE 1, 2 and 120

Typical Particle Size Distribution



E1 = Eckalite 1 E2 = Eckalite 2 E120 = Eckalite 120

The data quoted are determined by use of Imerys Standard Test Methods, copies of which will be supplied upon request. Where maximum/minimum limits are indicated, this constitutes a specification. Where no maximum/minimum limits are given the data quoted are typical only. Every precaution is taken in production to ensure the goods conform to our published data, however, as the products are based on naturally occurring raw materials, Imerys Minerals Australia reserves the right to change these data should it become necessary. Unless stamped 'controlled' in red ink, the reader should check that the data contained herein is current.



Manufactured under a quality system certified as complying with ISO 9001 by an accredited certification body.

Imerys Minerals Australia Pty Ltd
 Glenelg Highway Pittong Linton Victoria 3360 Australia
 Telephone: (03) 5344 7205 Facsimile: (03) 5344 7308



File 495

PsS Applications Laboratory

Saturn DigiSizer 5200 V1.06 Saturn DigiSizer 5200 V1.06 Serial Number 127 Page 1

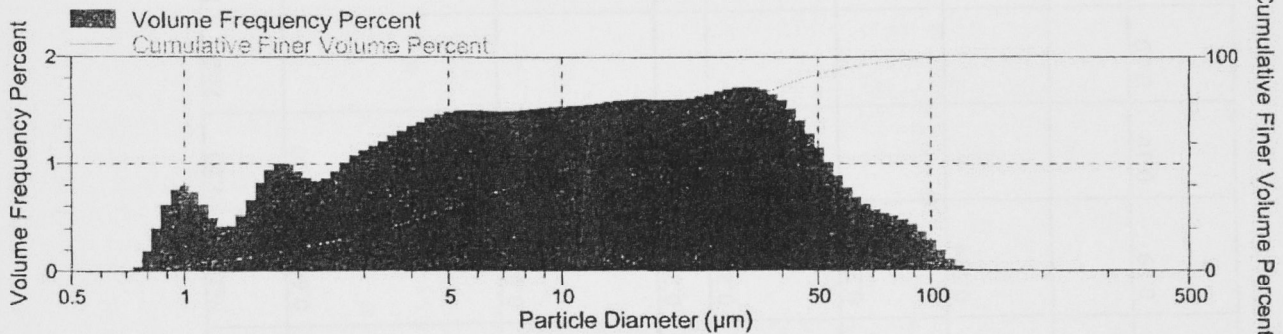
Sample: 495
 Operator: CM
 Submitter: ANU
 File: C:\5200\DATA\L131\000-340.SMP

Test Number: Avg of 3
 Analyzed: 8/1/02 12:12:32PM
 Reported: 8/1/02 3:31:09PM
 Background: 8/1/02 2:04:31PM

Model: Fraunhofer, 1.331
 Material: Fraunhofer / Water
 Background: Water RI 1.331
 Smoothing: Medium

Combined Report

Volume Frequency vs. Diameter



Summary Report

Analysis Conditions

FlowRate: 12.0 l/m Ultrasonic intensity: Not Used
 Circulation time: 120 sec Ultrasonic time: Not Used

Sample

Sample Concentration: 0.0297 %
 Obscuration: 13.9 %

Volume Distribution Arithmetic Statistics

	Mean	Std Dev of 3	Mode	Std Dev of 3
Mean	18.75	0.144	31.72	0.000
Median	11.05	0.056	20.09	
Coef. Var.	1.071		1.764	
Kurtosis	3.310			

Peaks

Peak Number	% of Dist.*	% of Dist. Std Dev of 3	Mean	Mean Std Dev of 3	Median	Median Std Dev of 3	Mode
1	5.2	0.3	1.031	0.017	1.018	0.012	1.003
2	7.8	0.1	1.813	0.018	1.804	0.017	1.784
3	25.0	0.9	4.434	0.070	4.322	0.045	5.870
4	28.6	1.9	12.57	0.054	12.06	0.021	16.84
5	33.3	0.8	41.54	0.772	35.89	0.799	31.72

* Peaks must comprise at least 5.00 % of the distribution.

FRITS ANALYSIS CHART

Frit No.	Description	MELTING TEMPERATURE	USES	CaO	Na2O	K2O	ZnO	BaO	PbO	Al2O3	SiO2	B2O3	ZrO2	Mol Wt
5301 4194	A High alkaline leadless frit. Useful for Raku glazes. Can be used for thermal expansion in small amounts without affecting the glaze adversely	900 - 1060 °C	Raku glazes	0.14	0.66	0.20				0.29	2.96	0.67	F2 0.40	329
3110 4110	Leadless, soft sodium borosilicate frit. High expansion	1000 -1060°C	Copper blue and manganese purple glazes. For crackles	0.29	0.61	0.07				0.02	2.86	0.09		280
4124 3124	Leadless, calcium borosilicate frit.	1040 -1100°C		0.68	0.29	0.04				0.16	2.58	0.54		266
4113 4712	Hard leadless clear borosilicate frit.	1040 -1100°C	General purpose for developing strong colours	0.60	0.27	0.13				0.35	3.50	0.63		353
3134 or 4508 4108	Lead free calcium borosilicate frit.	1040 -1100°C	Special effects: raku glazes	0.68	0.22					0.07	200	0.63		229
3271 4171	A Lead free calcium frit borosilicate frit	1040 -1100°C	Lead free calcium borosilicate frit	0.486	0.514						2.25	0.768		248
4064 3464	A standard low solubility 'lead bisilicate' frit.								1.00	0.085	1.95			349
938 3193	Clear, hard barium borosilicate leadless frit	1040-1100°C	Not for use over underglaze colours	0.51	0.19	0.10	0.10	0.10		0.20	2.86	0.62		308

Specification:

Silica Fume



Microsilica Pty Ltd

ACN 009 290 715

Source of Silica Fume

Condensed silica fume (CSF) is produced by filtering the off gasses from a silicon furnace. All silica fume supplied by Microsilica Pty Ltd is produced by Simcoa Operations Pty Ltd. at its silicon smelter located at Bunbury Western Australia.

This specification details the properties of each and indicates where they can be used.

International Standards

Internationally complies with CSA-A23.5-M86. Product supplied to Australia and New Zealand complies with AS3582.3 1994. A test certificate is issued with each order.

	Australian Standard 3582.3 1994	Canadian Standard A23.5-M86
<i>Batch Control Limits</i>		
LOI	<6%	<6%
Bag Weight	Yes	Yes
<i>Plant Control Limits</i>		
Plant Type		
SO ₃	<3%	<1%
SiO ₂	>85%	
Chloride Ion	Report	NA
Soundness Exp/Cont	NA	<0.2%
H ₂ O	<2%	<3%
Retained 45um	NA	<10%
Relative Density	Report	NA
Variation Avg Density	NA	<5%
Variation Avg Fineness	NA	<5%
Relative Strength (Accel Pozz. Index)	Report	>85%
Relative Water Req.	Report	NA
Bulk Density	Report	NA

Quality Assurance

Simcoa Operations Pty Ltd, the company responsible for quality assurance is accredited to quality standards AS3902 and ISO9002.

Chemical Data

99% Confidence Limits / Typical Levels

The data below represents the max or min values at a 99% confidence level. It is derived from the mean value + 3 standard deviations. The typical level is shown in the adjacent column.

	99% Confidence level	Typical Level
SiO ₂ min	90%	94%
Fe ₂ O ₃ max	0.2%	0.1%
Al ₂ O ₃ max	0.5%	0.2%
TiO ₂ max	0.1%	0.1%
Na ₂ O max	0.1%	0.1%
K ₂ O max	0.8%	0.3%
MgO max	0.7%	0.2%
SO ₃ max	0.1%	0.1%
CaO max	0.3%	0.3%
P ₂ O ₅ max	0.3%	0.1%
LOI max	6.0%	4.0%
Ph	-	-
m ² /g		22
Colour	Light grey	Light grey

PsS Applications Laboratory

Saturn DigiSizer 5200 V1.06 Saturn DigiSizer 5200 V1.06 Serial Number 108

Page 1

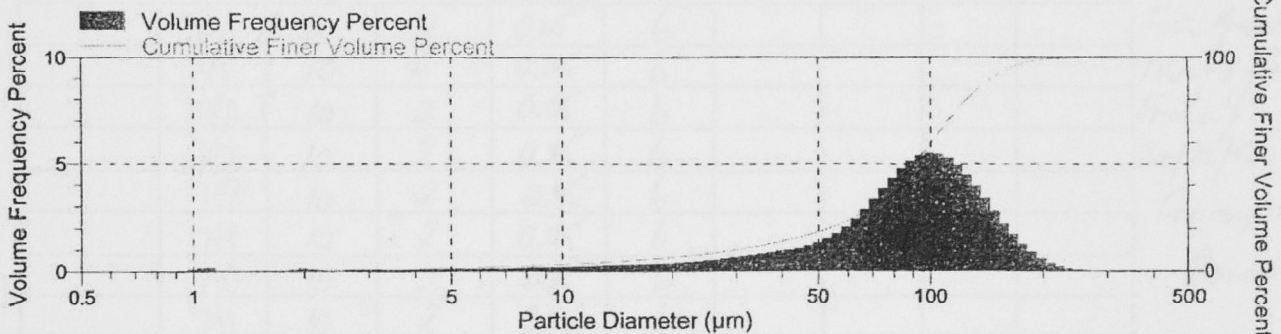
Sample: 545
 Operator: CM
 Submitter: ANU
 File: C:\5200\DATA\131\000-395.SMP

Test Number: Avg of 3
 Analyzed: 9/2/02 3:14:26PM
 Reported: 9/2/02 3:27:57PM
 Background: 9/2/02 3:02:25PM

Model: Fraunhofer, 1.331
 Material: Fraunhofer / Water
 Background: Water RI 1.331
 Smoothing: High

Combined Report

Volume Frequency vs. Diameter



Summary Report

Analysis Conditions

FlowRate: 12.0 l/m
 Circulation time: 120 sec

Ultrasonic intensity: Not Used
 Ultrasonic time: Not Used

Sample

Sample Concentration: 0.2175 %
 Obscuration: 16.4 %

Volume Distribution Arithmetic Statistics

	Std Dev of 3			Std Dev of 3	
Mean	90.24	0.899	Mode	99.70	0.000
Median	90.20	0.900	Std. Dev.	43.50	
Coef. Var.	0.482		Skewness	0.184	
Kurtosis	-0.039				

Peaks

Peak Number	% of Dist.*	% of Dist. Std Dev of 3	Mean	Mean Std Dev of 3	Median	Median Std Dev of 3	Mode
1	99.0	0.1	91.14	0.849	90.71	0.865	99.70

* Peaks must comprise at least 5.00 % of the distribution.

Record of tests

Date	No	Description							
		GROUP A	cont	Am210	Keelin	Water			
	774	82500	4194	2	0.35	6			
	775	10	2	0.35	6				For Am210
	776	10	2	0.35	6				1300 jing
	777	10	2	0.35	6				Tuesday
	778	10	2	0.35	6				12/12/02
	779	10	2	0.35	6				Group A
	780	10	2	0.35	6				Base
	781	10	2	0.35	6				
	782	10	2	0.35	6				
	783	10	2	0.35	6				
		82500	4194	Keelin	Water				
	784	10	2	0.35	6				For Am210
	785	10	2	0.35	6				1400/3 jing
	786	10	2	0.35	6				Friday
	787	10	2	0.35	6				22/12/02.
	788	10	2	0.35	6				Group A
	789	10	2	0.35	6				Base
	790	10	2	0.35	6				
	791	10	2	0.35	6				
	792	10	2	0.35	6				
	793	10	2	0.35	6				
		GROUP B.	Am210						
		82500	4194	Keelin	Water	SF	SN		11000'
	794	10	2	0.35	6	1.0	0.1		794-803
	795	10	2	0.35	6	0.9	0.2		804-813
	796	10	2	0.35	6	0.9	0.3		814-823
	797	10	2	0.35	6	0.7	0.4		824-833
	798	10	2	0.35	6	0.6	0.5		For Am210
	799	10	2	0.35	6	0.5	0.6		11000 jing
	800	10	2	0.35	6	0.4	0.7		Monday
	801	10	2	0.35	6	0.3	0.9		9/12/02
	802	10	2	0.35	6	0.2	0.9		Group B
	803	10	2	0.35	6	0.1	1.0		

Scanning Laser Dilatometer

This equipment has been developed at ANSTO for studying the densification behaviour of Synroc and other ceramic materials

The Scanning Laser Dilatometer can be used for:

- Measurement of thermal expansion coefficients of ceramics, metals and composites
- Monitoring of sintering shrinkage against time and temperature.
- Rate controlled sintering of powder compacts.

Advantages of this system:

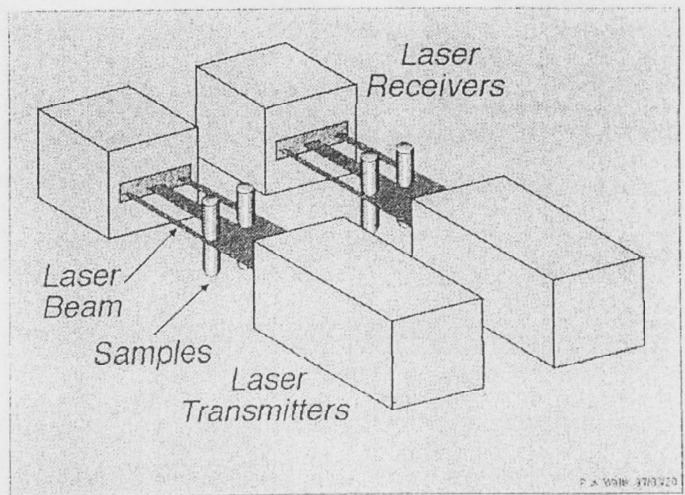
- Can monitor the dimensions of 8 samples simultaneously.
- Large samples and components up to 250mm can be monitored.
- Non-contact dimension measurement by laser (no push rods required).

The scanning laser dilatometer consists of three components:

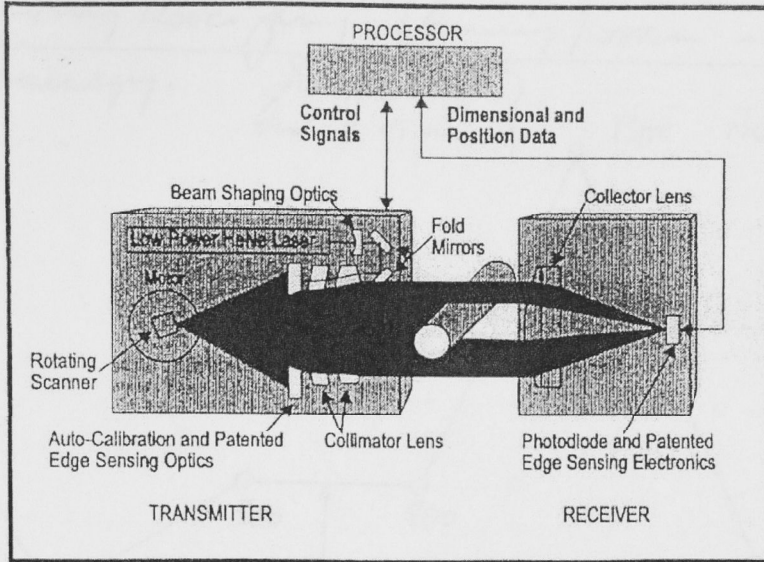
- **Air Furnace - (MODUTEMP, WA)** A silicon carbide element furnace with fibreboard insulation. Maximum operating temperature of 1550°C. Working zone of 400 x 400 x 400mm. Silica glass windows located in the doors on either side of the air furnace allow a scanning laser beam to be transmitted through and detected on the opposite side of the furnace.
- **Vacuum Furnace - (IONEX, USA)** A graphite element furnace with graphite fibreboard and grafoil insulation. Samples can be monitored in vacuum or in argon, nitrogen or special gas atmospheres. Working zone of 400 x 400 x 400mm.
- **Laser Dimension Sensors - (Z-Mike, USA)**

Samples placed within the scanning laser beam create shadows. The detector component of the laser sensors detect the shadows.

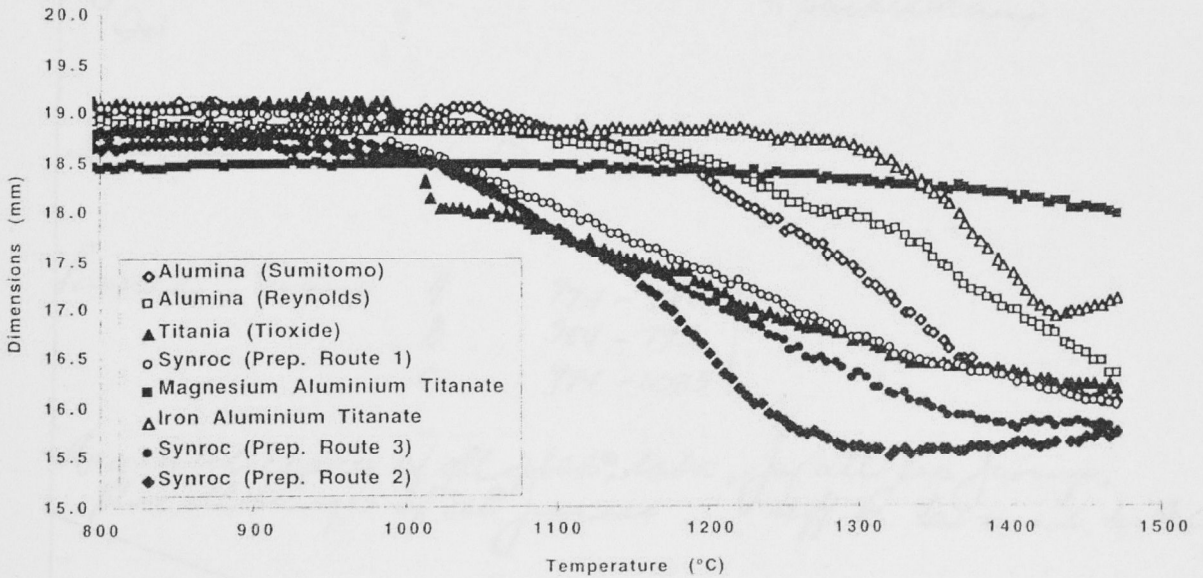
Dual sensors allow either; a single large sample (up to 250mm long) to be monitored; or, simultaneous monitoring of up to 8 samples.



Operating Principle of the Laser Scanners



Demonstration of the Laser Dilatometer's Ability to Monitor 8 Samples Simultaneously

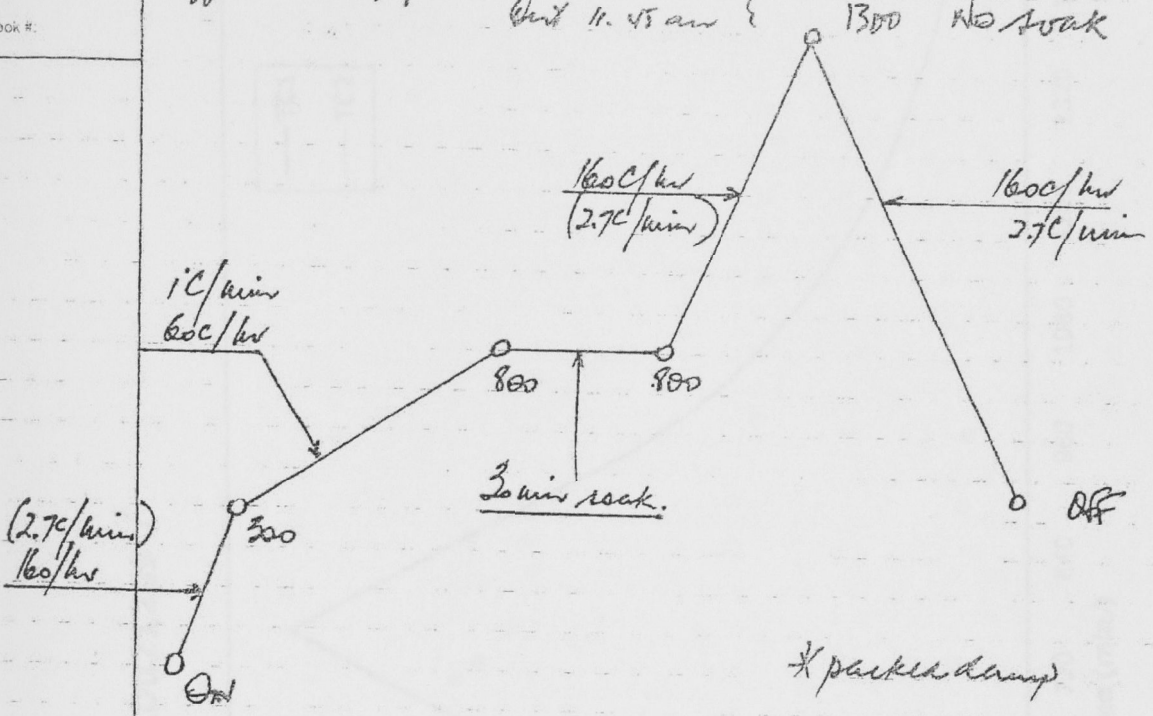


For further information on the Scanning Laser Dilatometer system please contact:

Dr Philip Walls
 Senior Research Scientist
 ANSTO Materials Division
 Tel: (02) 9717-9239
 Fax: (02) 9543-7179
 Email: paw@ansto.gov.au

Page 132
 Date 10/12/52
 Continued From
 Page #
 Book #

Title of Experiment
 Visit to AFSTO mechanical division. Parking firing for 1300C
 Unpacking 1200C firing. (burning 7.00am - 3.15pm)
 Jeff Kennedy. In 10.00am
 Out 11.45 am



Temp pack in 20/11/52

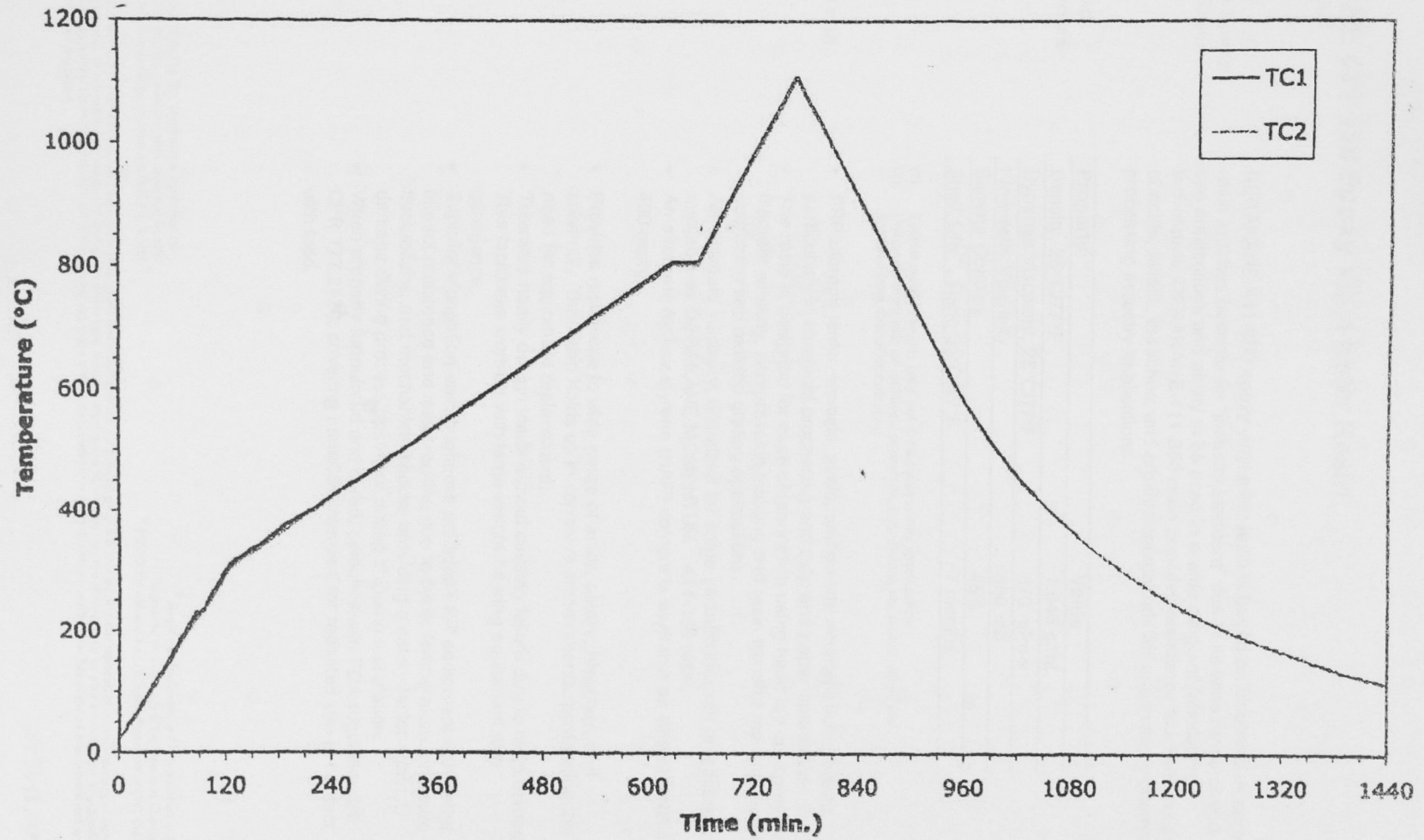
Packed Group

A	774 - 783
B	954 - 993
C	994 - 1033

Requested copies of all plots, data, for all 200 firing.
 plus all images of 200 furnace. Jeff K. to mail to Eng.

Continued on
 Page #
 Book #

SLD021209 ✓





DERAKANE 411-350 Epoxy Vinyl Ester Resin

November 2004

The Industry Standard for Epoxy Vinyl Ester Resin

DERAKANE 411-350 epoxy vinyl ester resin is based on bisphenol-A epoxy resin and has become an "industry standard" due to its wide range of end-use applications and ability to be used in a wide range of fabrication techniques. DERAKANE 411-350 resin provides resistance to a wide range of acids, alkalis, bleaches, and organic compounds for use in many chemical processing industry applications.

Typical Liquid Resin Properties

Property ⁽¹⁾	Value
Density, 25°C/77°F	1.046 g/mL
Dynamic Viscosity, 25°C/77°F	370 mPa·s
Kinematic Viscosity	350 cSt
Styrene Content	45%
Shelf Life ⁽²⁾ , Dark, 25°C/77°F	7 months

- (1) Typical property values only, not to be construed as specifications.
 (2) Unopened drum with no additives, promoters, accelerators, etc. added. Shelf life specified from date of manufacture.

Applications and Fabrication Techniques

- FRP storage tanks, vessels, ducts, and on-site maintenance projects, particularly in chemical processing and pulp and paper operations.
- The resin is designed for ease of fabrication using hand lay-up, spray-up, filament winding, compression molding and resin transfer molding techniques, pultrusion and molded grating applications.
- An alternate viscosity, optimized for some vacuum infusion processes, is available as DERAKANE MOMENTUM[™] 411-100 resin.
- An alternate for low styrene (HAP) content is available as DERAKANE 441-400 resin.

Benefits

- Provides resistance to wide range of acids, alkalis, bleaches, and solvents. This resin holds up in corrosive environments, postponing the need for equipment replacement.
- Tolerates heavy design loads without causing failure due to resin damage. This facilitates working with large weight-bearing equipment with confidence.
- Superior elongation and toughness provides FRP equipment with better impact resistance and less cracking due to cyclic temperature, pressure fluctuations, and mechanical shocks providing a safety factor against damage during process upsets or during shipping installation.
- When properly formulated and cured, complies with FDA regulation 21 CFR 177.2420, covering materials intended for repeated use in contact with food.



Ashland is committed to the continuous evolution of technology and service solutions that promote health, safety and environmental protection around the world.

[®] Registered trademark and [™] trademark of Ashland Inc.
^{*} Registered service mark of the American Chemistry Council
[©] 2002, 2004 Ashland Inc. All Rights Reserved. CWT-DS-314 Rev. 1

All statements, information and data presented herein are believed to be accurate and reliable but are not to be taken as a guarantee, express warranty or implied warranty of merchantability or fitness for a particular purpose, or representation, express or implied, for which seller assumes legal responsibility, and they are offered solely for your consideration, investigation and verification. Statements or suggestions concerning possible use of this product are made without representation or warranty that any such use is free of patent infringement and are not recommendations to infringe on any patent.

ASHLAND

Gel Time Formulations

The following table provides typical gel times for MEKP. "Starting point" formulations for MEKP, non-foaming MEKP alternatives, and BPO peroxides are available in separate product bulletins. These and other information are available at

MEKP Gel Time Table

Typical Gel Times⁽³⁾ Using NOROX⁽⁴⁾ MEKP-925H⁽⁵⁾ and Cobalt Napthenate-6%⁽⁶⁾

Temperature	15 +/-5 Minutes	30 +/-10 Minutes	60 +/-15 Minutes
15°C/59°F	1.5 phr ⁽⁷⁾ MEKP 0.30 phr CoNap6% 0.20 phr DMA	1.5 phr MEKP 0.30 phr CoNap6% 0.05 phr DMA	1.25 phr MEKP 0.30 phr CoNap6% 0.05 phr DMA 0.04 phr 2,4-P
20°C/68°F	1.5 phr MEKP 0.30 phr CoNap6% 0.10 phr DMA	1.5 phr MEKP 0.30 phr CoNap6% 0.05 phr DMA 0.03 phr 2,4-P	1.5 phr MEKP 0.30 phr CoNap6% 0.05 phr DMA 0.06 phr 2,4-P
25°C/77°F	1.25 phr MEKP 0.20 phr CoNap6% 0.05 phr DMA	1.25 phr MEKP 0.20 phr CoNap6% 0.02 phr 2,4-P	1.5 phr MEKP 0.20 phr CoNap6% 0.05 phr 2,4-P
30°C/86°F	1.0 phr MEKP 0.20 phr CoNap6% 0.02 phr DMA	1.25 phr MEKP 0.20 phr CoNap6% 0.04 phr 2,4-P	1.25 phr MEKP 0.20 phr CoNap6% 0.06 phr 2,4-P
35°C/95°F	1.0 phr MEKP 0.20 phr CoNap6% 0.02 phr 2,4-P	1.0 phr MEKP 0.20 phr CoNap6% 0.05 phr 2,4-P	1.0 phr MEKP 0.20 phr CoNap6% 0.08 phr 2,4-P

(3) Thoroughly test any other materials in your application before full-scale use. Gel times may vary due to the reactive nature of these products. Always test a small quantity before formulating large quantities.

(4) Registered trademark of Norac, Inc.

(5) Materials: NOROX MEKP-925H Methyleneethyleketone peroxide (MEKP) or equivalent low hydrogen peroxide content MEKP, Cobalt Napthenate-6% (CoNap6%), Dimethylamine (DMA), and 2,4-Pentanedione (2,4-P). Use of other MEKP or other additives may result in different gel time results.

(6) Use of cobalt octoate, especially in combination with 2,4-P can result in 20-30% slower gel times.

(7) Phr=parts per hundred resin molding compound

Casting Properties


Typical Properties⁽¹⁾ of Postcured⁽⁶⁾ Resin Clear Casting

Property	SI	US Standard	Test Method
Tensile Strength	86 MPa	12,000 psi	ASTM D-638/ISO 527
Tensile Modulus	3.2 GPa	4.6 x 10 ⁴ psi	ASTM D-638/ISO 527
Tensile Elongation, Yield	5-6%	5-6%	ASTM D-638/ISO 527
Flexural Strength	150 MPa	22,000 psi	ASTM D-790/ISO 178
Flexural Modulus	3.4 GPa	4.9 x 10 ⁴ psi	ASTM D-790/ISO 178
Density	1.14 g/cm ³		ASTM D-792/ISO 1183
Volume Shrinkage	7.8%	7.8%	
Heat Distortion Temperature ⁽⁹⁾	105°C	220°F	ASTM D-648 Method A/ISO 75
Glass Transition Temperature, Tg2	120°C	250°F	ASTM D-3419/ISO 11359-2
Barcol Hardness	35	35	ASTM D-2563/EN59

(1) Typical property values only, not to be construed as specifications. SI values reported to two significant figures; US standard values based on conversion.

(6) Cure schedule: 24 hours at room temperature; 2 hours at 120°C (250°F)

(9) Maximum stress: 1.8 MPa (264 psi)

 Ashland is committed to the continuous evolution of technology and service solutions that promote health, safety and environmental protection around the world.

® Registered trademark and ™ trademark of Ashland Inc.
* Registered service mark of the American Chemistry Council
© 2002, 2004 Ashland Inc. All Rights Reserved. - CWT-DS-344 Rev. 1

All statements, information and data presented herein are believed to be accurate and reliable but are not to be taken as a guarantee, express warranty or implied warranty of merchantability or fitness for a particular purpose, or representation, express or implied, for which seller assumes legal responsibility, and they are offered solely for your consideration, investigation and verification. Statements or suggestions concerning possible use of this product are made without representation or warranty that any such use is free of patent infringement and are not recommendations to infringe on any patent.

ASHLAND

Laminate Properties

Typical Properties⁽¹⁾ of Postcured⁽¹⁰⁾ 6 mm (1/4") Laminate⁽¹¹⁾

Property	SI	US Standard	Test Method
Tensile Strength	150 MPa	22,000 psi	ASTM D-3039/ISO 527
Tensile Modulus	12 GPa	1.7×10^6 psi	ASTM D-3039/ISO 527
Flexural Strength	210 MPa	30,000	ASTM D-790/ISO 178
Flexural Modulus	8.1 GPa	1.2×10^6 psi	ASTM D-790/ISO 178
Glass Content	40%	40%	ASTM D-2584/ISO 1172

(1) Typical property values only, not to be construed as specifications. SI values reported to two significant figures, US standard values based on conversion.

(10) Cure schedule: 24 hours at room temperature, 6 hours at 80°C (175°F)

(11) 6 mm (1/4") Construction - V/M/M²/Wr/M²/Wr/M

V = Continuous veil glass; M = Chopped strand mat, 450 g/m² (1.5 oz/ft²);

Wr = Woven roving, 500 g/m² (24 oz/yd²)

Safety and Handling
Consideration

This resin contains ingredients which could be harmful if mishandled. Contact with skin and eyes should be avoided and necessary protective equipment and clothing should be worn.

Ashland maintains Material Safety Data Sheets on all of its products. Material Safety Data Sheets contain health and safety information for your development of appropriate product handling procedures to protect your employees and customers.

Our Material Safety Data Sheets should be read and understood by all of your supervisory personnel and employees before using Ashland's products in your facilities.

Recommended Storage:

Drums - Store at temperatures below 27°C/80°F. Storage life decreases with increasing storage temperature. Avoid exposure to heat sources such as direct sunlight or steam pipes. To avoid contamination of product with water, do not store outdoors. Keep sealed to prevent moisture pick-up and monomer loss. Rotate stock.

Bulk - See Ashland's Bulk Storage and Handling Manual for Polyesters and Vinyl Esters. A copy of this may be obtained from Composite Polymers at 1.614.790.3333.



Ashland is committed to the continuous evolution of technology and service solutions that promote health, safety and environmental protection around the world.

® Registered trademark and 11 trademark of Ashland Inc.

* Registered service mark of the American Chemistry Council

© 2002, 2004 Ashland Inc. All Rights Reserved. CWT-DS-344 Rev. 1

All statements, information and data presented herein are believed to be accurate and reliable but are not to be taken as a guarantee, express warranty or implied warranty of merchantability or fitness for a particular purpose, or representation, express or implied, for which seller assumes legal responsibility, and they are offered solely for your consideration, investigation and verification. Statements or suggestions concerning possible use of this product are made without representation or warranty that any such use is free of patent infringement and are not recommendations to infringe on any patent.

ASHLAND

Microstructure and properties of stoneware clay bodies

A. J. FLYNN AND Z. H. STACHURSKI*

Department of Engineering, FEIT, Australian National University, Canberra, ACT0200, Australia

(Received 24 October 2005; revised 19 June 2006)

ABSTRACT: Raw clay materials manufactured for stoneware use are typically compounds of kaolins, silicas and feldspars. Two stoneware clay materials examined here were chosen because each is representative of the range of manufactured clay bodies. Samples were fired in an oxidizing atmosphere to a range of temperatures between ~1000 and 1300°C. Sample dimensions, density, porosity and mechanical properties under compression were measured as a function of firing temperature. Thin sections, showing particles and their relationship to pore/void structures, were prepared, recorded under scanning electron microscopy (SEM), and analysed. The observed changes in microstructure can be related to previously described metamorphic and micro-eutectic reactions and a gradual sintering process. Indications of changes to apparent porosity are further amplified by measured changes of mechanical properties. The modulus of elasticity increases with reduction in porosity to a point at which porosity ceases to be the principal determining factor. The critical Griffith's crack length, calculated from fracture-strength measurement, exhibits a similar trend. The onset of these changes coincides with a significant increase in sealed porosity and with the microstructural metamorphosis as revealed by SEM.

KEYWORDS: kaolin, silica, feldspar, porosity, microstructure, elastic modulus, compressive strength.

While extensive research has been conducted into industrial ceramics (i.e. high-temperature refractory or brick materials), there has been little, if any, examination of structure-property relationships in non-industrial clays. The implications for structure-property relationships of changes in composition, firing temperature and distribution of particles have hitherto been observed only on an empirical basis. In this study we report on experimental results and analysis, which allow the comparison of such data with those contained in the already extensive body of literature relating to industrial clay-based ceramic materials. Stoneware clay is a material of great complexity. It is manufactured by mixing (in a wet state) finely ground ingredients of kaolin,

feldspar and silica with or without various additives, to produce a 'body' possessing the property of plasticity in its wet state, and subsequently drying and heating to high temperatures (~1000–1300°C).

It appears from our experience and an exhaustive literature search that the relationship between the properties of fired stoneware clays and their microstructures, dictated by the distribution of particles sizes in raw materials, is to a large extent uncharted territory. In particular, we measured the various relevant properties that combine to affect final properties and inquired as to whether or not a point exists at which, or beyond which, optimal strength is achieved.

Our study shows some similarity to investigations carried out recently by Bauluz *et al.* (2004), in which mineralogical and textural changes produced in carbonated clays for brick making were reported.

* E-mail: zbigniew.stachurski@anu.edu.au
DOI: 10.1180/0009855064130218

The transformations that take place during the firing of raw materials determine the final properties of the ceramic products, and therefore an understanding of the microstructural changes is important in understanding structure-property relationship.

THEORETICAL BACKGROUND

Density and porosity

The volume of a ceramic body comprises solid substance, open voids (which are articulated and connected to the outside), and closed pores (sealed). Therefore, the volume of the body can be divided into three parts:

$$V_b = V_s + V_{op} + V_{sp} \quad (1)$$

where: V_b is defined by the external dimensions, V_s is the volume occupied by the solid substance only, V_{op} is the volume occupied by the open pores, and V_{sp} is the volume occupied by the sealed voids. Given the mass of the solid substance, m_s , the density of the body, ρ_b , is defined as:

$$\rho_b = \frac{m_s}{V_b} \quad (2)$$

and the density of the solid substance is defined as:

$$\rho_s = \frac{m_s}{V_s} \quad (3)$$

In general, $\rho_b < \rho_s$, if $(V_{op} + V_{sp}) > 0$, and $\rho_b = \rho_s$, if $(V_{op} + V_{sp}) = 0$. We define the following ratios as the volume fraction of the open pores, and that of the sealed pores, respectively:

$$v_{op} = \frac{V_{op}}{V_b} \quad (4)$$

$$v_{sp} = \frac{V_{sp}}{V_b} \quad (5)$$

From equations 1 to 5, the following relationship can be derived:

$$\frac{\rho_b}{\rho_s} + v_{op} + v_{sp} = 1 \quad (6)$$

Assuming that water can fill all of the open pore spaces, then the so-called apparent porosity of the ceramic body is defined as follows (Singer & Singer, 1971):

$$AP(\%) = \frac{\text{wet weight of sample} - \text{dry weight}}{\text{dry weight of sample}} \times 100 \quad (7)$$

where: 'dry weight' is the weight of sample without any water (moisture), and 'wet weight' is the weight of sample with open pores completely filled with water. The dry weight of the sample determines the mass of the solid substance, m_s . The increase in the weight of the wet sample is assumed to be due to water ingress through open pores. Since water content = v_{op} , then the volume fraction of open pores can be calculated from:

$$v_{op} \cong \rho_b * \frac{AP\%}{100} \quad (8)$$

If the solid density, body density, and open porosity are known, then from equation 6 the amount of sealed porosity can be predicted to be:

$$v_{sp} = 1 - v_{op} - \frac{\rho_b}{\rho_s} \quad (9)$$

If the solid substance is made up of a number of different constituents, then the mass of the solid is the sum of the masses of the individual constituents. The overall density of the solid, in the absence of chemical interactions, is predicted by the simple law of mixtures (Holliday, 1967):

$$\rho_s = \rho_1 v_1 + \rho_2 v_2 + \rho_3 v_3 + \dots + \rho_n v_n = \sum_{i=1}^n \rho_i v_i \quad (10)$$

where: $v_1, v_2, v_3 \dots v_n$, represent the volume fractions of the individual constituents respectively, and $\rho_1, \rho_2, \rho_3 \dots \rho_n$, are the corresponding densities.

Modulus of elasticity

The elastic modulus is a function of both matrix composition and porosity. To a first approximation, the dependence on composition can be predicted by a simple law of mixtures. Thus:

$$E = E_1 v_1 + E_2 v_2 + \dots + E_n v_n = \sum_{i=1}^n E_i v_i \quad (11)$$

where: $E_1, E_2 \dots E_n$ are the elastic moduli of individual components. If only two phases are considered, the first solid and the second is assumed to be void with zero elastic modulus, then the relationships for the porous body can be represented (Kunori & Geil, 1980) as:

$$\frac{E_b}{E_o} = \frac{1-p}{1+pk}, \text{ where } k = \left(\frac{8-10v}{7-5v} \right) \quad (12)$$

where: E_o is elastic modulus of the matrix without pores, E_b is elastic modulus of the body with pores,

p is total porosity, and ν is Poisson's ratio of the matrix. Different relationships for porous bodies were proposed by several authors (Helmuth & Turk, 1966; Sammis & Ashby, 1986; Brandt *et al.*, 1978). Specifically, Helmuth and Turk proposed:

$$\frac{E_b}{E_o} = (1 - p)^3 \quad (13)$$

A plot of E_b vs. $(1 - p)^3$ should extrapolate to the ultimate modulus, E_o , at $p = 0$. Similarly, from equation 12, a plot of E_b vs. $(1 - p)/(1 + pk)$ should also extrapolate to E_o at $p = 0$.

Compressive strength

The compression failure of brittle samples has been described by Kendall (1978), who showed that the compressive stress required to split a columnar specimen containing a vertical crack is given by:

$$\sigma_{\text{split}} = \frac{\sqrt{2/3}}{(1 - w/d)} \sqrt{\frac{E G_{1c}}{d}} \quad (14)$$

where: d is the specimen width, w is the width of the compression platen, E is the specimen's modulus of elasticity, and G_{1c} is the critical strain energy release rate (fracture toughness). The equation predicts the compressive strength to increase with the specimen elasticity and fracture toughness, and its dependence on geometry, but not on crack length. The apparent difficulty with equation 14 for $w =$ or $> d$, a common geometry for most compression tests, has been resolved by Ashby & Hallam (1986) who considered a multitude of cracks and voids from which winged cracks can initiate and grow. When loaded in compression, the cracks grow and interact with other growing cracks, ultimately leading to coalescence and finally to catastrophic failure. They showed that the initiation condition, for the case of simple compression, was given by:

$$\sigma_f = \frac{\sqrt{3}}{\sqrt{1 + \mu^2} - \mu} \sqrt{\frac{E_b G_{1c}}{\pi a}} \quad (15)$$

where: σ_f is the fracture initiation stress, a is the critical length of a crack in the plane of maximum shear traction, E_b is the modulus of elasticity of the body, and μ is the friction coefficient for sliding crack faces. In equation 15 there is crack-length dependence. Therefore, sudden brittle fracture is predicted once the initiation condition is satisfied.

MATERIALS AND METHODS

Experimental raw materials

Sufficient quantities of two manufactured stoneware clays, denoted as Body A and Body B, were obtained from Clayworks, Dandenong, Victoria, Australia. The composition of the stoneware clays were: (1) Body A - kaolin, feldspar and quartz; and (2) Body B - kaolin, feldspar, quartz and with small additions (a few percent) of goethite, FeO(OH). The precise ratios were not available. At the same time, small quantities of the raw materials in an unmixed state were also purchased for mineral identification. The X-ray diffraction (XRD) identification of three of the raw materials, and quantitative particle-size distribution are reported below.

From observations of thin sections by optical microscopy, and from investigation of conventions followed by manufacturers in Australia, we estimated the volume fractions of the initial constituents to be in the range (1) kaolin: 0.60–0.70, (2) feldspar: 0.20–0.15, and (3) quartz: 0.20–0.15. The essential differences between Bodies A and B lie in the differences between the proportions of kaolin/feldspar/quartz, and in particle-size distributions. These are reflected in finished, fired surface qualities: A is white whereas B is fired darker and shows a coarser surface than A.

Sample preparation and firing

Samples (in wet state) were extruded in 180 mm lengths through a die with a circular aperture of 20 mm diameter and a 1° reducing taper. 180 mm was chosen to reduce or eliminate wasting or necking due to stretching under the sample's own weight prior to cutting off. The extruder barrel was washed at the completion of the extrusion of each stoneware clay body.

All extruded samples were fired in an oxidizing atmosphere to ~1000°C in one firing in a temperature-controlled electric kiln. The firing cycle followed a temperature increase rate of 60°C/h to 300°C, followed by 150°C/h to completion. The kiln was allowed to cool normally to 200°C before opening. After initial firing, all sets of extrusions were sawn to 36 mm sample lengths by a water-cooled, diamond-saw-blade cutter with a movable bed. Altogether, 180 test samples of each body were made, allowing a choice of five for each of the subsequent 10 oxidation firings.

Next, the samples were packed in a systematic ABABAB order to spread any localized variations in temperature/heat work more equably across the whole sample-body range, and fired to higher temperatures. Standard Orton Cones, manufactured by the Edward Orton Jr. Ceramic Foundation, were chosen for use in all kiln firings associated with this project (Orton, 1994). The cones were placed on the centre line of each shelf 100 mm back from the leading edge. Twelve firing temperatures were chosen: Orton Cones 06, 04, 03, 01, 2, 4, 6, 7, 8, 9, 10 and 11.

Sample dimensions and weight

The dimensions of all samples were measured using vernier callipers capable of accuracy to 0.01 mm. The length of the cylinder was measured once; the diameter in three places, and averaged for each sample. The expected relative error in length is estimated as $0.01/36 = 3 \times 10^{-4}$, and in diameter as $0.01/20 = 5 \times 10^{-4}$. From these measurements the volume of each sample was calculated, with the relative error calculated as $2\Delta R/R + \Delta L/L = 1.3 \times 10^{-3}$.

All samples were dried for 24 h at 200°C and weighed immediately on removal from the drying oven using scales (Mettler Model AB204). Wet weight was measured by first boiling samples suspended and immersed in water for 1 h, then allowing the samples to cool naturally for a further 23 h while completely immersed in the water in which they were boiled. Each sample was removed from water, rolled on absorbent paper to dry the surface and weighed.

Particle-size distribution

Samples were prepared using a 0.05% Calgon-in-water deflocculant with sample density of 2.65 g/cc and liquid density 0.9944 g/cc. The sedimentation rate was measured using a SediGraph 5100 instrument for particle-size distribution within the range 0.1–60.0 µm. Particles in the range 60–2000 µm were measured using a column sediment analyser.

SEM imaging of thin sections

Thin sections of each fired sample were cut using a diamond saw to a thickness of ~1.2 mm. The sample face was hand ground using P800 wet and dry papers to minimize irregularities within the cut surface. The sample was dried and attached to a

standard petrology slide using Petropoxy that had been first applied and absorbed into the porous structure before slide attachment. Using standard 15 µm alumina oxide grit, each sample was then reduced to 35 µm average thickness on the laboratory's Logitech LP30 lapping and optical polishing equipment. The sample was then further polished and reduced in thickness using a tin lap with 2.5 µm diamond paste and oil, with the final polished 30 µm finished on Pellon cloth with 1.0 µm diamond paste and oil.

Using the facilities of the ANU's Electron Microscopy Unit, 30 µm thin sections of each sample were carbon-sputter coated. Samples were viewed on the Cambridge 360 instrument, using SEM backscatter mode at $\times 800$ magnifications. Five randomly selected regions from each sample were imaged and recorded both electronically and photographically.

The same carbon sputter-coated thin sections of each sample were subjected to analysis using an X-ray probe on the Unit's JEOL 6400 instrument.

Measurement of mechanical properties

The cylindrical samples were subjected to uniaxial compression on a mechanical testing machine (Instron, Model 4005). Each sample was placed between parallel compression plates. Sellotape, affixed to the ends of the sample, acted as a lubricant between the sample and the platens, also holding the ends of the samples together after fracturing. The conditions of testing were: cross-head speed of 5 mm/min, 100 kN load-cell, normal room temperature and humidity. The elastic modulus in compression was calculated from the slope of the linear portion of load-displacement curve and the dimensions of the sample. The compressive strength was calculated as the ratio of the maximum load sustained by the sample divided by the cross-sectional area.

EXPERIMENTAL RESULTS

Figure 1 shows recordings obtained on the unmixed raw materials, clearly identifying the minerals as pure kaolin, quartz and goethite. X-ray diffraction of bodies A and B (not shown) gave complex diffraction patterns indicating the presence of the three main constituents, i.e. kaolin, quartz and orthoclase feldspar. This conclusion is supported by the work of Chi (1996). Quantitative estimation of

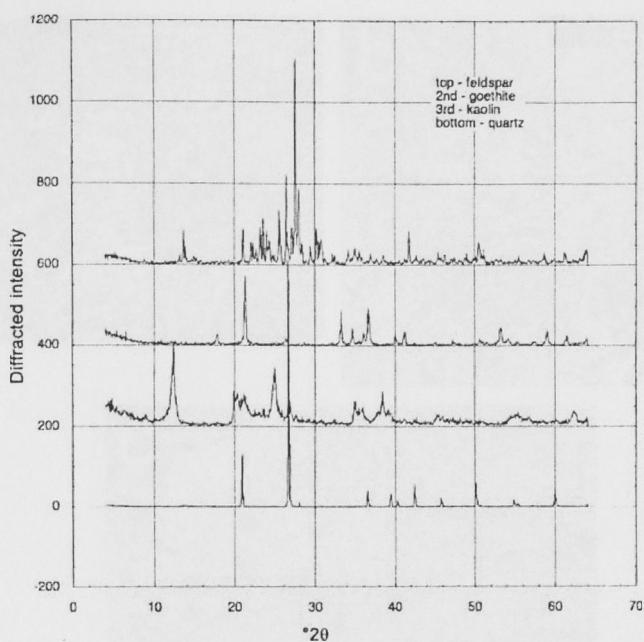


FIG. 1. XRD patterns of three minerals used in the ceramic clay bodies. Goethite appeared in body B only. (Cu-K α radiation, powder samples.)

the components was not attempted due to the uncertainty of the process.

Figure 2 shows the composite distribution of particle sizes measured on the as-received bodies by the two different techniques as described earlier. Significant differences can be observed at the finest particle end, and between ~ 50 and $350 \mu\text{m}$ equivalent spherical diameter range.

Micrographs from cut and polished surfaces of samples from bodies A and B, fired to all indicated temperatures, were obtained by scanning electron microscopy (SEM). Figures 3 and 4 show SEM images for selected samples fired to 1000, 1260 and 1320°C, respectively. The thin sections were coated by carbon sputtering and the images obtained in back-scattered mode.

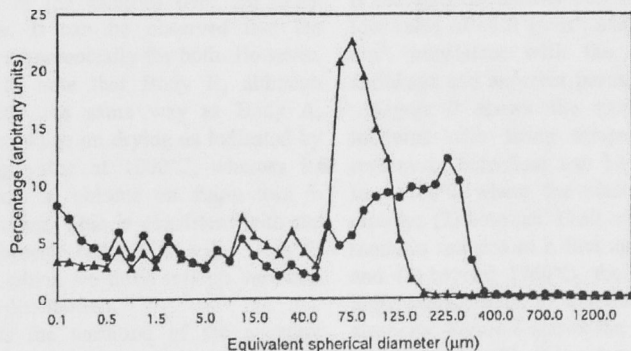


FIG. 2. Distribution of particle sizes in the stoneware clay bodies, derived from measurements carried out using SediGraph 5100 and a Column sediments analyser. Note the differences at the lowest fractions and significant differences for fractions between 50 and 350 μm .

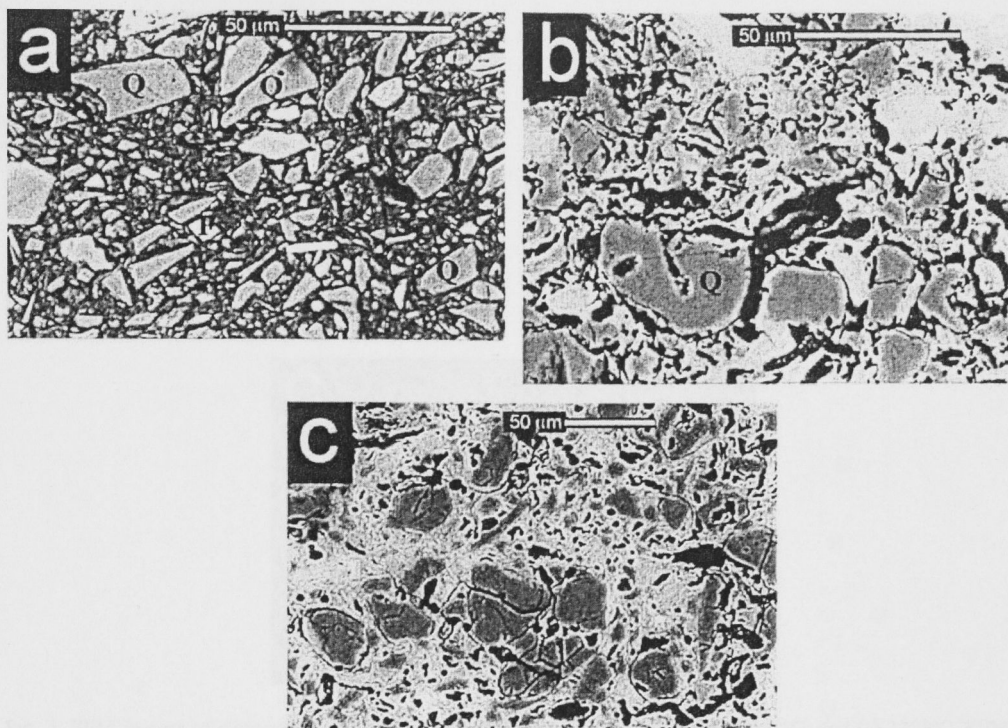


Fig. 3. SEM images of stoneware body A fired to approximately: (a) 1000°C, (b) 1180°C, and (c) 1320°C. SEM backscattered mode from polished thin sections. In (a) a feldspar grain is indicated by F. The large grey particles are quartz grains (some identified by Q). Scale bar = 50 μm .

The results of physical measurements carried out in the course of this study are shown in Figs 5–8. Each point on the graphs represents an average of five individual measurements. Figure 5 shows the changing volume of the samples over the firing temperature range. It can be observed that the volume decreases monotonically for both. However, it is interesting to note that Body B, although prepared in exactly the same way as Body A, showed greater shrinkage on drying as indicated by the lower starting value at 1000°C, whereas its subsequent decrease in volume on firing was in parallel with the other. This is consistent with the initial apparent porosity being higher for Body B than for Body A, which we think reflects variation with particle-size distribution.

Figure 6 shows the variation of the apparent porosity with firing temperature. It varies from close to 19% at the initial firing temperature, down to ~2% at the highest firing temperature. The decrease in apparent porosity is seen to occur over

three stages: (1) a relatively fast change from 1000 to 1180°C; (2) an arrest between ~1180 and 1260°C; (3) a final stage which is again relatively fast. Associated with apparent porosity and volume is the apparent density (not shown), starting at the low value of ~1.8 g/cm³, and increasing to ~2.3 g/cm³, consistent with the changes in volume shrinkage and apparent porosity.

Figure 7 shows the variation of the elastic modulus with firing temperature. Again, three regions of behaviour can be distinguished: (1) up to ~1180°C where the elastic modulus increases rapidly; (2) between 1180 and 1260°C where the modulus remains to a first approximation constant; and (3) beyond 1260°C, the final region, surprisingly characterized by a gradual loss of mechanical elasticity. Figure 8 shows the variation of compressive strength with firing temperature measured in the same test as the elastic modulus. Here three stages of dependence on firing temperature are also evident.

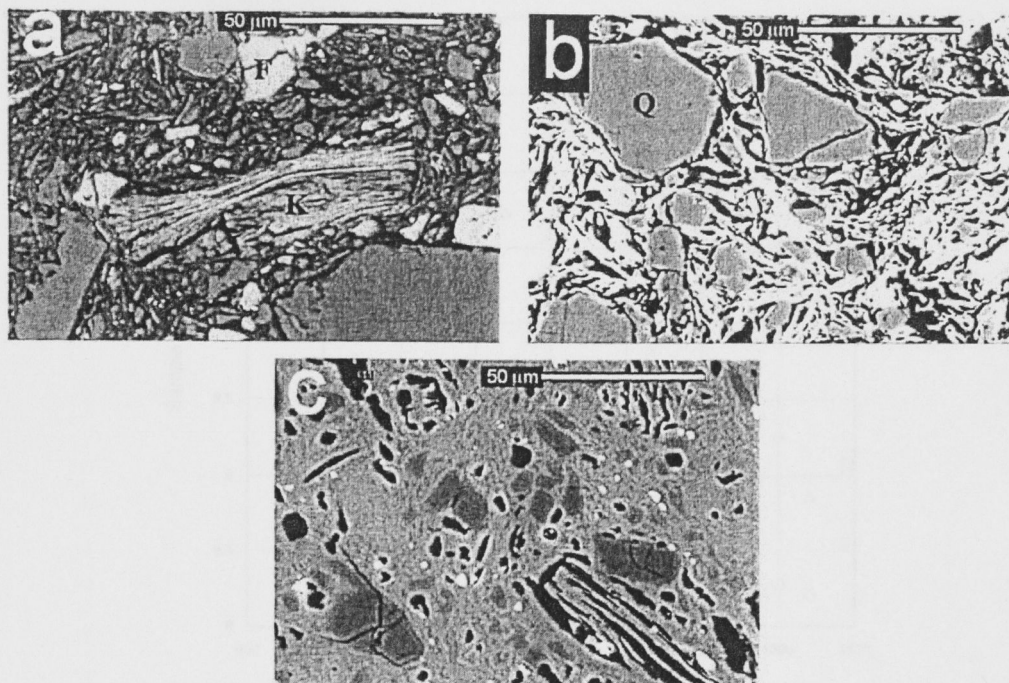


FIG. 4. SEM images of stoneware body B fired to approximately: (a) 1000°C, (b) 1180°C, and (c) 1320°C. SEM backscattered mode from polished thin sections. The large grey particles are quartz (Q). Part (a) shows a large particle (K) with dickite-like morphology, and feldspar particles (F) as identified by XRD. White particles in (c) (infrequently observed) give indications, under SEM probe, of tin or zircon, and must be original inclusions in the raw materials. Scale bars = 50 µm.

DISCUSSION

Microstructure

The changes in microstructure, seen in Fig. 3a–c for Body A, and Fig. 4a–c for Body B, represent characteristic points of three significant stages in the development of microstructures in the stoneware clay bodies:

- (1) up to ~1180°C,
- (2) from ~1180 to 1260°C, and
- (3) above ~1260 to 1320°C.

These changes are the result of phase transformations, as well as melting and eutectic formations that take place increasingly in stage 2, and continuously in stage 3. Initial reactions (dehydration of minerals and driving out of volatiles) are completed by ~600°C (Sosman, 1965; Deer *et al.*, 1992). In this temperature range, kaolin transforms to metakaolin with slight shrinkage and an increase in porosity (Kingery *et al.*, 1976). By ~980°C, metakaolin decomposes into spinel and reactive

SiO₂ (Brindley & Lemaître, 1987). The original particles appear to be held together at numerous but small contact points (assumed to result from sintering) so that the compressive strength reaches ~40 MPa as shown in Fig. 8. The original distribution and morphology of the particles are still preserved (these microstructures are very similar to those reported in Fig. 2 of Bauluz *et al.* (2004), who report that there is little glass formation at this temperature, although the differences in mineral composition must be noted). The micrographs in Figs 3a and 4a show close similarities in microstructures: voids are almost all uniformly small; larger voids are associated with margins of much larger particles; individual particle boundaries are obvious and clearly defined; and there is no observable aggregation of particles as a consequence of melting. Noticeable in Body B are large laminar kaolin particles (Fig. 4a). The most obvious feature that distinguishes Body A from Body B is the difference in size and distribution of

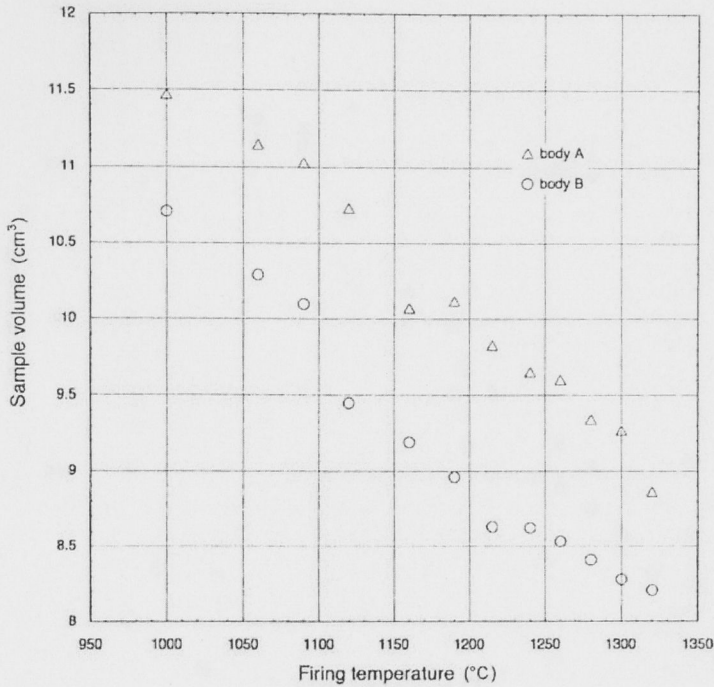


FIG. 5. Variation of measured sample volume over the whole firing range. Note that stoneware body B, although prepared in exactly the same way as the other, shows greater shrinkage on drying, whereas its subsequent decrease in volume on firing was in parallel with stoneware body A. Each point is an average of five samples.

particles within the range of 50 to 350 μm (Fig. 2). The different types of voids observed include articulated voids that are a direct consequence of the irregular contact points between particles of differing shapes and sizes, and both sealed and articulated voids that are inherent in the raw materials introduced into the clay bodies.

As can be seen in Figs 3b and 4b, further changes take place at increasing temperatures. At $\sim 1100^\circ\text{C}$, feldspar melts, leading to the formation of glasses in combination with SiO_2 evolving from metakaolin, reacting with quartz grains to melt outer surfaces and sharp corners, forming an inhomogeneous glassy matrix (Smith & Brown, 1988). Above 1150°C , orthoclase feldspar transforms to leucite and SiO_2 , adding further to the glassy matrix of varying composition. According to Deer *et al.* (1992), and Wyatt and Dew-Hughes (1974), quartz transforms to cristobalite at 1470°C . However, Heany *et al.* (1995) reported that cristobalite can be metastable well below this temperature. Simultaneously, porosity is correspondingly reduced. This is already visible in

micrographs shown in Figs 3b and 4b, where large particles and voids are rounded off, small particles have fused together, and micropores have to a large degree disappeared. Thin cracks appear around large particles as a consequence of the above-mentioned transformations with accompanying volumetric changes. Small particles ranging between 1 and 5 μm that were clearly observable in each of the stoneware clay bodies in Figs 3a and 4a are no longer present. Particles of $>10 \mu\text{m}$ are surrounded by fused aggregations containing larger and less evenly distributed voids. Voids larger than those contained in, and associated with, the surrounding solid continue to be associated with large particle boundaries. There is evidence of cracking in large-particle boundary/small-void interfaces as well as transverse cracking in elongated large particles.

At the highest firing temperature ($\sim 1320^\circ\text{C}$), a complex glassy matrix, variegated in appearance, seen in Figs 3c and 4c, is the dominant phase of the microstructure, occupying a greater proportion in Body B than in Body A. It is assumed to be glassy

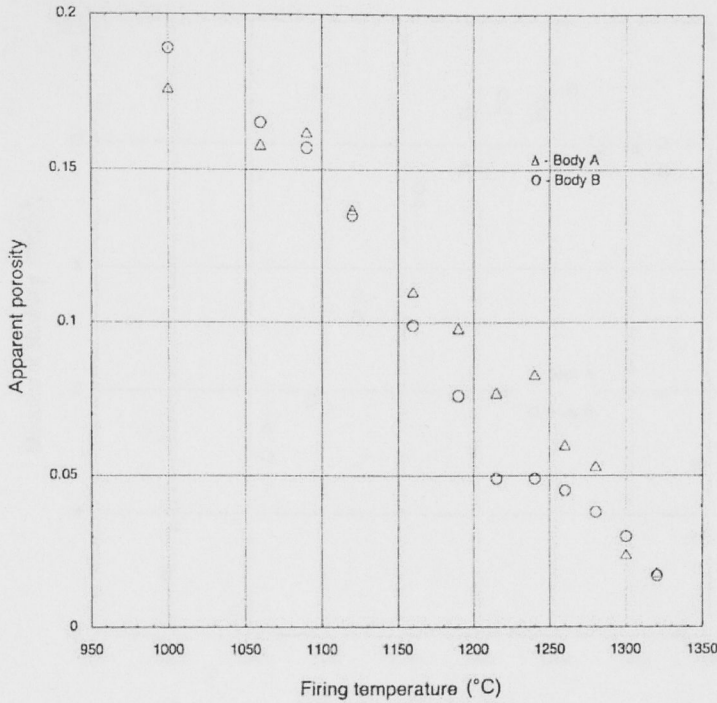


Fig. 6. Variation of measured apparent porosity over the whole firing range. Stoneware body B shows greater decrease of open porosity on firing between 1180° and 1260°C than stoneware body A. Each point is an average of five samples.

since XRD gives a broad scattering peak with small sharper peaks that must arise from the remaining crystalline phases. The larger extent of vitrification in Body B is likely to be the result of the small additions of the Fe oxide. The other major phase comprises silica (quartz particles), clearly identifiable under SEM analytical probe, and some grains also identified in the micrographs. The interface between the remaining silica particles and the matrix is diffuse and in many places cracked. Porosity has decreased considerably, and it is not evident which part consists of open voids, and which of sealed voids, now approximately in equal proportions. Cracks are evident around the grains as well as within the grains, as reported by Menéndez *et al.* (1996). We assume the cracks have formed on cooling from the firing temperature due to differential shrinkage. Changes in the size and distribution of voids are less obvious than in the earlier micrographs. Body B contains elongated voids (~50 μm long), which originated from the kaolin particles as can be seen in Fig. 4a.

Porosity and density

We have estimated the sealed porosity by making use of equation 9. Figure 9 shows the variation of open porosity, as derived from apparent porosity, and the calculated sealed porosity. For each body, the sum of open and sealed porosities gives the total porosity. The finer details, evident in the two bodies, are ascribed to differences in particle-size distribution and the associated rate of formation of eutectics and sintering. The sudden increase in sealed porosity at ~1180°C suggests onset of melting and fusion leading to closure of previously articulated voids. The calculations required the knowledge of solid density as defined by equation 3, which can be estimated using equation 10. We have been able to determine that the silica-rich phase is quite pure and can be identified as quartz (Fig. 1). From Sosman (1965) and Heaney *et al.* (1995) we take the density of the initial quartz constituent as 2.65 (± 0.01) g/cm^3 . On firing to high temperature (1300°C), quartz can convert to

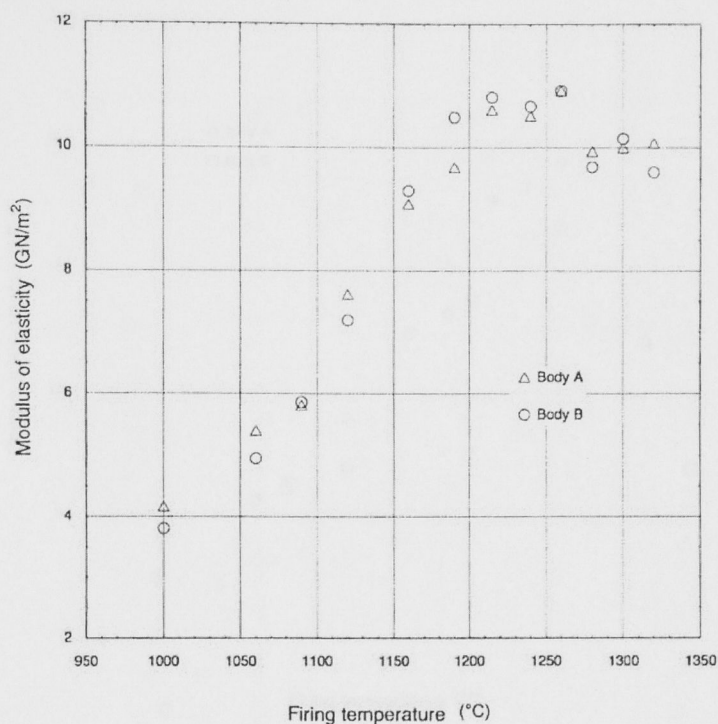


FIG. 7. Variation of measured elastic modulus in compression over the whole firing range. Note the decrease observed after 1260°C, due to the formation of inhomogeneous glasses and circumferential cracks around silica particles. Each point is an average of five samples.

cristobalite with a corresponding reduction in density (Smith & Brown, 1988) which can be as low as 2.35 g/cm^3 . The feldspars used in these compounds are K-rich, orthoclase minerals. This has been confirmed by XRD, and during SEM observations. We take the density of the initial constituent as $2.58 (\pm 0.02) \text{ g/cm}^3$ (Deer *et al.*, 1992; Smith & Brown, 1988). In the temperature range of 1120 to 1180°C, feldspars melt forming a glassy phase of variable density, which we estimate as $2.38 (\pm 0.02) \text{ g/cm}^3$. The structure and properties of Australian kaolin minerals have been studied thoroughly by Chi (1996). The density of the kaolin from Victorian fields is taken as $2.64 (\pm 0.02) \text{ g/cm}^3$. On firing, kaolin transforms gradually to metakaolin to spinel, forming mullite as well as contributing to glass formation of density $\sim 2.38 \text{ g/cm}^3$.

We have calculated the solid density of both stoneware clay bodies after the first firing as $2.629 (\pm 0.025) \text{ g/cm}^3$. It is assumed to be constant

between 1000 and 1180°C. The next step required estimation of the variation of densities with higher firing temperatures. We noted from SEM observation of thin sections, and from XRD results, that at the highest-temperature (1320°C) feldspars have fused with kaolin, and that approximately a third of the quartz has also fused with surrounding constituents. At the same time XRD traces indicated an increase in the X-ray amorphous (glass) content from insignificant at 1000°C, to $\sim 40\%$ at the final firing at 1320°C. We assume the volume fraction of glass to be 0.4, and its density to be 2.38 g/cm^3 . The volume fraction of the transformed and recrystallized materials is 0.6; therefore, the final solid density of the bodies is estimated to be $2.51 (\pm 0.03) \text{ g/cm}^3$. It is assumed that it decreases monotonically between 1180 and 1320°C.

Volume shrinkage is evidence for reduction in porosity, and this information was used by Zhang *et al.* (1944) to corroborate their measurements of permeability during hot isostatic pressing of mineral

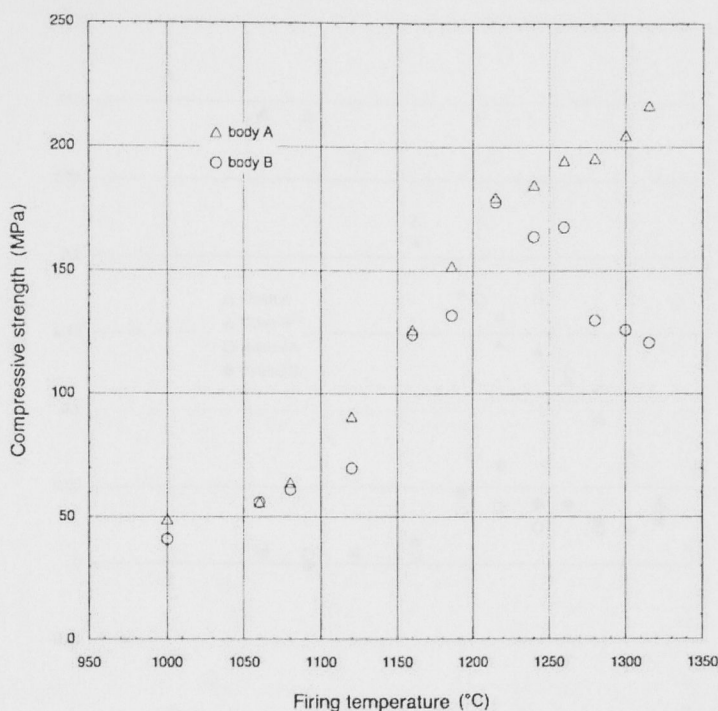


FIG. 8. Variation of compressive strength of the two stoneware clay bodies A and B over the whole firing range. Body B is weaker as the firing temperature increases. Each point is an average of five samples.

aggregates. We have already used this information in equation 9 to derive sealed porosity. Other methods for porosity measurement could have been applied but were deemed to be unnecessary as the results reported here are consistent with densification behaviour reported for other aggregate bodies. For instance, in the above-mentioned work (Zhang *et al.*, 1944), the porosity of the aggregate starts at ~ 0.22 and ends at 0.06 after isostatic hot pressing. The total porosity measured for Bodies A and B is also around that value after firing to 1300°C (slightly higher because densification occurred as a result of sintering forces alone without the aid of isostatic pressing). By contrast, the greater initial porosity value of ~ 0.32 for bodies A and B, is ascribed to the presence of introduced inherent porosity, as evident in the micrographs in Figs 3a and 4a.

MECHANICAL PROPERTIES

The effective value of the modulus of the composite was estimated using equation 11. For this we need

the moduli of individual components: for quartzite, $E = 55 (\pm 20)$ GPa (Brindley & Lemaitre, 1987; Jumikis, 1979), for feldspar, $E = 45 (\pm 20)$ GPa. Kaolin shows both strong anisotropy and some internal porosity; we take the value of $15 (\pm 10)$ GPa as a reasonable average value. Allowing for the uncertainty in the volume fraction of the components, the effective modulus of the stoneware clay bodies is calculated to be $30 (\pm 15)$ GPa. No allowance for porosity has been made. Therefore this value corresponds to an isotropic composite at zero porosity. At 1000°C , porosity is of the order of 35%, and the much lower value of ~ 4 GPa was found by experimental measurements (Fig. 7). As the absolute porosity and its variation have been calculated, one can analyse the experimental data from Fig. 7 using equations 12 and 13. A plot of the experimental values against porosity factors is shown in Fig. 10, where it can be seen that extrapolation towards zero porosity of the trend shown by the first 4–5 points is close to 35 GPa, well within the above-calculated range of the effective modulus at zero porosity. The result for

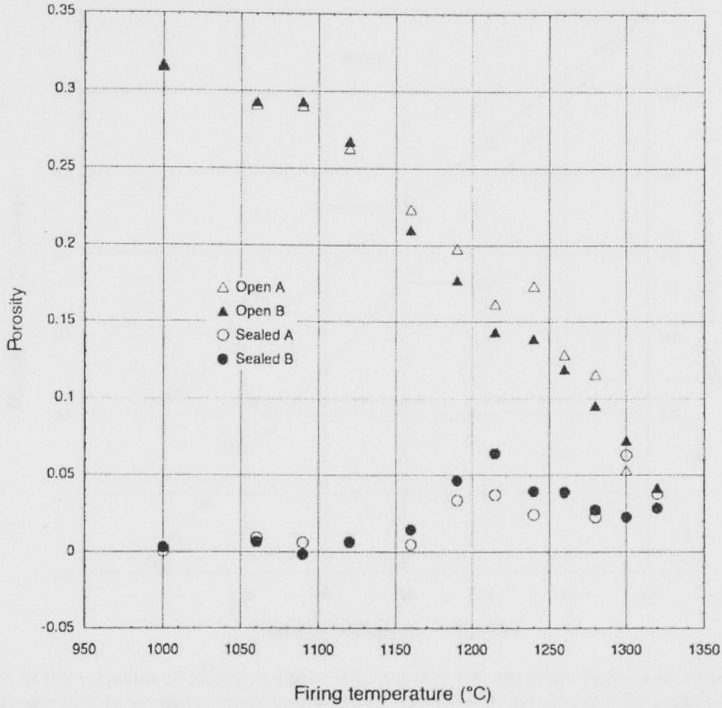


Fig. 9. Calculated open and sealed porosity over the whole firing range. Open porosity (open triangles – Body A, open circles – Body B) calculated from equation 4, and sealed porosity (filled triangles – Body A, filled circles – Body B) calculated from equation 9.

Body B is very similar. This analysis predicts the modulus of both fired stoneware clay bodies at zero porosity to be in the range 25–35 GPa.

For samples fired beyond 1180°C the elastic modulus appears not to be affected by variations in porosity, even though total porosity continues to decrease. The modulus reaches peak values of close to 12 GPa between 1180 and 1260°C, and then, for firings at the highest temperatures employed, decreases slightly to ~10 GPa instead of rising to near 35 GPa as predicted in Fig. 10. We ascribe this remarkable phenomenon to two factors: (1) the chemical changes occurring in the composite bodies; and (2) the formation of circumferential cracks around the remaining silica particles. The first factor is the formation of eutectics and glassy phases resulting in a lower modulus than that of original feldspars, and the second is the decoupling of silica particles from the matrix by the cracks. We propose that both contribute simultaneously to lower the elastic response of the materials.

Assuming a value of 0.5 for the friction coefficient, and solving equation 15 for critical crack length, gives:

$$a_c \cong 2.5 \frac{G_{1c} \times E}{(\sigma_f)^2} \tag{16}$$

Figure 11 shows the variation of the critical crack size as a function of firing temperature for the two stoneware clay bodies, assuming a typical value of $G_{1c} = 20 \text{ J/m}^2$ for ceramics, and using the modulus and strength values from Figs 7 and 8. The graph shows some similarity to the graph for open porosity with firing temperature (Fig. 9), suggesting that the pores play the role of the critical crack. The size of the pores decreases with decreasing porosity (increasing firing temperature) as is evident from the micrographs. The compressive fracture strength of the samples increases correspondingly as the critical crack size reduces from ~100 μm at the initial firing temperature to 20 μm at 1200°C. Above 1260°C, the formation of micro-eutectics at

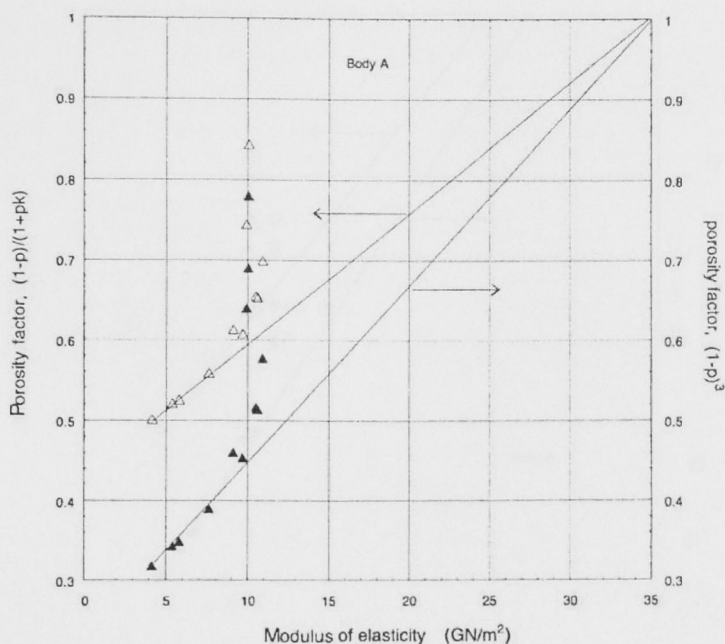


FIG. 10. Analysis of the variation of elastic modulus with porosity for stoneware body A in terms of equations 12 and 13. Extrapolation to zero porosity points to a value of ~ 35 GPa, in agreement with calculations described in the text.

contact points leads to localized melting and glass formation on cooling. Differential thermal shrinkage causes cracks to appear around the large particles. This has a significant effect on Body B since it contains larger particles, the shrinkage cracks contribute to lowering of its fracture strength at the high firing temperatures. Interestingly, Body A continues to increase in strength even at the higher firing temperatures. Tentatively, we ascribe this different behaviour to the differences in particle-size distributions, which is the subject of a separate study.

CONCLUSIONS

The absolute porosity of the stoneware clay samples drops continuously from ~ 0.33 at first firing at 1000°C to ~ 0.08 after the final firing at 1300°C . Initially, the porosity appears as connected open voids only, changing to both sealed and open porosity, each comprising a ~ 0.04 fraction at the final firing. This continuous densification of the material is not mirrored by a corresponding increase in elastic modulus. The modulus of elasticity of the

samples, whilst primarily determined by the solid constituents, is also influenced by the presence of pore/voids and microcracks. The modulus-porosity relationship is not described adequately by the existing physical models.

The micromechanics of compressive failure in stoneware clay bodies appears to be related to porosity in that the critical crack size for failure initiation decreases with decreasing void size. However, above $\sim 1260^\circ\text{C}$ the simple relationship does not appear to hold for Body B, where the compressive strength reverses its trend, contrary to that of porosity. Since Body B contains a larger amount of particles in the $100\text{--}300$ μm size, it leads us to the tentative conclusion that shrinkage cracks forming around these particles lower the fracture strength of these fired stoneware clays.

ACKNOWLEDGMENTS

The authors gratefully acknowledge assistance given by Dr Sally Stowe and the staff of the ANU Electron Microscope Unit for their invaluable instruction in the

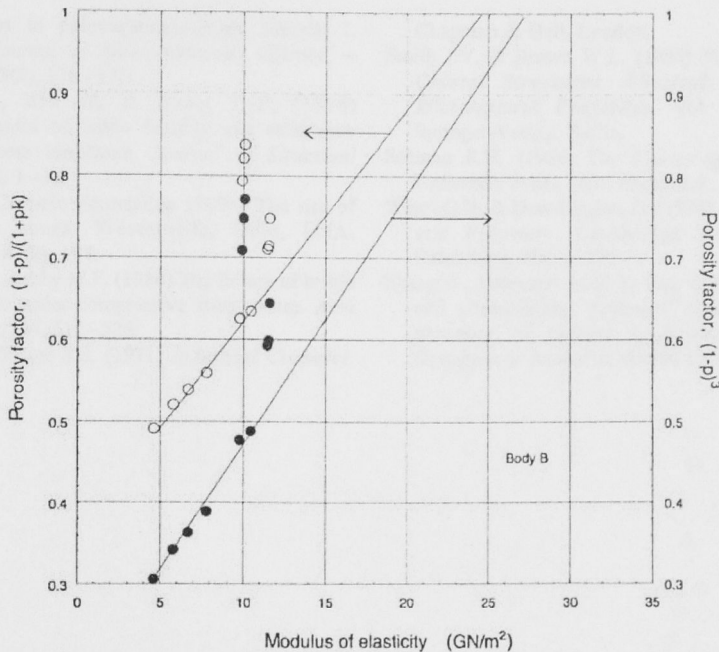


FIG. 11. Predicted variation of critical crack size (using equation 16) for compression fracture of the stoneware clay bodies, assuming a constant strain energy release rate of 20 J/m^2 , and using the experimental values of modulus and compressive strength from Figs 7 and 8.

use of their instruments and assistance in imaging. We also wish to thank Dr Meta Sterns of the Department of Chemistry for X-ray diffraction of the samples, and the Geology Department, ANU, for the preparation of thin sections for microscopy, and helpful discussions regarding the interpretation of some microstructural features. All firings in this program were carried out in kilns in the Ceramics Workshop, Faculty of the Arts, ANU. We are also grateful to the AGSO for the use of their particle-size analysis equipment.

REFERENCES

- Ashby M.F. & Hallam S.D. (1986) The failure of brittle solids containing small cracks under compressive stress states. *Acta Metallurgica*, **34**, 497–510.
- Bauluz B., Mayayo M.J., Yuste A., Fernandez-Nieto C. & Gonzalez Lopez J.M. (2004) TEM study of mineral transformations in fired carbonated clays: relevance to brick making. *Clay Minerals*, **39**, 333–344.
- Brandt R.C. Hasselman D.P.H. & Lange F.F. (eds) (1978) *Fracture Mechanics of Ceramics*, Vol. 4, Plenum Press, New York.
- Brindley G.W. & Lemaitre J. (1987) Thermal, oxidation and reduction reactions of clay minerals. Pp. 319–370 in: *Chemistry of Clays and Clay Minerals* (A.C.D. Newman, editor). Monograph No. 6, Mineralogical Society, London.
- Chi M.A. (1996) *The ultra-structure of kaolin*. PhD thesis, Australian National University, Menzies Library, Canberra.
- Deer W.A., Howie R.A. & Zussman J. (1992) *An Introduction to the Rock-Forming Minerals*. Longman Scientific & Technical, London.
- Heaney P.J., Prewitt C.T. & Gibbs G.V., editors (1995) *Silica: Physical Behaviour, Geochemistry and Materials Applications*. Reviews in Mineralogy, **29**, Mineralogical Society of America, Washington, D.C.
- Helmuth R.A. & Turk D.H. (1966) *Highway Research Board*. National Research Council (US) Special Report **90**, 135–141.
- Holliday L. (1967) *Composite Materials*. Elsevier, London, p. 16.
- Jumikis A.R. (1983) *Rock Mechanics*. Trans Tech Publications, New Jersey. p. 94.
- Kendal K. (1978) Complexities of compression failure. *Proceedings of the Royal Society of London*, **A362**, 245–263.
- Kingery W.D., Bowden H.K. & Uhlmann D.R. (1976) *Introduction to Ceramics*, 2nd edition. John Wiley & Sons, New York.
- Kunori T. & Geil P.H. (1980) Morphology-property

- relationships in polycarbonate-based blends: I. Modulus. *Journal of Macromolecular Science - Physics*, **B18(1)**, 118–175.
- Menendez B., Zhu W. & Wong T.-F. (1996) Micromechanics of brittle faulting and cataclastic flow in Berea sandstone. *Journal of Structural Geology*, **18**, 1–16.
- Orton E., Jr., Ceramic Foundation (1994) The use of pyrometric cones. Westerville, Ohio, USA. *Intereram*, **43(2)**, 107.
- Sammis C.G. & Ashby M.F. (1986) The failure of brittle porous solids under compressive stress states. *Acta Metallurgica*, **34**, 511–526.
- Singer F.S. & Singer S.S. (1971) *Industrial Ceramics*. Chapman & Hall, London.
- Smith J.V. & Brown W.L. (1988) *Feldspar Minerals: Crystal Structures, Physical, Chemical and Microtextural Properties*. Vol. 1, Chapter 12, Springer-Verlag, Berlin.
- Sosman R.B. (1965) *The Phases of Silica*. Rutgers University Press, New Brunswick, Canada, p. 11.
- Wyatt O.H. & Dew-Hughes D. (1974) *Metals, Ceramics and Polymers*. Cambridge University Press, Cambridge, UK, p. 227.
- Zhang S., Patterson M.S. & Cox S.F. (1994) Porosity and permeability evolution during hot isostatic pressing of calcite aggregates. *Journal of Geophysical Research*, **99/B8**, 15,741–15,760.